Experimental and Computational Analysis of Cell Mechanics during Spreading and Migration

Sangyoon Han

A dissertation

submitted in partial fulfillment of the

requirements for the degree of

Doctor of Philosophy

University of Washington

2012

Reading Committee:

Nathan J. Sniadecki, Chair

Santosh Devasia

Garrett Odell

Program Authorized to Offer Degree:

Mechanical Engineering

University of Washington

Abstract

Experimental and Computational Analysis of Cell Mechanics during Spreading and Migration

Sangyoon Han

Chair of the Supervisory Committee:
Assistant Professor Nathan J. Sniadecki
Mechanical Engineering

The processes of cell migration and spreading are critical for wound healing and cancer metastasis. Cells use their ability to generate mechanical forces to probe the mechanical resistance of their environment and move forward. Biomechanical explanations for how mechanical factors in their environment affect these forces and how cells use their forces to migrate are still unclear. Here, using patterned micropost arrays, the effects of substrate stiffness, cell adhesive area, and micropost density on contractile forces of endothelial cells were investigated. Each of these traits was found to play a fundamentally different role in contributing to overall cellular contractility. Substrate stiffness influenced the magnitude of traction force in a cell independently of its spread area whereas spread area affected it by regulating the number of available adhesions. By quantifying the size of individual focal adhesions on each post, it was also found that focal adhesion area responds to each parameter in the same way that traction forces do. A computational model (1) was then adopted to predict, using ordinary differential equations, the traction forces produced during cell migration. To validate the results from these simulations, NIH 3T3 fibroblasts were seeded

onto arrays of posts, but allowed to migrate only in one dimension by patterning the tips of the posts with lines of extracellular matrix (ECM) proteins. Experimentally measured development of force at their leading edge and loss in force at their trailing edge matched closely with the computational simulations. Moreover, I found experimentally that the increase in force at the leading edge caused a decrease in force at the adjacent post, but did not affect the rest of the forces at the interior or trailing edge of the cell. Similarly, my experiments showed that when a cell detached from a post at its trailing edge, the decrease in force at the tail caused an increase in force at the adjacent post, but not at the interior or front of the cell. To match these experimental results, the model requires the elasticity of the cell to be lower than the elasticity of its substrate and the tension in the cell to be uniform across the whole cell. The significance of this dissertation work is that it provides biophysical relationship and mathematical model involving mechanical properties of a substrate, a cell and traction force generation during spreading and migration.

Acknowledgements

It has been a long journey to come to face the end of my formal education, and I do not have any idea about how I can begin thanking who have brought me here. I will start with the two people who have known me longest. Thank you to my father and mother in Korea, Kapsoo Han and Wonkyung Yang. In addition to giving me engineering-oriented practice and good education environment, you have always supported me with encouraging advice and prayers.

To the most important person in my life, Sunyoung Ahn. You have been always with me anywhere (at the lab, office, library and café), anytime (even at late night) over past four years, being excited by good results and also sometimes going through a dark tunnel with me. Without your sacrificial help and support (and some nutritious snacks), I would not have been able to take even one step forward. Thus, you deserve this doctoral degree.

I also want to thank my son, Caleb for growing up to a one-year-old boy with such many smiles and good health even though there were some occasions when I could not respond to your invitations to play with you. I am also grateful to my sister-in-law and brother-in-law, Uijeong Ahn and Bumhee Ahn for being part of my family in the same house and giving me extra time by sharing their time for taking care of Caleb. I also appreciate loving effort of my friend, Jieun Ahn for Caleb.

I am also thankful to my advisor, Nate Sniadecki. I remember the big decision you made to allow my research career to be toward on the field of cell mechanics as your first student. Since then, you have shown me a wide variety of virtue that a good scientist should have such as balancing work and life, asking good questions, and trusting your student. These things have contributed greatly to my success. To my dissertation committee: Dr. Garry Odell, Dr. Tom Daniel, Dr. Santosh Devasia, Dr. Duane Storti and Dr. Alex Veress. Our conversations have opened my eyes to new perspectives and made my work more solid and confident. I

especially would like to appreciate Dr. Odell's time and effort on coaching me on how to improve my scientific writing. The following sentence will be one of my writing standards for the rest of my academic life: "Good scientific writing asserts claims that readers can interpret in only one way".

To the members of Sniadecki Lab, it has been my pleasure to watch how dynamic the lab can become as one of you joined the lab each year and how you can be a source of encouragement in times of frustration. Thank you Lucas, Shirin, Marita, Kevin and alumni Anthony for your hardworking collaboration, advice, proofreading, and all the conversations which have enriched my graduate student experience. I would also like to thank Sean, Max and Ariel for their help as an undergraduate student, Dr. Ulich Hetmaniuk, Dr. Brian Fabien and Dr. Peizhe Shi for their discussion on my mathematical model, Dr. Peter Chen for the advice on the cell migration study, and Dr. Albert Kobayashi for the scholarship which supported my research.

It has been such a blessing to have opportunities to build friendships at UW. Danny, Shanna, Cher, Heather, Christy, Dan, Fei, Jiradech, Vara, Sheri, Jong, Jaehyuk, Hong, Kiseok, Heechang, Heeseok, Sooyeon, Inkwon, Jonghoon, Hyunboo and Hwan, all the conversations I have had with you have been very precious to me. I especially thank my dear friend, the late Hyunchul Kim for giving me many rides and encouraging me to succeed in UW in my early years here.

Finally, this moment reminds me of the question that triggered me to come here at UW: why did I refuse to stop studying after my master's degree and decide to study more in US? It was neither because I was so smart that I had to use my brain for the further study, nor because I liked studying than doing any other things. I believe that it was my God who brought me here and gave me a motivation to study: to serve people with the knowledge I learned. Pastor Byungkook Yoo, Pastor Eugene Cho, Minhee, Pam, Tim, Louise, Jin, Young, and families at Quest church and Onnuri church in Seoul, thank you for your prayer and fellowship.

TABLE OF CONTENTS

LIST OF FIGURES

LIST OF TABLES

1. General Introduction

1.1 Contractile Forces and the Mechanical Environment of a Cell

Crawling cells can sense and respond to a variety of external signals, both chemical and mechanical. In particular, cells exert contractile forces to probe the mechanical properties in their environment and, as a result of transducing mechanical feedback into a biochemical signal, they change their structure, behavior, lineage and fate. How cells sense mechanical factors has been elusive. Owing to the recent advance in nanotechnology-based cellular assays, it is now possible to learn how components of a cell such as focal adhesions and stress fibers work in the overall system to exert cell forces in response to specific mechanical properties in the environment. The knowledge gained from the new tools will contribute to better biomaterial design and tissue engineering.

1.1.1 Contractile Forces in Non-Muscle Cells

Contractile forces of a cell are generated by interactions between actin and myosin filaments. Actin filaments are one of the three filaments (microtubules, actin, and intermediate filaments) in a cell and are formed by polymerization of globular actin monomers. When multiple actin filaments are bound with myosin II and actin-crosslinking proteins (e.g. α-actinin), they form a fiber called the stress fiber which is typically over 13 micrometers long and about 0.25-2.5 micrometers wide (2). Myosin II is a double-headed protein that has three pairs of peptide chains: two heavy chains that form a long rod domain, two regulatory light chains that regulate myosin activity, and two essential light chains that stabilize the heavy chain structure (3) (Figure 1). In the absence of regulatory light chain phosphorylation, a myosin II molecule forms a compact, rounded shape where its head binds its tail. But when the regulatory light chains are phosphorylated, head-tail interactions stop and the numerous myosin II molecules aggregate into filaments that are bi-polar in the sense that many actin-binding heads of myosin II molecules face in opposite directions. Once phosphorylated, myosin II can perform a power stroke on actin filament by ATP hydrolysis which puts tension in the fiber (4).

Myosin light chain is phosphorylated by several kinases including myosin light chain kinase (MLCK) and Rho kinase (ROCK). Many signals from a cell's receptors can activate these kinases. For example, calcium-calmodulin activates MLCK. But the small GTP-binding protein RhoA plays a major role in myosin activity by activating ROCK. While both MLCK and ROCK can phosphorylate myosin light chain directly, ROCK (not MLCK) also inhibits the myosin phosphatase which dephosphorylates myosin II, resulting in increased myosin phosphorylation (5) (Figure 1). Cells regulate the myosin-driven forces via these signaling molecules which result from sensing the cell's environment.

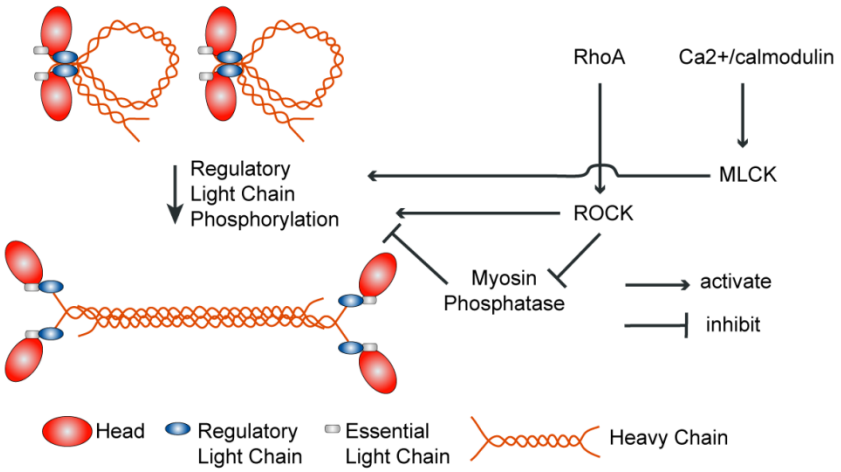

Figure 1. Molecular structure of myosin II and signaling pathways that leads to phosphorylation of myosin phosphorylation

1.1.2 Extracellular Matrix

The environment that surrounds a motile cell *in vivo* is extracellular matrix (ECM). It is composed of matrix proteins such as fibronectin, collagen, laminin, vitronectin and elastin which the motile cell or other accessory cells secrete. Fibronectin, which we use experimentally in this thesis, is a major component of ECM that displays many - sites for a cell's trans-membrane integrins to bind plus binding sites for other ECM proteins such as collagen, heparin, and fibrin (6). Collagen and elastin serve as tension-bearing structures. These proteins form strong fibers that are mixed with a gel-like substance that consists of proteoglycans. By their affinity with water, proteoglycans provide resistance against compressive forces as well as regulate cell behavior through interactions with other

enzymes. ECM can also form a sheet-like mesh, referred to as the basement membrane, which consists of laminin and collagen networks. Mechanical and structural features of the ECM such as stiffness, content, and density of available ligands can influence cellular functions through mechanosensation by integrins (7). In experiments in this dissertation, we attach fibronectin to an artificial elastomer substrate which provides, *in vitro*, the mechanical properties that collagen, elastin, laminin, and proteoglycans provide *in vivo*.

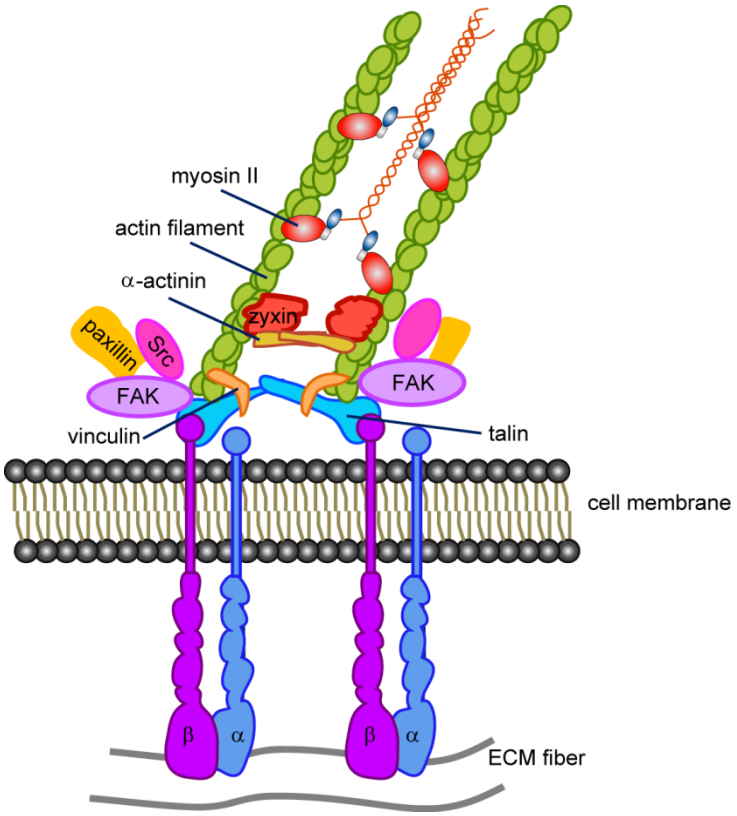

Figure 2. Focal adhesion structure.β subunits of integrins bind to both focal adhesion proteins on the cytoplasmic side and the ECM ligands on the extracellular side of the cell membrane. Talin, vinculin, and α-actinin serve as mechanical anchorage whereas FAK, Src, paxillin and zyxin are signaling proteins in a focal adhesion.

1.1.3 Integrins and Focal Adhesions

Integrins are heterodimeric, transmembrane receptors that bind to ligands found in the ECM (8) (Figure 2). In particular, integrins $\alpha_v\beta_3$ and $\alpha_5\beta_1$ bind to a short peptide sequence (Arg-Gly-Asp, RGD) found in fibronectin. They have a width of 10 nm and are ten to one hundred times more abundant on a cell's surface than other non-adhesive receptor types expressed in many cell types including smooth muscle, endothelium, platelets, and

osteoclasts (9). Integrins are freely dispersed within a cell's membrane, but they cluster when binding to ligands. A conformational change occurs upon binding of integrins to ligands within the cytoplasmic domains of integrins that allows for the recruitment of proteins at the cytoplasmic side of the membrane. These proteins are known as focal adhesion proteins. They include vinculin, talin, and α-actinin which link integrins to the actin cytoskeleton. At the same time, signaling proteins (FAK, Src, paxilin, and zyxin) - aggregate in focal adhesions and serve as signaling transducers that interpret the cell's environment and influence cellular decisions about migration, apoptosis, proliferation, or differentiation. In particular, these signaling kinases trigger the activation of Rho GTPases such as Rac which induces actin polymerization (7). As more focal adhesion proteins and integrins are recruited, the size, strength and signaling activity of the structure becomes larger. These aggregated clusters are known as focal complexes and are approximately a hundred nanometers in diameter and contain over a hundred different proteins that associate within the adhesion site (10-12). Focal complexes are transient structures that can vanish or develop into mature focal adhesions. Although the molecular nature of ligand binding is relatively well-established, the changes that allow the focal complex to transition into a focal adhesion remain elusive. Yet, the size, strength, assembly, and disassembly of focal adhesions appear to be key mediators of many cellular functions.

1.1.3.1 Role of Mechanical Forces in Focal Adhesion Maturation

One aspect of focal adhesion maturation is that mechanical forces acting on the structure are essential for its regulation (13). The formation and growth of focal adhesions relies on myosin II, especially its isoform myosin IIA (3,14,15). It is increasingly evident that traction forces from the actin-myosin contractile machinery mediate the assembly and disassembly of focal adhesions (16,17). Furthermore, focal adhesions act as points where tension in stress fibers are transmitted to the surrounding microenvironment, so they are essential not only for a cell's ability to migrate, but also to pull and rearrange proteins in the ECM or reshape tissue during morphogenesis (18-21).

1.2 Force Measuring Tools

Cytoskeletal tension in the stress fiber is transmitted, via focal adhesion, to the underlying environment and, if the environment is deformable, the transmitted force deforms the substrate. Traction forces have been hypothesized to drive cell migration, but they have been difficult to measure when they are studied using rigid glass substrates. Deformable substrates have provided approaches to observe and quantify cellular traction forces by the extent of physical distortion in a substrate.

1.2.1 Silicone Wrinkling Membrane

The first method for measuring traction forces was to use a thin film of silicone rubber that wrinkled under the load from traction forces exerted on them (22). This wrinkling substrate was made by briefly exposing silicone fluid to a flame that crosslinked only the surface of the silicone, creating a skin of 1 μm thickness. When cells were plated on the surface, they spread out and pulled tangentially on the rubber sheet, producing visible wrinkles in the rubber (Figure 3). This result was significant in that traction forces could be observed and compared for the first time. Wrinkling membranes were used to confirm that signaling pathways such as the small GTPase RhoA or Ca2+/calmodulin pathways regulate traction forces through stress fiber formation and focal adhesion formation (23,24). Despite the immense significance of this technique to the field, it provided a limited measurement because it could only be used to assess cells by the number of wrinkles they produced and not the exact amount of force. Some improvements have been made to provide a semi-quantitative measurement of the traction forces using wrinkling membranes (25,26). Callibrating the wrinkling of silicone membranes to read out quantitatively the forces causing the wrinkles would depend on knowing the exact thickness of the flame-hardened surface film and knowing how that thickness varies with position in the film. These quantities would be too difficult to measure. In addition the non-linear mechanics involved in computing force distributions from observed spatiotemporally chaotic wrinkling is such a difficult computation that no one has attempted it (27).

1.2.2 Traction Force Microscopy

The first, non-wrinkling, but still deformable substrate was made by crosslinking the silicone rubber in a glass chamber using a glow discharge device (Figure 4 *A*) (28). Small beads that were a micrometer in diameter were embedded on the elastomer surface. As a cell produced traction forces, the beads moved laterally on the silicone rubber due to deformation of the film. From the bead displacements, the force vectors cells exerted could be measured. At first, the local traction force was assumed to be linearly related to bead displacement. This incorrect assumption was later rectified by using non-linear elasticity theory of the deformation of a compliant film (29). This technique had limited sensitivity and proved to be able to measure traction forces only for highly contractile cells and so a limited range of cultured cells were able to be studied. Nonetheless, there were interesting findings on the migration of fish keratocytes using this early elastic film. These highly motile cells had been studied extensively to understand the mechanisms and mechanics of cell migration. Using the non-wrinkling silicone films, small bead displacements were observed at the leading edge of the cells and larger bead displacements at the rearward region.

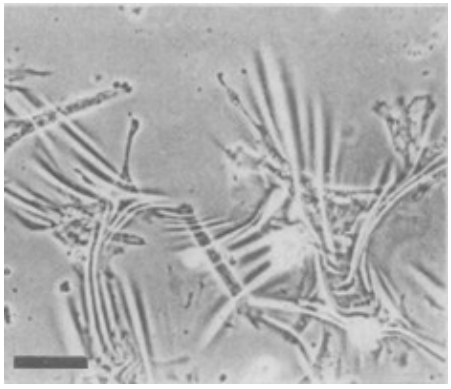

Figure 3. Silicone rubber membrane wrinkles due to the traction forces from several chick heart fibroblasts. Reproduced from (22). Bar: 100 μm.

The introduction of polyacrylamide gel in Yu Li Wang's laboratory to measure traction forces was a breakthrough in addressing the limitations of silicone film substrates because it provides a way to control the gel's stiffness by varying the mixing ratios between the acrylamide monomer and bisacrylamide cross-linker (Figure 4 *B*) (30,31). When a cell adheres to collagen-coated polyacrylamide gel and deforms it, the technique, referred to as

traction force microscopy (TFM), measures the movement of fluorescent nanobeads embedded in the gel (Figure 4 *C*). The displacement vectors are calculated by subtracting the positions of beads as they are deformed by a cell's traction forces from their original, undeformed positions once the cell has been removed. The traction stress field is then calculated from the displacement vectors using elasticity theory (32,33). Since the beads are randomly seeded into the gels, there can be uncertainty in solving for the appropriate traction forces in regions of low bead density. To address this, orthogonal arrays of fluorescent beads were made by electron-beam lithography and then patterned onto an elastomeric substrate (Figure 4 *D*) (34). Due to the even distribution of the bead markers, non-uniqueness, i.e. the number of possible solutions for the traction force vector field for a measured displacement field, was significantly reduced.

Despite some of the difficulties in analyzing traction forces using TFM, it has become widely used to study cells during migration and contraction. The traction stress distribution of migrating fibroblasts was found to have high forces at the leading edge of a cell whereas the middle and posterior of a cell had lower forces (Figure 4 *C*) (27). This nonuniform distribution of forces indicates that cells are pulled forward by contractile forces at the front of a cell. The role of high forces at the leading edge were also found to determine the change in direction during migration (35). Since the gels can have finely controlled stiffness, this has led to an important finding that cells sense and respond to the rigidity of the ECM (36). Cells on soft gels have less spread area, increased rates of motility and lamellipodia extension, small focal adhesions, and less phosphorylation of focal adhesion proteins as compared to those on rigid gels (30). Building from this finding, gels were created that contained both soft and rigid regions that were adjacent to each other (37). Cells were observed to migrate from the soft region to the rigid region (Figure 4 *E*). However, cells never crossed from the rigid region into the soft region. This phenomenon of directed migration due to substrate rigidity is called durotaxis. It was later found that biased persistent random walk and cell orientation with respect to the gradient were correlated with magnitude of stiffness gradient, but were independent of the absolute stiffness of the substrate (38). In addition, ECM stiffness has been found to affect cell

proliferation rate (39), the contractile development of cardiomyocytes (40), differentiation of stem cells (41), and invasiveness of breast tumor cells (42,43).

TFM has also been used to study the effect of ligand density and the involvement of traction forces in spreading. The spread areas of cells were tightly influenced by the ligand density on a surface, but had different increasing relationships depending on cell type and ECM ligand type (44-46). Traction forces also increased with spread area and ligand density, indicating that traction forces play a role in a cell's ability to extend its structure and maintain stable contact with a surface (46,47). These findings are in agreement with those from previous studies using surface adhesivity control, where cell spreading and adhesion strength were enhanced with increased ligand density (48-50). Furthermore, focal adhesion size, a measure of the degree of recruitment of cytoplasmic proteins and integrins, was found to increase with the local traction force acting at an individual adhesion (34). TFM has elucidated the two-dimensional (2-D) distribution of individual force vectors that a single cell exerted, but cells often reside in a three-dimensional (3-D) context. Fibroblasts in tissue-derived 3-D gel showed more effective attachment to the ECM than those in planar surface, spindle shaped morphology and higher proliferation rate (51). Some early works into measuring traction forces in 3-D have been implemented using TFM, but have not found dramatic differences are compared to traction forces in 2-D (52,53). One approach was to overlay a second TFM gel on top of a cell to look at tangential traction forces on the dorsal and ventral surfaces (52). It was found that the strength of these traction forces were similar to those observed in 2-D culture. Furthermore, even in 2-D, measuring the distortion of beads in a gel in all three directions using confocal microscopy from the cells lying on top of a gel surface allowed for finding that cells generate normal forces (to the gel surface) where their magnitude is similar to or slightly greater than the magnitude of tangential forces along the gel surface (53) (Figure 4 *F*). The three-dimensional forces that cells generate on 2-D surface imply that cells can use the forces in both normal and tangential directions to explore or remodel their microenvironment. While the dimensions used in this study was only semi-3D where cells were on top of flat gel, the full 3D force sensor was developed using hydrogel embedded with fluorescent beads (54). The bead displacement was measured via confocal

micrographs and finite element analysis. With fine resolution, the approach could recognize the forces exerted by tips of filopodial extension which showed strong inward tractions. Although these works provided an early framework to analyze 3-D traction forces, there are still many challenges and obstacles to create a feasible and analyzable assay to study the physical interactions of cells in 3-D (55,56).

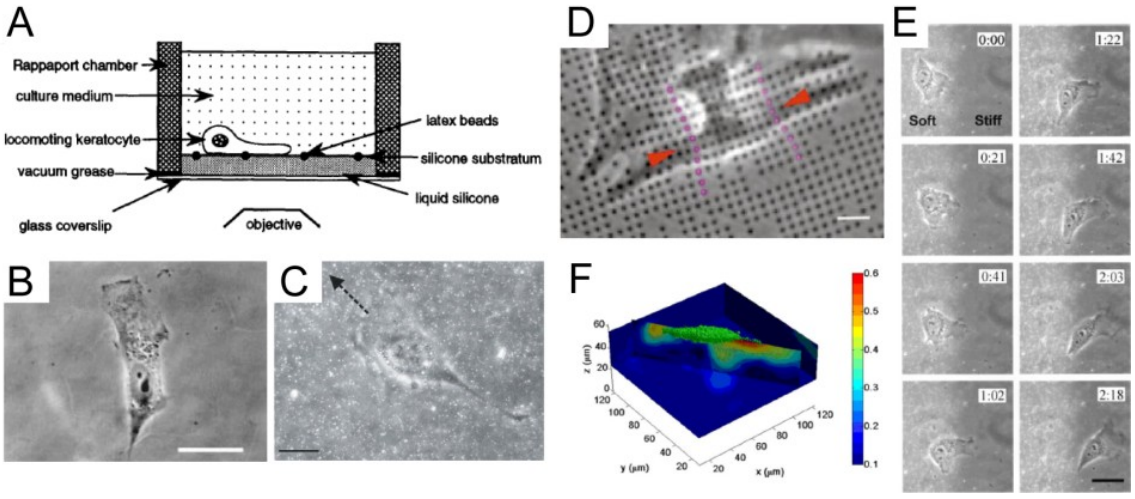

Figure 4. Traction force microscopy (TFM) is used to measure cellular forces. (A) Silicone rubber-based traction force microscopy has latex beads embedded on the surface of silicone film to report the distortion from traction forces. Reproduced from (28). (B) A fibroblast on a compliant polyacrylamide (PA) gel. Reproduced from (30). Bar: 10 μm. (C) Traction forces of a fibroblast migrating in the direction of the arrow were measured by the displacement of fluorescent nanobeads (0.2 μm diameter) which are seen as white dots embedded in the gel. Reproduced from (35). Bar: 20 μm. (D) Regular array of micropatterned dots on an elastomeric substrate shows contraction of a fibroblast (indicated by arrowheads). Reproduced from (34). Dots pitch: 2 μm, bar: 6 μm. (E) A fibroblast plated on a soft region of a gel migrated towards the rigid region. Reproduced from (37). Bar: 40 μm. (F) 3-D forces of a cell are measured by the displacement contour slice along the depth of a gel. Color bar: magnitude of total 3D displacement. Reproduced from (53).

1.2.3 Horizontal Cantilever Force Sensor

Continuous, deformable substrates such as silicone membranes or traction force microscopy gels have an inherent disadvantage in that a local force at a focal adhesion can cause a wide distortion of the substrate, which can in turn cause weaker, secondary forces that act externally at adjacent focal adhesions. Thus, the continuous nature of the substrates makes it difficult to isolate the local force at each focal adhesion. The need for tools to measure the local traction force uncoupled from forces exerted in adjacent regions brought about the development of microfabricated cantilevers (16,57-59). The first cantilever used

for a traction force study was a horizontal cantilever which was fabricated on a silicon wafer using surface micromachining fabrication (Figure 5 *A*) (58). The cantilever is deflected laterally when a cell pulls on the tip of the cantilever. The local traction force was determined by multiplying the displacement of the tip by the stiffness of the cantilever. This force calculation assuming linear elasticity might be over-simplified because the measured maximum deflection could be regarded as large deflection (e.g. 1.2 mm in deflection while length of cantilever was 0.18 mm). Interestingly, a migrating cell showed much larger force at its tail than those found at the front (58). This result is similar to traction forces of keratocytes measured on silicone rubber (28), but opposite to findings from fibroblasts on traction force microscopy (27,35). This inconsistency between the findings may be due to the difference in device design where horizontal cantilever can measure force at only one subcellular region at a certain time point whereas TFM can measure forces of a whole cell simultaneously. Typical morphology of crawling fibroblasts which feature with broad lamellipodia and narrow tail could be also one of the reasons that caused different force measurement because a low force measured at the leading edge using horizontal cantilever might be one among many force vectors that could be distributed throughout broad band of lamellipodia. Moreover, local difference in stiffness at the device might affect the force generation of a cell. That is, the rest of surface is extremely stiff while the cantilever pad is very flexible, so when the force at the tail was being measured, the leading edge was on very stiff surface which might possibly affect the force at the tail.

1.2.4 Micropost Arrays

One of the limitations of the horizontal cantilever was a fixed, single location of force sensing which only allowed for a force measurement in a single direction (orthogonal to the cantilever). Unlike TFM, it did not provide a 2-D map of traction forces acting at all adhesions of a cell. To address this issue, vertical arrays of elastomeric cantilevers were developed through a soft lithography and replica casting with a silicone rubber (57,59). Cells could spread out in a single 2-D plane by attaching to the tips of individual posts (Figure 5 *B*) (59,60). Like the horizontal cantilever, posts deflect independent of each other

and thus can report the local traction force based upon the stiffness of the posts. The stiffness of a post depends on the post's diameter to the power of four and varies inversely with the post's height to the power of three, along with Young's modulus of elastomer. The range of the post's deflection (~0.5 μm) can be regarded as small deformation considering the post's height (~7 μm). Thus, this force sensor has advantages of direct relationship between the deflection and the applied force, and capability to show force vector distribution of a cell simultaneously. The use of the array of vertical cantilevers has helped confirm that RhoA-signaling and focal adhesion size affect the total traction forces, as seen previously with wrinkling silicone membranes and TFM (59). Moreover, the stiffness of a post can be easily tuned by tailoring dimensions of a post, so contractile forces of a cell could be tested in response to different stiffness. As seen with 2-D TFM, contractile forces increased with the stiffness of the posts in an array, which indicates that the displacement at a focal adhesion does not vary inversely with post stiffness (17,36,61). It is worth noting that in 3-D, TFM has shown that the magnitude of bead displacements were constant for different gel stiffness (53). It may be that a cell has an integrin-associated mechanosensory feedback system that regulates the overall strain that actin and myosin produce within a cell. This hypothesis was further speculated by considering stretching of focal adhesion proteins (62).

One advantage of using silicone rubber for the posts is that posts can be made adhesive selectively by printing ECM on posts with a patterned stamp (63). Individual cells can be patterned on the posts with different sized square patterns (Figure 5 *C*), but pairs of cells, or monolayers of cells have been also patterned on posts with different shapes (59,64-66). Tan and colleagues have seen that cells with more spreading exerted higher contractile forces than those that are less spread, which agrees with findings from TFM studies by Reinhart-King *et al.* (47,59). Confinement of spread area on a force sensor can allow one to rule out the effect of spread area and focus on the influences of other factors on contractile forces. For example, cells have been observed to exert more force on stiffer substrates, but at the same time, they also spread more on stiffer substrate so the effect on contractile forces may be confounded by cell spreading (17,37,44,46,47). Techniques to isolate the roles of cell spreading and stiffness are used in Aim 1 because they are

beneficial to understand how cells regulate their contractile forces in response to each factor.

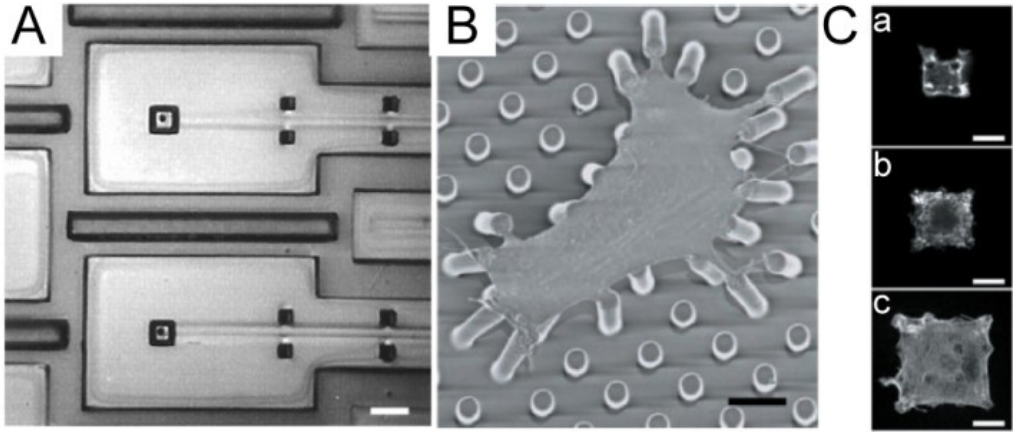

Figure 5. Microfabricated cantilevers for traction force study. (A) Microelectromechanical system (MEMS) based horizontal cantilever force sensor. The two pads are shown as two black squares that are bigger than eight smaller black squares. Connecting pads with its free ends, the cantilever levers are buried beneath the surface of the substrate. Reproduced from (58). Bar: 10 μm. (B) Scanning electron micrograph of a smooth muscle cell attached on tips of vertical post arrays. (C) Microcontact printing can be used to confine cell spreading. Actin image of cells patterned on (a) 2x2, (b) 3x3, and (c) 4x4 posts. Panels B and C reproduced from (59). Scales bars: 10 μm.

This concludes the review of literature on various ways of visualizing and/or quantifying the traction forces that motile cells generate. We turn now to this dissertation's results, which we partition into three major research aims each with its own interpretation and discussion subsections.

2. Aim 1: Delineating the Independent Influence of Substrate Stiffness and Spread Area on Contractile Forces and Focal Adhesion Size

2.1 Background

Mechanotransduction pathways associated with a cell's focal adhesions can affect its survival, fate, and behavior (7,36,67-69). Focal adhesions form a physical connection between a cell and its substrate, enabling cytoskeletal tension to be transmitted to the extracellular matrix as a traction force. A cell needs to transfer its cytoskeletal tension through its focal adhesion in order to migrate or contract (70), but it also uses cytoskeletal tension to probe its environment by means of integrin-related pathways that are activated by traction forces (62,71,72). As examples, cells need to produce cytoskeletal tension in order to sense the stiffness of their substrate, and cells evidently transduce the substrate stiffness they sense to regulate the progression of their cell-cycle or commitment towards specific lineages (41,42,73). Cytoskeletal tension also plays an essential role in the mechanotransduction of cell spreading and can influence proliferation and differentiation (74-76). The notion that cytoskeletal tension is indispensable for mechanotransduction further supports the idea that traction forces and focal adhesions play a key role in interpreting these mechanical cues.

Previous studies using deformable gels or micropost arrays have observed that substrate stiffness can strongly influence the generation of a cell's traction forces (37,42,61,77-80). Whatever these studies have contributed to the field of cell mechanics, they did not control cell spreading. This omission is critical because cells are able to spread to a greater extent when cultured on stiffer substrates (61,81). Moreover, a cell's spread area has a strong influence on the generation of its traction forces (47,59,80,82-85). The coupled relationship between spread area and substrate stiffness makes it difficult to conclude whether cells have higher traction forces due to the stiffness of their substrate or due to the effect of stiffness on cell spreading, which in turn implies higher traction forces. Understanding how stiffness and spreading affect traction forces can also shed light to the formation of focal adhesions, which are simultaneously regulators and products of traction forces. The initial assembly of a nascent adhesion complex leads to the generation of

traction forces, while their maturation into a stable, focal adhesion is strongly dependent on the strength of the local force transmitted through them (62,71,72). Focal adhesions have been observed to be larger for cells on stiff substrates versus those on soft substrates, but these findings have been mostly descriptive and without direct quantification of the correlation between size and force (61,78,86). Similarly, increasing spread area can promote focal adhesion growth (84,85). Given the underlying relationship between area and stiffness, we sought to decouple the role of stiffness and of spread area on traction force generation and focal adhesion growth.

We used microcontact printing of micropost arrays in order to control independently substrate stiffness, the total area a cell can occupy, and post density and then studied the effects of these three parameters on the generation of traction forces and focal adhesions. We assessed traction forces of a cell by analyzing the sum of their magnitudes (we call this 'total force', justification for using this quantity is in Materials and Methods) and average of their magnitudes ('average force'). We find that substrate stiffness leads to an increase in the total force and average force for a cell. Moreover, we determine that substrate stiffness can affect the generation of traction forces independent of cell spreading. We also find that cell spreading causes an increase in total force, but a decrease in average force. The opposing effect of cell spreading on total force and average force can be attributed to changes in the spatial distribution of traction forces. Furthermore, we conjectured that cell spreading causes an increase in the number of focal adhesions underneath a cell, so we used arrays with high or low density of posts in order to compare the effects of cell spreading versus the number of post underneath a cell upon the forces a cell generates. We found that the post density, but not cell spread area, strongly determines its total force and average force. Finally, we show that size of focal adhesions also increases with substrate stiffness and spread area and has trends that are closely matched with those observed for traction forces.

2.2 Materials and Methods

2.2.1 Cell Culture

Human pulmonary aortic endothelial cells (HPAECs, ATCC #CRL-259) were cultured in F-12K Kaighn's modified media (Hyclone) containing 50 μg/ml ECGS (Biomedical Technologies, Inc.), 100 μg/ml heparin (Sigma Aldrich), 10% newborn calf serum (Gibco) and were maintained at 37ºC in a humidified, 5% CO_2 incubator. Cells were seeded on post arrays and fixed after 14 h.

2.2.2 Traction Force Micropost Arrays

Arrays of elastomeric microposts were fabricated via replica molding using PDMS (Sylgard 184; Dow-Corning, Midland, MI) as previously described (87). The arrays were printed with 50 μg/ml fibronectin (BD Bioscience) using a PDMS stamp that had patterns of raised, square structures on its surface to confine cell spreading (SI Material and Method). The deflection of a post (δ), measured from photos taken through a 40X 1.3 NA objective lens, was used to report the local traction force (F) of a cell according to $F = k\delta = 3\pi r^4 E\delta/4h^3$ where k is a post's stiffness, r is its radius, h is its height, and E is the elastic modulus of PDMS. We expect this formula, derived from linear elasticity theory, to be valid for strains $(\delta/h) < .15$. The dimensions of post arrays including heights and diameters were measured using a scanning electron microscope (FEI Sirion) and summarized in Table 1 with their corresponding spring constant values. The elastic modulus of PDMS was measured according to ASTM standard D412. The dog-bone shaped PDMS specimens were baked for 3 h at 110 ºC. Mixing ratio of 10-to-1 for the base and the curing agent (Sylgard 184, Dow) was used for all arrays. The tensile test was performed on an Instron machine with a 1-kN load cell with extension rate of 0.2 mm/s. To obtain correct extension data, the neck region of each dog-bone specimen was marked with felt-pen and the distance between the marks was measured before and after extension. The stress vs. strain data were fitted with a linear best-fit line to determine that the elastic modulus of PDMS is $E = 2.49 \pm 0.17$ MPa.

Table 1. Dimensions and stiffness of micropost arrays. Values shown in the first two rows are means ± standard deviations. Values shown in the last two rows are means ± error as determined by the propagation of

uncertainty in the measurements for height and diameter of the microposts and elastic modulus of PDMS. From these measurements, arrays #1 through-#5 were found to have spring constants that were unique from each other ($p < 0.05$, ANOVA with Tukey's post-hoc test), while stiffness of arrays #4 and #6 were found to be similar to each other (tested with paired student t-test).

Array	1	2	3	4	5	6
Height (μm)	8.96 ± 0.36	7.44 ± 0.28	7.19 ± 0.22	7.45 ± 0.20	6.7 ± 0.13	5.62 ± 0.14
Diameter (μm)	2.14 ± 0.03	2.04 ± 0.06	2.22 ± 0.10	2.42 ± 0.05	2.5 ± 0.07	2.07 ± 0.05
Spacing (μm)	9	9	9	9	9	6
Post Stiffness (nN/μm)	10.7 ± 2.3	15.5 ± 3.6	24.1 ± 6.3	30.5 ± 6.2	47.8 ± 10	38.1 ± 7.9
Effective Shear Modulus (kPa)	0.79± 0.15	0.95 ± 0.20	1.42 ± 0.36	1.87 ± 0.35	2.64 ± 0.55	3.96 ± 0.75

Post arrays were stamped with flat stamps that had fibronectin (50 μg/ml, BD Biosciences) adsorbed onto the entire surface for unconfined cell studies and were stamped with flat stamps with square patterns of fibronectin for the confined cell area studies. To make the square patterns on the flat stamps, fibronectin was adsorbed and then dried with nitrogen onto a flat stamp. A second stamp with a picture-frame pattern (opposite to desired square patterns) was oxidized for 7 min UV-ozone (Jelight, Irvine, CA) and then placed into conformal contact with the fibronectin-coated flat stamp. This process, which we refer to as 'lift-off patterning', successfully removed fibronectin that was outside the square patterns of interest and left the protein inside the patterned square areas on the stamp. The square-patterned stamps were then used to stamp the tips of the micropost arrays that were oxidized for 7 min using UV-ozone. The use of flat stamps for all printing allowed for a more uniform protein transfer then stamps with a relief surface pattern. After micro-contact printing, substrates were immersed in 2 μg/ml 1,10-dioleyl-3,3,30,30-tetramethylindocarbo-cyanine methanesulfonate (DiI) solution (Invitrogen) for 1 h to stain the PDMS posts and then submerged in 0.2 % Pluronic F-127 solution (BASF) to block cell adhesions on the side-walls or base surface of the arrays (Figure 6).

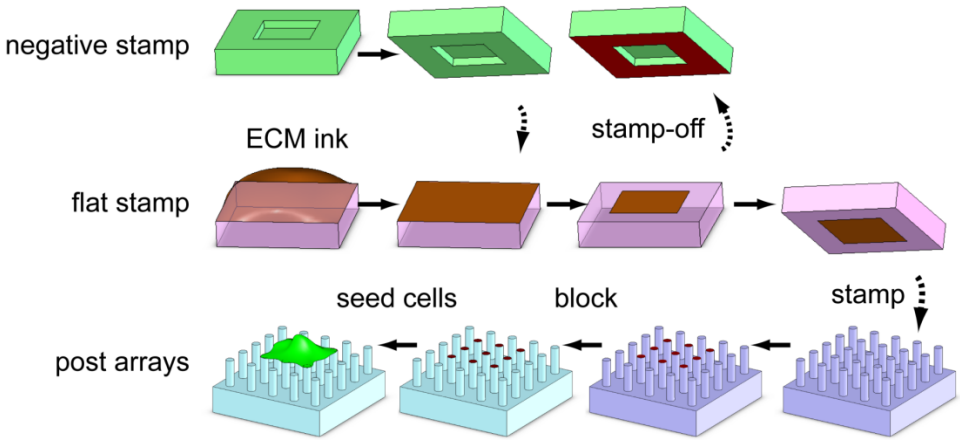

Figure 6. Stamp-off technique allows for efficient transfer of patterned protein on microposts. ECM protein is adsorbed on the flat stamp (second row) followed by taking off the marginal protein on a flat stamp with a negative stamp (first row), leaving ECM only in the desired pattern. Microposts are stamped with "Stamp-off"ed flat stamp followed by blocking side and bottom PDMS surfaces with a surfactant so that seeded cells can only bind to the posts where the ECM is.

2.2.3 Immunofluorescent Staining and Image Analysis

Fixed HPAECs were permeabilized using a Triton-X extraction protocol that removed the cellular membrane and Triton-soluble proteins but preserved Triton-insoluble structures such as the cytoskeleton and focal adhesions. Substrates were submerged in ice-cold cytoskeleton stabilizing buffer containing 10 mM PIPES (J.T.Baker), 50 mM NaCl (BDH), 150 mM Sucrose (J.T.Baker), 2mM PMSF (Electron Microscopy Sciences) and 3 mM MgCl (BDH), 20 µg/ml aprotinin, 1 µg/ml leupeptin, and 1 µg/ml pepstatin (all from G-Biosciences) at pH 6.8 for 1 min to reduce enzymatic activity before fixation. Substrates were then strongly permeabilized by treating for 2 mins in cytoskeletal stabilizing buffer containing 0.5% Triton X-100 solutions. Triton-extracted cells were then fixed with 4% paraformaldehyde (EMD Chemicals) in PBS, washed with PBS, blocked in 10% goat serum (Gibco), and incubated with primary antibodies against vinculin (Sigma Aldrich), and labeled with Alexa-Fluor 647 conjugated anti-IgG secondary antibodies (Invitrogen). F-actin was visualized by staining samples with phalloidin conjugated with Alexa-Fluor 488 (Invitrogen) and the nucleic acids in the nucleus were stained with Hoechst 33258 (Invitrogen). After immuno-fluorescence staining, samples were imaged with an inverted fluorescence microscope (Ti-E, Nikon) using a 60×, 1.4 NA, oil immersion objective with 400 ms exposure time for vinculin, 200 ms for actin and DiI-labeled microposts, and 7 ms

for nuclei at room temperature. Images were analyzed by using a custom-built code written (MATLAB, Mathworks) to find the centroids of the top and bottom of a post, to measure the spread area of a cell, and to determine the areas of the focal adhesions (60). The spread area of unconfined cells was measured based on the F-actin images of cells whereas those of confined cells were determined by the expression $((N\text{-}1)s+d)^2$, where N is the number of posts in each row, s is the center-to-center distance between the posts, and d is the diameter of a post. Not all cells filled the square pattern completely. I collected force data from cells that filled more than 90% of posts in a pattern for confined cell study. For quantifying overall force generation of a whole cell, I used the total magnitude sum of traction forces which was determined by summing the magnitudes of individual traction forces on all the posts the cell adhered to (for rest of Aim 1, I used the abbreviated term, 'total force' for referring this quantity). The reason why I chose total force as a read-out for overall contractility is to appropriately compare traction force measurement to total force used in TFM study by Reinhart-King *et al*. where the magnitudes of all force vectors in a whole cell were summed to study the relationship between spread area and the force generation (47). Average force per post ('average force' for the rest of Aim 1) was quantified as the total force divided by the number of posts under a cell. The average force is compatible with root-mean-square traction stress that Wang and colleagues used for quantifying the average contractility on gel (37) where they summed the magnitudes of all force vectors in a cell and divided by the spread area of the cell. We observed all these results after cells had come to equilibrium (in terms of area occupied and post deflections) so, for example, 'cell spreading' does not refer to the rate at which a cell spreads transiently but to the equilibrium area it occupies eventually. Achieving such equilibrium typically took about 4 hours.

2.2.4 Statistical Analysis

All data were obtained from at least three replicate experiments and error bars in all figures represent the standard error of the mean. Regression analyses for the data were performed using Igor (Wavemetrics), Minitab (Minitab, Inc.), and R code (www.r-project.org). R-squared values (R^2) were reported for both linear and nonlinear curve-fitting for the data.

We labeled data has having a strong correlation if $R^2>0.9$, a good correlation if $R^2>0.75$, a moderate correlation if $R^2>0.4$, and a weak correlation for $R^2<0.4$. SPSS (IBM Corp.) was used for multi-variable nonlinear fitting surfaces.

2.3 Results

2.3.1 Substrate Stiffness Affects Traction Forces and Cell Spreading

To examine the influence of substrate stiffness on traction forces, HPAECs were seeded onto five different types of arrays of posts, where each array had posts with a unique stiffness (Table 1). HPAECs spread on the arrays for initial 4 hrs after seeding. After spreading, about 40 % of cells still showed migration, but about 90 % of cells became non-migratory after 10 hr and even migrating cells showed non-changing spread area. These cells had different shapes and sizes and produced traction forces that deflected the posts centripetally (Figure 7, *A* and *B*). Total force and average force were analyzed for the cells free to spread to any area they selected on each array and compared with their spread area (Figure 8, *A* and *B*). A positive relationship between total force and spread area was found for cells on each of the arrays and the statistical correlation for each array was moderate-to-good (Figure 8 *A,* $0.40 < R^2 < 0.85$, Table 2). On the other hand, a negative relationship between average force and spread area was found for unconfined cells on each of the arrays, but the statistical correlations were weak ($0.01 < R^2 < 0.26$, Table 3). Thus, there is suggestive, but not strong evidence from linear regression analysis that spread area affects traction forces.

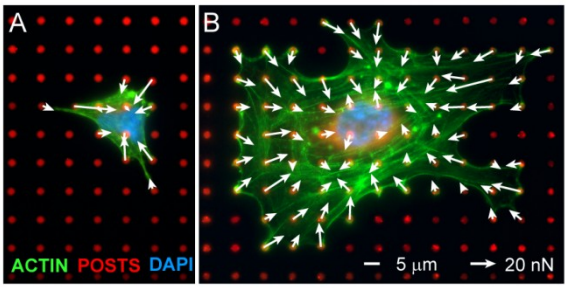

Figure 7. Human pulmonary artery endothelial cells (HPAECs) on micropost arrays with different stiffness. *(A-B)* Representative fluorescent micrographs and traction forces are shown for HPAECs on arrays of microposts with a spring constant of *(A)* k = 24 nN/μm and *(B)* k = 48 nN/μm (blue: DNA, green: actin, red: microposts). Traction forces were measured by analyzing the deflections of the posts and reported as a force vector (arrows).

We noted that the effect of spread area and stiffness may be interrelated since we observed that HPAECs tended to have increased cell spreading on the stiffer arrays (Figure 8 *C*) among cells not confined to square areas. If one considers the effective shear modulus of the arrays, the relationship between area and stiffness could be fitted to a power-law function, as has been reported previously (81). We found that the power-law function has a good fit to our data as well (Table 4, $R^2 = 0.83$). When cells were analyzed together regardless of their spread area, their average forces were found to increase with stiffness (Figure 8 *D*) and with a good statistical correlation (Table 5, $R^2 = 0.81$). Thus, these results indicate that the increases in stiffness of the microposts can induce cells to increase their average force, but stiffness can also influence cell spreading, which in turn contributes to lower average forces. As a consequence, we utilized a stamp-off printing approach to allow us to directly control cell spreading so that we could independently assess the effect of spreading and substrate stiffness on traction forces.

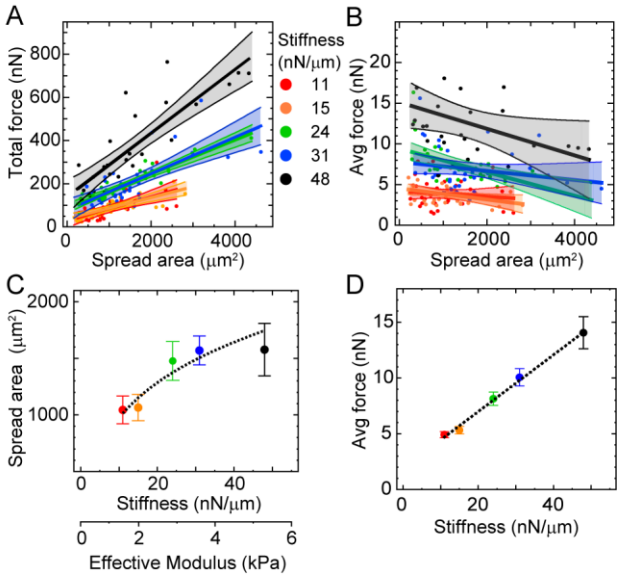

Figure 8. Traction forces versus spread area and substrate stiffness. *(A)* Total force increases with spread area for cells on arrays with different post stiffness. *(B)* Average force per post decreases with spread area. Each data point represents measurement from an individual cell. Straight, colored lines denote the linear least-squares fits to the data and shaded regions reports the 90% confidence interval for each fit. *(C)* Spread area versus substrate stiffness follows a power-law relationship (dashed line, Table 4). *(D)* Average force versus substrate stiffness has a positive linear relationship (dashed line).

Table 2. Linear regression analysis of total force of unconfined cells versus spread areas for each type of stiffness

Stiffness (nN/μm)	*Number of points*	*Slope (nN/μm²)*	*Slope Error (nN/μm²)*	*Intercept (nN)*	*Intercept Error (nN)*	R^2
11	30	0.056	0.013	27.86	15.76	0.40
15	33	0.050	0.008	35.59	10.22	0.55
24	31	0.079	0.006	86.34	10.72	0.85
31	35	0.085	0.013	76.79	24.80	0.55
48	26	0.148	0.018	137.12	35.48	0.72

Table 3. Linear regression analysis of average force of unconfined cells versus spread areas for each type of stiffness

Stiffness (nN/μm)	*Slope (nN/μm²)*	*Slope Error (nN/μm²)*	*Intercept (nN)*	*Intercept Error (nN)*	R^2
11	-0.00034	0.00053	4.21	0.64	0.01
15	-0.00068	0.00035	4.54	0.44	0.11
24	-0.00144	0.00042	9.41	0.74	0.28
31	-0.00056	0.00048	7.78	0.88	0.04
48	-0.00163	0.00093	15.12	1.82	0.12

Table 4. Fit coefficients of spread areas of cells as a power-law function of effective modulus (coefficient ± standard deviation). Coefficients were compared with rat aortic smooth muscle cells (RASMCs) from Engler et al. (2004). The values for RASMC were adapted by assuming that the polyacrylamide gel is a homogenous, isotropic linear elastic material with a Poisson's ratio of 0.5, such that $G_{eff} = E/3$, where E is the elastic modulus of the gel measured by atomic force microscopy nano-indentation.

$Area = BG_{eff}^{N}$		
	N	*B*
HPAEC – 12h	0.43 ± 0.11	1155 ± 72
RASMC – 4h	0.29	5501
RASMC – 24h	0.37	8258

Table 5. Linear regression analysis of average forces versus substrate stiffness.

Slope (μm)	*Slope Error (μm)*	*Intercept (nN)*	*Intercept Error (nN)*	R^2
0.254	0.027	1.89	0.47	0.81

2.3.2 Spread Area and Substrate Stiffness Affect Traction Forces Independently

We confined cell spreading with patterns of square islands with 441, 900, 1521, or 2304 μm^2 area. HPAECs on these arrays were confined to spread inside the square islands (Figure 9, *A-D*). Analysis of their traction forces revealed that the total force produced by the confined cells had a positive, linear relationship with spread area and was statistically identical to the fit for unconfined cells on the same substrate stiffness (Figure 10 *A*). Statistical correlations in the data were good-to-strong ($0.76 < R^2 < 0.98$, Table 6). Confined cells had average forces that decreased with spread area (Figure 10 *B*). A negative power law matched closely to the trends in the data and with strong statistical correlations ($AF = a*Area^b$ where $22< a < 241$, $-0.39 < b < -0.22$, $0.94 < R^2 < 0.99$, Table 6). For the previous data on unconfined cells (Figure 8 *B*), a negative power law could be applied, but the statistical correlation in the data was weak ($0.01 < R^2 < 0.48$, Table 7). Thus, controlling cell spreading by microcontact printing made it possible to demonstrate that a cell's total force increases with its spread area, but its average force decreases with spread area in a manner that is independent of substrate stiffness.

In addition, cells confined to the square patterns had average forces that increased with substrate stiffness (Figure 10 *C*). Statistical correlations in the data were moderate-to-good ($0.41 < R^2 < 0.88$, Table 6). This finding indicates that substrate stiffness can directly

influence traction forces whether or not cells spread. Taking together the results for average force versus stiffness and average force versus spread area, a multi-parameter fit could be applied to the data (Figure 10 *D*, Table 8). The surface fit incorporated a linear relationship for substrate stiffness and a negative power law relationship for cell spreading, resulting in a strong fit to the data ($R^2 = 0.97$). Thus, these results indicate that spread area and substrate stiffness can affect traction forces independently of each other.

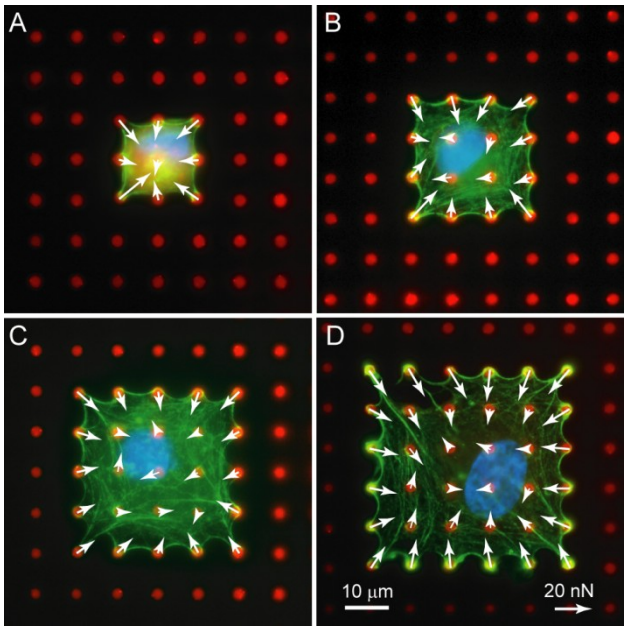

Figure 9. Representative micrographs and traction forces of confined HPAECs on printed areas of *(A)* 441 μm^2, *(B)* 900 μm^2, *(C)* 1521 μm^2, and *(D)* 2304 μm^2 (blue: DNA, green: actin, red: microposts).

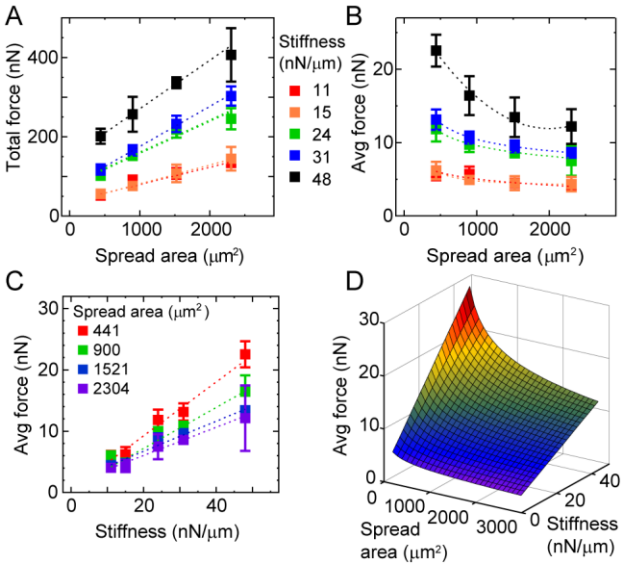

Figure 10. Spread area and post stiffness influence traction forces independently. *(A)* Total force increases with spread area for cells on each array type. *(B)* Average force decreases with spread area for each array stiffness. *(C)* Average force increases with substrate stiffness for each patterned area. Table S5 shows the number of cells that were measured per condition and R^2 values of the best-fit lines. *(D)* A multi-parameter fit of the data for average force shows they are a function of both spread area and stiffness. Table S8 shows the fit coefficient for nonlinear regression analysis.

Table 6. Sample size of cells studied in confined cell study and regression coefficients for total forces vs. area, average forces vs. area, and average forces vs. stiffness used in Figure 10. A total of 258 cells were measured. (* Pearson's r for power fit was done by performing linear fit in log-log scale).

Area (μm^2) / *K* (nN/μm)		*441*	*900*	*1521*	*2304*	*linear regression in* Figure 10 *A*			*regression in* Figure 10 *B* $AF = a*Area^b$		
						Slope ($nN/\mu m^2$)	*Intercept* (nN)	R^2	*a* (nN)	*b* (log nN / log μm^2)	R^2
11		13	16	13	9	0.043	36.32	0.98	27.14	-0.25	0.94
15		7	14	9	8	0.048	33.61	0.86	22.49	-0.22	0.94
24		8	14	9	6	0.081	78.40	0.96	51.70	-0.24	0.99
31		17	23	21	19	0.101	74.26	0.94	59.59	-0.25	0.99
48		20	13	12	7	0.122	148.5	0.76	241.0	-0.39	0.99
linear regression in Figure 10*C*	*Slope* (μm)	0.44	0.33	0.25	0.23						
	Intercept (nN)	0.47	0.49	1.81	1.46						
	R^2	0.86	0.67	0.88	0.41						

Table 7. Nonlinear regression analysis of average force of unconfined cells versus spread areas for each post stiffness using power-fit ($AF = a*Area^b$) shown in Figure 2 B. Pearson's r for power fit was calculated by performing linear fit on the data in log-log scale.

Stiffness (nN/μm)	*a*	*a Error*	*b*	*b Error*	R^2
11	8.27	8.33	-0.11	0.15	0.01
15	10.25	5.85	-0.15	0.09	0.11
24	92.87	36.8	-0.36	0.06	0.48
31	38.36	29.9	-0.24	0.11	0.08
48	99.94	67.8	-0.30	0.1	0.19

Table 8. Nonlinear regression analysis of average forces of confined cells with respect to substrate stiffness and spread area. The model fit function is $AF = (a*Area^b)*(c+d*Stiffness)$. Coefficients were calculated numerically for minimizing residuals by iteration with 61 model evaluations and 23 derivative evaluations.

a	*b*	*c*	*d*	R^2
0.69	-0.324	16.65	4.25	0.97

2.3.3 Spread Area Reduces Average Force Due to the Spatial Distribution of Traction Forces

We theorized that the increase in total force and decrease in average force with cell spreading is due to changes in the spatial distribution of traction forces. We compared data for cells with areas of 441, 900, 1521, or 2304 μm^2 and analyzed the average traction force per post (Figure 11 *A*). All of the cells analyzed were on arrays that had the same stiffness of 31 nN/μm. Color maps showed that traction forces were highest on posts at the corners and edges of the cells and were lowest on post within the interior regions. For cells confined to the smallest area (441 μm^2), their traction forces along the perimeter were consistently high in magnitude. However, for cells which were able to spread to a larger area, their traction forces were strongest at the corners and were only moderate along the edges. We found that the average traction force on a micropost did not correlate with its distance from the center of the cell. Instead, the average traction forces at the corners of cells with either small or large spread areas were similar in magnitude, even though their distances from the cells' centers were substantially different.

Histogram curves of the average traction force per post in Fig 11 were plotted to clarify how spread area leads to an increase in the total force, but also a decrease in the average force for a cell (Figure 11 *B*). We noted that the area under each curve is equivalent to the

total of force magnitudes for an average cell since the area under the curve is the sum of the traction forces. Consequently, analysis of the area under the histogram curves confirmed that cells with the largest spread area produced the most total force. In contrast, cells with a smaller area had a similar range of traction forces, but the area under their histogram curves was significantly less, and hence these cells produced less total force.

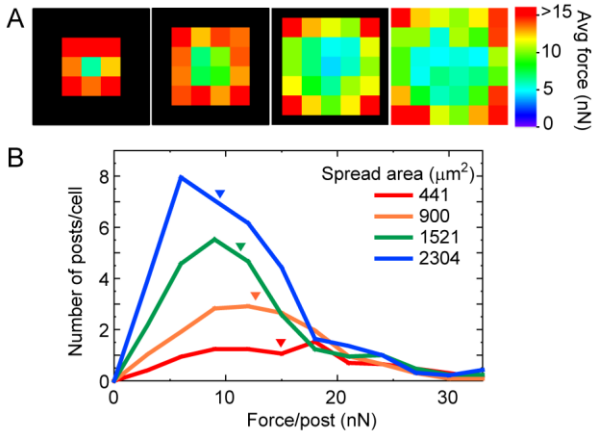

Figure 11. Spatial distribution of traction forces determines total force and average force for a cell. *(A)* Color map of average traction force at each post underneath cells on 441, 900, 1521, and 2304 μm^2 printed areas. High traction forces are found at the edges and corners of cells. *(B)* Histogram of traction forces for cells on each patterned area. The area under the histogram curve is equivalent to the total force of an average cell. Inverted triangles indicate average force for the data.

Additionally, the relationship between average force and spread area is evident by the skew in the distributions towards lower traction forces per post. Cells with the largest spread areas had a significant number of traction forces that were low in magnitude, which contributed to their overall, low average force (Figure 11 *B*). The color maps show lower traction forces are located predominately within the interior region of a cell. Likewise, cells with the smallest spread areas had only one post within their interior and had significantly more adhesions at the perimeter. This spatial distribution led to the highest average force amongst the different groups. Therefore, our data shows that total force for a cell increases with spreading due to the addition of more adhesions with the microposts, i.e. focal adhesions, but cell spreading decreases the average force of a cell by shifting the ratio of strong traction forces at the perimeter and weak traction forces within the interior of a cell. .

2.3.4 Focal Adhesion Area versus Spread Area and Substrate Stiffness

To examine the response in focal adhesions to substrate stiffness and spread area, we stained HPAECs for vinculin in order to quantify the area of their focal adhesions. Our data shows a weak, linear correlation between an individual focal adhesion's area and its local traction force (Figure 12, $0.2 < R^2 < 0.4$). However, we observed that the total area and average area of a cell's focal adhesions follow closely with the trends observed for traction forces: total focal adhesion area increased with a cell's spread area and with moderate-to-good linear correlations (Figure 13 *A*, $0.59 < R^2 < 0.98$, Table 9); average focal adhesion area decreased with spread area according to a negative power law relationship with moderate-to-strong correlations (Figure 13 *B*, $0.40 < R^2 < 0.99$, Table 10), and average focal adhesion area increased with substrate stiffness with moderate-to-strong linear correlations (Figure 13 *C*, $0.52 < R^2 < 0.92$). As before, a multi-parameter fit was applied to the data and had a good statistical correlation ($Average\ FA\ Area = (a \times Area^b) \times (c + d \times Stiffness)$, Figure 13 *D*, $R^2 = 0.84$, Table 11). Thus, these results demonstrate that in response to substrate stiffness and spread area, the total and average focal adhesion area of a cell correlates with its traction forces.

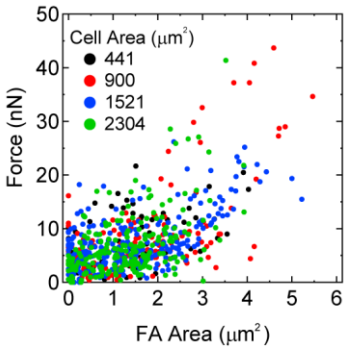

Figure 12. Individual forces at each post show a weak correlation with focal adhesion area regardless of cell spread area. Data of force and focal adhesion area are from cells on posts with 31 nN/μm.

As seen previously with traction forces, increased spread area caused the total area of focal adhesions to increase and their average area to decrease. To better understand the response to spreading, focal adhesion data for cells with 441, 900, 1521, or 2304 μm^2 area (Figure 14 *A*) were combined and the average focal adhesion area at each post was shown using a color-coding scheme (Figure 14 *B*). The spatial distributions of focal adhesion area were

seen to correlate with traction forces. Color maps showed that focal adhesions were large at the corners of cells and small within the interior regions. Histogram curves of the average focal adhesion per post were plotted and showed that the total area increased with spreading, while the average area decreased with spreading (Figure 14 *C*). These findings demonstrate that there is a close spatial relationship between traction force and focal adhesion area in response to stiffness and area.

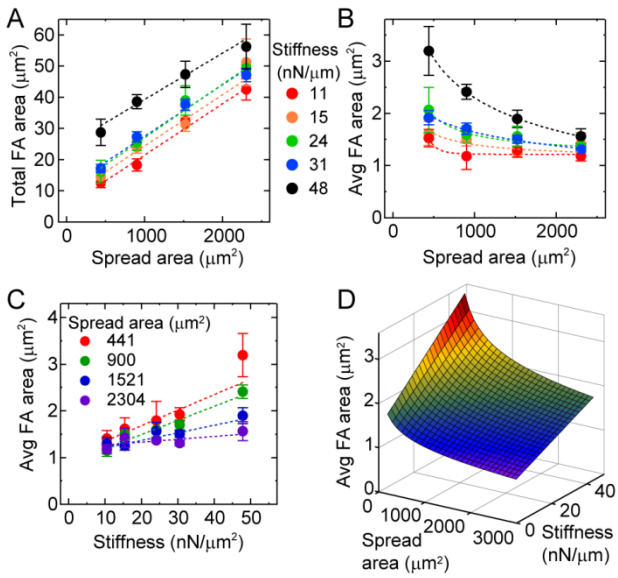

Figure 13. Spread area and post stiffness influence focal adhesion area independently. *(A)* Total focal adhesion area increases with spread area. *(B)* Average focal adhesion area decreases with spread area. *(C)* Average focal adhesion area increases with substrate stiffness. Table S9 shows R^2 values of the best-fit lines. *(D)* A multi-parameter fit of the data for average focal adhesion area shows they are a function of both spread area and stiffness. Table S11 shows the fit coefficient for the nonlinear regression analysis.

Table 9. Regression coefficients for total focal adhesion (FA) area vs. cell area and average FA area vs. cell area used in Figure 13 A and B.

Area (μm^2) / *K* (nN/μm)	*linear regression in* Figure 13 *A*			*regression in* Figure 13 *B* *FA Area = a*Area^b*		
	Slope (1)	*Intercept* (μm^2)	R^2	*a*	*b*	R^2
11	0.017	4.92	0.90	3.57	-0.14	0.76
15	0.016	7.86	0.59	4.69	-0.17	0.40
24	0.017	9.73	0.88	6.56	-0.20	0.96
31	0.017	10.96	0.98	8.27	-0.24	0.98
48	0.015	24.35	0.96	48.98	-0.44	0.99

Table 10. Regression coefficients for average FA area vs. stiffness used in Figure 13 C.

Cell area (μm^2)	*linear regression*		
	Slope (μm/nN)	*Intercept* (μm^2)	R^2
441	0.033	1.02	0.52
900	0.030	0.88	0.92
1521	0.016	1.04	0.79
2304	0.006	1.20	0.48

Table 11. Nonlinear regression analysis of average FA area of confined cells with respect to substrate stiffness and spread area as shown in Figure 13 D. The model fit function is *AverageFAArea* = (a*Area^b)*(c+d*Stiffness). Coefficients were calculated numerically with 28 model evaluations and 11 derivative evaluations.

a	*b*	*c*	*d*	R^2
2.59	-0.253	2.14	0.06	0.841

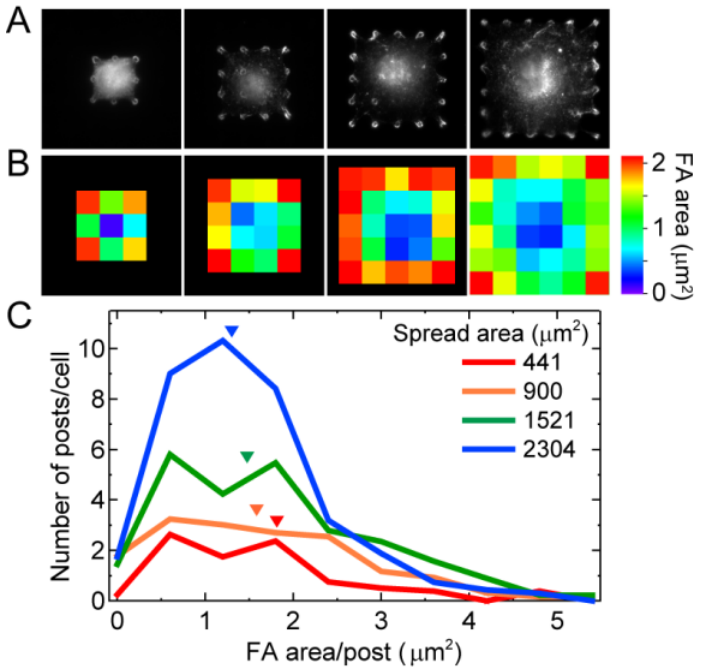

Figure 14. Focal adhesions are large at the corners and edges of cell, but small at its interior. *(A)* Vinculin images of cells on each pattern area. *(B)* Color map of average focal adhesion area. *(C)* Histogram of focal adhesion area per post for cells on patterned areas. The area under the histogram curve is equivalent to the total focal adhesion area of an average cell. Inverted triangles indicate average focal adhesion area for the data.

2.3.5 Post Density Affects Traction Forces and Focal Adhesion Area

A question that arises from the spatial distributions of traction forces and focal adhesion areas is whether spread area affects contractility or whether it acts by increasing the number of focal adhesions underneath a cell. To address this question, we used a pair of arrays which had spring constants that were similar, but which had different post densities (arrays #4 and #6, Table 1). Cells with the same spread area (1521 μm^2), but with a different number of posts underneath them were compared (Figure 15, *A* and *B*). Conversely, cells on the same number of posts, but with different spread areas were examined (Figure 15, *C* and *D*). Our results indicate that for cells with similar spread areas, those that were attached to more posts produced larger total forces (Figure 16 *A*, $p < 0.08$) and lower average forces (Figure 16 *B*, $p < 0.005$). Similar results were seen for cells with 441 μm^2 area (Figure 16, *E* and *F*, $p < 0.09$ and 0.03, respectively). On the other hand, cells that occupied the same number of posts but had different spread areas produced total forces and average forces that were statistically identical to each other (Figure 16, *C* and

D). A similar trend was seen for cells on 16 posts, but with different areas (Figure 16 *E*). For all cells examined, total forces were seen to increase with the number of posts underneath a cell, whereas their average forces were seen to decrease with the number of posts (Figure 16 *E* and *F*).

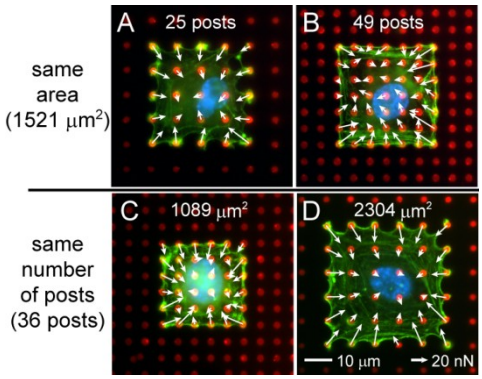

Figure 15. Representative immunofluorescence images and force vectors of cells with spread areas of 1521 μm^2 and occupying *(A)* 25 posts or *(B)* 49 posts and cells occupying 36 posts and with *(C)* 1089 μm^2 or *(D)* 2304 μm^2 area.

To confirm post density affects the close, spatial relationship between focal adhesions and traction forces, we analyzed the total focal adhesion area and average focal adhesion area as before. Post density was found to have an effect on focal adhesion area that mirrored its effect on traction forces. Cells with the same spread area had total focal adhesion areas that increased with post density (Figure 17 *A*), whereas their average focal adhesion area decreased with post density (Figure 17 *B*). Cells on the same number of posts but with different spread areas had total and average focal adhesion areas that were statistically identical (Figure 17, *C* and *D*). The trends for total focal adhesion area and average focal adhesion area versus the number of posts they occupied was observed for all cells examined (Figure 17, *E* and *F*). Thus, these results indicate that cell spreading does not directly influence traction forces. Instead, it appears that cell spreading increases the number of individual focal adhesions underneath a cell, which in turn affects the total and average force for a cell as well as its total and average focal adhesion area.

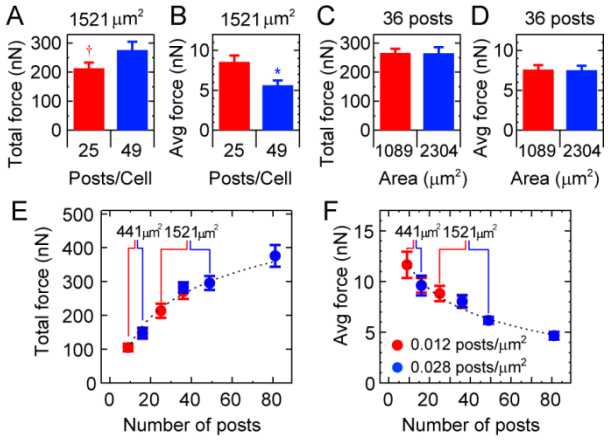

Figure 16. Traction forces depend on post density rather than spread area. For cells with similar spread area, *(A)* total forces increase with post density and *(B)* average forces decrease with post density († denotes p=0.08). *(C)* Total force and *(D)* average force are similar for cells occupying the same number of posts but with different areas. *(E)* Total force increases logarithmically with the number of posts that a cell occupies (R^2=0.99). *(F)* Average force per post decreases according to a power law fit with the number of posts underneath a cell (R^2=0.92).

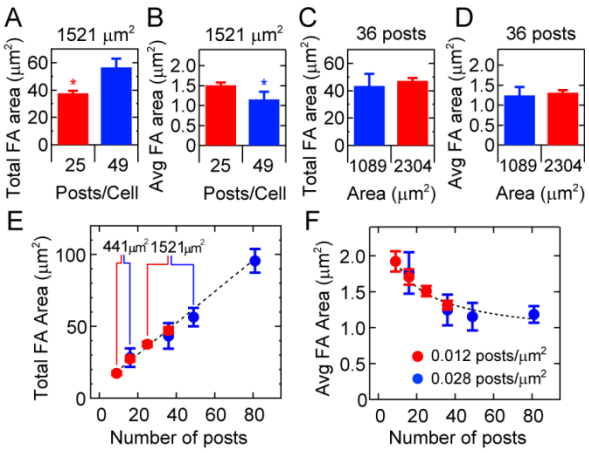

Figure 17. Focal adhesion area depends on post density rather than spread area. For cells with similar spread area, *(A)* total focal adhesion area increase with post density and *(B)* average focal adhesion area decreases post density. *(C)* Total focal adhesion area and *(D)* average focal adhesion area are similar for cells occupying the same number of posts but with different area. *(E)* Total focal adhesion area increases linearly with the number of posts that a cell occupies (R^2=0.91). *(F)* Average focal adhesion area decreases according to a power law fit with the number of posts underneath a cell (R^2=0.92).

2.4 Discussion

2.4.1 Mechanosensing of Substrate Stiffness

We observed that substrate stiffness can influence the traction forces and focal adhesions of cells with confined spread areas. This finding is novel because it reveals that substrate

stiffness affects traction forces and focal adhesions regardless of how much a cell can spread. The effect of substrate stiffness and cell spreading on traction forces has been previously investigated by Califano *et al.* through statistical analysis of unconfined cells using substrates of different stiffness (80). They inferred that the effect of stiffness and cell spreading on traction forces were independent, but they did not control cell spreading. With microcontact printing, however, we were able to demonstrate with compelling results that traction forces, as well as focal adhesion, are affected by stiffness in a manner that is independent of cell spreading.

It has been proposed that in order for cells to sense the stiffness of a substrate, they need to use their traction force to pull at their focal adhesions until they reach a displacement of 100-150 nm (36,62,78). It is thought that their displacements cause conformational changes in focal adhesion proteins, which in turn activate signaling pathways that play a role in sensing substrate stiffness (88,89). With our data, we can determine the average displacements at a cell's focal adhesions from the slopes of the best-fit lines in Figure 10 *C*. We find that average displacements in our data are significantly higher (230-440 nm, Table S6) than those reported previously by Saez *et al.* (130 nm) (78). This difference suggests that the displacement required for mechanosensing is significantly greater than previously expected. Moreover, we also find an inverse relationship between spread area and average displacement: the average displacement for cells with 441 μm^2 area is 440 nm, whereas for cells with 2304 μm^2 areas it is 230 nm.

2.4.2 Cytoskeletal Differences at the Periphery versus Interior

Our results demonstrate that the totals and averages for traction forces and focal adhesions change with cell spreading. These aggregate measurements have a strong contribution from traction forces and focal adhesions at the periphery of a cell and a weak contribution from forces and adhesions at the interior regions. Previously, Rape *et al.* patterned cells with various aspect ratios and found that a cell's traction forces and focal adhesions increase with distance from the geometric center of the cell (85). Our data is partially consistent with this observation for we see large forces and focal adhesions located at the corners of confined cells. However, our data also shows that traction forces and focal adhesions do

not correlate with the absolute distance from a cell's center. This discrepancy is apparent if one compares the heat maps for cells with 441 versus 1521 μm^2 areas or the heat maps for cell with 900 versus 2304 μm^2 (Figures 11 and 13). Here, cells confined to the smaller area are seen to have traction forces and focal adhesions at their periphery that are much larger than those found at the same geometric distance, but within the interior region, of the larger spread cells.

These comparisons indicate that traction forces and focal adhesion sizes are not a linear function of distance from the center of a cell. Instead, it is more likely that they are affected by the different degree of cytoskeletal organization at the periphery versus the interior. Larger traction forces and focal adhesions at the periphery have been attributed to the presence of circumferential actin bundles, which likely generate a majority of the force produced during cell spreading (90,91). From a study using AFM which measured a stiffness of a dorsal surface of a cell, the periphery, and in particular, the corners of cells confined to square islands have a higher degree of cell stiffness, which is indicative of increased cytoskeletal organization at this region (92). The notion that cytoskeletal organization leads to greater traction forces is supported by observations that cell stiffness correlates with higher traction forces (93). Moreover, computational models of active cell contraction have predicted that large traction forces occur at the periphery of cells in correspondence with its higher degree of actin-myosin assembly (1,94). Thus, our results lend support to the notion that there are regional differences in the cytoskeleton that affect the generation of traction forces and focal adhesions.

2.4.3 Cell Area versus Focal Adhesion Density

Our finding that traction forces increase with cell area is consistent with previous studies (47,59,77,83,85). However, we show that cell area does not affect traction forces directly, but instead acts by increasing the number of posts underneath a cell. This finding is particular to micropost arrays, which allow us to limit the number of focal adhesions for a cell by controlling post density and its spread area. Previously, McGarry *et al.* used a bio-chemical-mechanical model and predicted that the average force for cells should decrease

with the number of posts underneath them (94). Subsequently, our data confirms that average forces decrease with the number of posts (Figure 17 F).

Since partitioning the cell with more number of posts produced a larger total force and a smaller average force than those in the less partitioned cell, the way we partition the area a cell spreads across into sub areas can be regarded as important. In other words, one might think that the dependency of the magnitude of forces on the number of posts is a weakness of our methodology because it means that the details of an artificial environment affect the measurement of forces. We agree with this argument if the cell is continuum and contracts by some amount of internal tension isotropically in case of a square cell. In this case, measuring deflections from more points in the cell can result in obtaining larger magnitude sum of forces than measuring deflections from smaller number of points. The centripetal orientation of force vectors and gradient of force magnitude from the center to the edge of the cell might be a clue for advocating that the cell is mechanically continuum because these features can be modeled with a continuum model with some internal tension such as thermal stress. In this case, we could further analyze the distribution of post deflection vectors with traditional continuum mechanics such as Cauchy's stress tensor.

However, as we reviewed in the general introduction, a cell's major force-generating structures, i.e. actin cytoskeletons, are discrete in its organization, albeit its complexity in connectivity with each other, ending with discrete points of focal adhesions. One of the main goals in this study is to investigate the role of the number of focal adhesions in force generation and focal adhesion area independently of cell spread area. Studies using a continuous substrate like a gel or glass usually have let cells form as many focal adhesions as they can form in a certain spread area. These continuous substrates might provide more natural environment for cells, but the question about if the large total forces found in cells with large spread area compared to small cells come from truly the area or the number of focal adhesions which are formed in the area has remained open. Our micropost methodology solves this question by providing means to control the number of focal adhesions. In the work of Reinhart-King *et. al* (47), total magnitude sum of forces were quantified to study relationship between force and spread area which was fit linearly. However, if the cell increased its number of focal adhesions (which was not measured in

the actual paper) linearly with its spread area, then the average force per a focal adhesion could be an inverse relationship with the spread area or the number of focal adhesions. We further speculate that if a cell in on more densely packed posts such that it has more sub-partitions, there is probably some asymptotic limit of average force or total force, which remains as a future work with smaller scale of post arrays that have smaller post-to-post spacing but the same effective stiffness as the posts we currently used.

It has been argued that local ligand density, defined by a density of ligands in a few hundred nanometers of ECM area, has a stronger effect than global ligand density, defined by a density of ligands in a several micrometers of ECM area, on the formation of focal adhesions (95). However, by changing post density, we were able to increase the global ligand density without affecting the local ligand density on the tips of the posts. We find that by changing post density, there is an increase in total focal adhesion area and a decrease in the average focal adhesion area. Thus, these results suggest that when local ligand density is sufficient high for focal adhesion formation, global ligand density can still have an effect on focal adhesion size.

2.4.4 Role of Global Stiffness

We have postulated that reducing the spacing between posts increases the effective shear modulus of the array, which in turn creates a globally stiffer environment for the cells (96). Consequently, if we define the global stiffness as a ratio of a resistant force compared to applied forces, not on an individual adhesions underneath a cell, but on a continuous area of the cell where more than one adhesions can form such a way that the larger number of adhesions in the same area of a cell has more resistance than the smaller number of posts, it could be argued that the effect of post density on traction forces and focal adhesions is due to a change in the global stiffness of the arrays. This argument holds some merit because cells had larger total forces and larger total focal adhesion areas on the globally stiffer arrays (Figures 16 *A* and 17 *A*). On the other hand, this argument is unsuccessful when one considers the effect of global stiffness on the average force and average focal adhesion area. Based on our findings on local substrate stiffness (Figure 10, *A* and *C*), one would expect that increasing global substrate stiffness should increase the average force and

average focal adhesion area in cells. However, we find that globally increased stiffness causes lower average forces and adhesions (Figures 16 *B* and 17 *B*). It may be that global stiffness and local stiffness provide different mechanical cues that affect a cell's traction forces and focal adhesions.

2.4.5 Close Spatial Relationship for Traction Forces and Focal Adhesions

There have been several studies that have shown a direct correlation between individual focal adhesion size and local traction force (34,59,97). Other studies have shown inconsistent results on the relationship between traction forces and focal adhesion areas (59,98,99). However, our data indicates that traction forces and focal adhesion areas show similar trends in response to mechanical cues. We find that traction forces and focal adhesions have a closely matching relationship for cells on substrates of different stiffness, spread areas, or post densities (Figures 11 vs. 13, 16 vs. 17). Implication underlying this finding can be that focal adhesions, as anchoring structure that supports a certain amount of tension, increase their size, possibly by sensing resistant forces from a substrate, for an increased traction force. Since the traction forces we measured are an output of transmission of internal tension to the post arrays, this close correlation indicates that traction forces and focal adhesions might be tightly coordinated in order to properly maintain the cytoskeletal tension against a substrate.

2.5 Conclusions and Future work

The magnitudes of contractile forces a cell generates and exerts on a planar substrate comprising a regular square lattice of round post tops, change when we vary any of (1) the stiffness of posts, (2) the density of posts, or (3) the area a cell spreads out to cover. These contractile forces must therefore be regarded as functions of at least these three variables which our experiments are the first to vary independently. Matrix stiffness and spread area affect the regulation of contractile force, which plays a role in cell functions such as proliferation and differentiation (41,42,73-76). We resolved a previous shortcoming in studies where cells were free to spread on substrates of different stiffness. By controlling the available matrix area, we could find: 1) contractile forces increase in response to

substrate stiffness in a manner that is independent of spread area, 2) individual forces were distributed non-uniformly over a cell, 3) contractile forces depended on the number of adhesions underneath a cell, rather than actual area. We also showed focal adhesion area responded to the substrate stiffness and the cell area in the same way that contractile forces showed.

I consider the work in this aim complete because I clarified the biophysical relationships among substrate stiffness, cell spread area, micropost density, contractile forces and focal adhesion area with strong data. To understand more deeply the mechanism by which cells respond to both factors, it would be beneficial if we do: 1) 3D confocal image reconstruction of a cell on each confined area to identify cytoskeletal structure and correlate the forces with types of stress fibers and phosphorylated myosin (dorsal, ventral, and transverse as introduced in (91)), 2) patterning cells on posts with only periphery of a cell adhered to posts and comparing the forces with that of filled-patterned cells, 3) patterning other ECM protein to investigate differential role of various ECM constituents on contractility. These works may illuminate the structural mechanics of a cell that could result in contractile response with respect to cell area or adhesion spacing.

3. Aim 2: The Multiphysics Model of Contractility during Migration

3.1 Background

Cell migration plays an essential role in wound healing, vascular remodeling, immune response, and cancer metastasis (100,101). To better understand how each of these biological events occurs, a wide range of mathematical and computational models have been developed (102-105). Cell migration in these models was commonly simulated using a partial differential equation based on diffusion physics since importance was placed on the number of cells that were chemically guided to a spatial point. On the cellular level, however, migration involves the integration of dynamic changes in focal adhesions, cytoskeletal structures, and chemical and mechanical signals from the extracellular matrix. These changes are incorporated into a cyclic progress where a cell extends its leading edge, forms new adhesions at the front, contracts its cytoskeleton, and releases adhesions at the rear (106,107).

While mechanical and/or chemical gradients in the environment can affect the direction that a cell migrates (37,89,108-110), it is the traction forces that actually drive the migration. Once a cell protrude its leading edge using protrusive force from actin polymerization (111) and form focal adhesions at its leading edge, myosin-based traction forces are transmitted to a substrate via these adhesions to pull a cell in the direction of a cell's movement. Moreover, the adhesions at the rear need to detach in order to allow a cell to move forward. While adhesion release depends on interactions among actin, actin-binding proteins, signaling molecules, and enzymes (112,113), traction forces may also contribute to the release by breaking adhesive bonds at the rear (106,107). Whole cell models have been developed that incorporate the signaling and mechanics in actin polymerization, myosin contraction, and adhesions dynamics (114-117). These models have provided significant insights into trajectory of cells during directed cell migration, e.g. *chemo*taxis, *hapto*taxis, and *duro*taxis. However, modeling of cell migration would be more accurate if it could describe the traction forces that cells generate in addition to locomotion.

The post arrays have yielded many interesting findings about a cell's contractile response to mechanical changes in the substrate, and in turn, these findings have helped to generate new ideas in modeling cell mechanics. In particular, a bio-chemical-mechanical model has been developed and used to explain the findings from post array studies (1,94,118). The model consists of an activation signal that elicits actin polymerization and myosin light chain phosphorylation, the degree of assembly of actin and myosin into a stress fiber, and a force-velocity relationship between contraction rate of stress fibers and cytoskeletal tension that is akin to Hill's muscle model. However, this model did not incorporate the formation, growth and disassembly of focal adhesions which is critical for cell migration probably because Deshpande and colleagues focused on contraction of non-migrating cells.

Our goal in Aim 2 is to evaluate the appropriateness of the bio-chemical-mechanical model in quantitatively predicting the migration of cells on arrays of posts in both one- and two-dimensions. The model takes into account a fundamental feature of cell migration: traction force generation. In addition, I added the role that adhesion dynamics has in regulating cytoskeletal tension for better mimicking migration. These properties are expressed during three main steps in cell migration: initial contraction up to a steady state, a second activation of contractility after new adhesion formation, and release of adhesion at the trailing edge of the cell. Hone and colleagues have found that the protrusive force cannot be detected unless there are some posts which have larger height than other posts (119). Thus, I assumed that leading edge occurs during the initial contraction phase and it does not affect the deflection of posts. I also assumed that the focal adhesion forms in the beginning of the second phase which causes a new activation signal for whole cell. This model predicts key spatial and temporal features cellular contractility during migration, which includes large traction force at the leading and trailing edges and a contractility drop during the release phase.

3.2 The Model

This section discusses the modeling of contractility-based migration examining each component in the contractility model, its biological relevance, and assumptions. The

computational methods that solve the contractility model of cell migration are described for one-dimensional (1D) and two-dimensional (2D) simulations.

3.2.1 Model for Contractility

The contractility model used in this study is based on the bio-chemical-mechanical model previously developed (118). For the purpose of our study, however, the model has been adapted to suit cell migration mechanics by adding a few more assumptions which we discuss in the following section. Briefly, the contractility model consists of three components: a time-decaying activation signal, actin-myosin assembly level, and a linearized version of the force-velocity equation for actin-myosin force production. These components create a set of ordinary differential equations for the independent variable of a post deflection, 'x_i' at each i-th post from the post at the left end called the 1-st post. I used a finite-element model of a cell in which each cell is partitioned into an array of contiguous stress fibers, joined end to end with the joins atop the posts.

3.2.1.1 Activation Signal

An activation signal C_i, which is a function of time and position, that subsequently triggers actin polymerization and myosin phosphorylation starts the contractile activity within a cell. This signal represents signaling activities of Rho GTPases, which are one of the main regulators of the cytoskeleton (120). The strength of the activation signal is mathematically given by

$$C_i = \exp\left(\frac{-(t-t_i)}{\theta}\right) \tag{3.1}$$

where θ is the decay constant of the signal, and t_i is the time of the onset of an activation signal. This equation is based on the assumption that once an activation signal is received, the strength of the signal suddenly rises to a fully activated state ($C = 1$) and then decays exponentially as the activating molecules start to dissociate from the receptors to which they are bound ($C \rightarrow 0$).

3.2.1.2 Stress Fiber Assembly Level

The assembly level η represents the degree to which the filamentous actin and phosphorylated myosin are incorporated into a stress fiber, which is fundamental to the contractile performance of a migrating cell. As used here, η_i is the ratio of the amount of assembly for a i-th stress fiber compared to its maximum possible level ($0 \leq \eta_i \leq 1$). The rate of assembly level, which depends on the activation signal and the amount local tension, is represented by

$$\dot{\eta}_i = \left[(1-\eta_i) \frac{C_i k_f}{\theta} \right] - \left[\left(1 - \frac{T_i}{T_0} \right) \eta_i \frac{k_b}{\theta} \right] \tag{3.2}$$

where T_i is the local tension in the i-th fiber, T_0 is the isometric tension, and k_f and k_b are the forward and backward rate constants for assembly and disassembly of a stress fiber, respectively. The isometric tension T_0 is defined to be proportional to the assembly level of the stress fiber, $T_0 = \eta T_{\max}$, where $T_{\max}$ is the maximum isometric tension possible in a stress fiber. Lastly, the over-dot denotes differentiation with respect to time.

As defined in the first term in equation 2, the rate of stress fiber assembly decreases with current assembly level η due to a limited number of free monomers of actin and unphosphorylated myosin within the cell. With the same reasoning, the second term in equation 2 describes the rate of stress fiber disassembly and increases with current assembly level η. If equation 2 was set-up as a simple first-order kinetic equation where $\dot{\eta}_i = (1-\eta_i)k_f / \theta - \eta_i k_b / \theta$, then the assembly level η would increase with increasing time until it reached an equilibrium state that is determined by the values of k_f and k_b (Figure 18, *blue line*). Likewise, if equation 2 only incorporated the role of Rho GTPases in stress fiber assembly, then the rate would be given by $\dot{\eta}_i = C(1-\eta_i)k_f / \theta - \eta_i k_b / \theta$. In this case, the exponential decay in the activation signal would cause the first term to converge to zero, and as such, the disassembly rate would dominate until there was no longer a stress fiber (Figure 18, *green line*). Finally, incorporating the role of tension into the second term encompasses the findings that tension can promote stress fiber formation (121) and myosin catch bonds (122) and that compression can inhibit actin polymerization (123,124). The assembly level in equation 2 is seen to rise and drop because of the decay in the activation

signal, but then stabilizes at a particular steady-state level. The differential equation models in this dissertation approach steady state levels asymptotically as t → large and therefore never actually reach a steady state. In my calculations, here and below, however, I used a practical criterion to identify "steady states" as states within 99% of the asymptotes they were approaching. This response is because the tension that developed in the stress fiber causes the disassembly term to go to zero while the assembly term also goes to zero because of the activation signal (Figure 18, *red line*). In this simulation, the forward and backward rate constants were fixed at $k_f = k_b = 5$, and the decay constant was set to $\theta = 1$. The stabilizing effect of tension on stress fiber assembly is a simplification of a complex set of different processes (13). In fact, it is reasonable to consider that high levels of tension can rupture stress fibers, but the intracellular tensions associated with migration are considered here to be far lower than the forces that would cause a cell to pull itself apart.

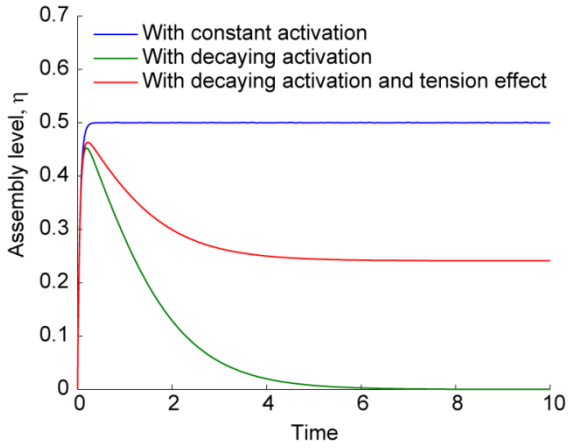

Figure 18. Simulation results of assembly level for three illustrative cases. Forward and backward kinetic rate constants $k_f = k_b = 5$ are used for all simulations

3.2.1.3 Force-Velocity Relationship

Stress fibers in nonmuscle cells are assumed here to have a similar isotonic relationship as myofibrils in skeletal muscle due to similarities between nonmuscle myosin II and muscle myosin II. Hill's model states that contractile tension of tetnanized muscle is inversely related to its shortening velocity (125). Here, this inverse relationship was used for the relationship between non-muscle cytoskeletal tension and shortening velocity of a stress fiber,

$$(v+b)(T+a)=b(T_0+a) \tag{3.3}$$

where v is the rate of change in length of a stress fiber, T0 is the isometric tension in the fiber, a is a constant of shortening heat, and b is a constant that has a relationship with a by

$$b=\frac{\eta v_0}{k_v T_0}a \tag{3.4}$$

where v_0 is the maximum rate of change, and k_v is a velocity constant that relates the reduction in tension due to the shortening velocity (v/v_0). A plot of the tension T with respect to the contraction rate v shows that tension decreases as shortening velocity increases (Figure 19). Here, it is noteworthy that the isotonic velocity, which is the shortening velocity at zero tension, is limited by the assembly level and the velocity constant. Since assembly level changes during contractile activity, the isotonic shortening velocity changes in accordance. This is reasonable because if there were no stress fibers assembled ($\eta = 0$), then it would impossible for a cell to contract, and likewise, there is maximum isotonic velocity when all stress fibers are fully assembled ($\eta = 1$).

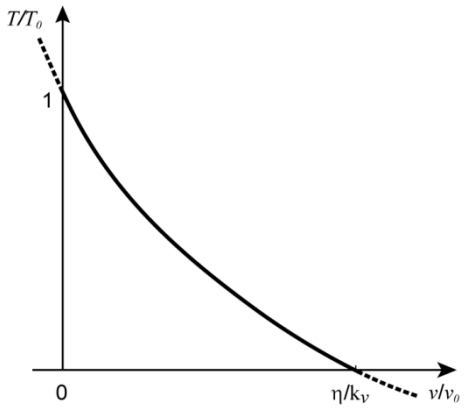

Figure 19. Hill's muscle model used in the migration model (126)

3.2.2 Migration Mechanics

To extend this contractility model, we incorporated several key events into the time-course of the migration model. First, a relaxed, stationary cell was activated to contract until it reached a steady state condition. Second, a new adhesion to a post was formed during the extension phase that triggered the reactivation of C, causing whole cell contraction until it reaches a new steady state. Lastly, in order to complete the first steps of migration,

mechanical release of an adhesion at the rear of a cell was conducted. Since the current ordinary differential model has no distinction between the front and the back of the cell, we arbitrarily chose the orientation of the cell migration. These settings are designed to illuminate how each step affects cellular contractility in a spatial and temporal fashion.

3.2.2.1 One-Dimensional (1D) Simulation

In this study, we consider a cell lying on an array of posts, in which all posts have the same stiffness and the spacing between posts is uniform. The force equilibrium equation about the n^{th} post is given by

$$T_{n+1} - T_n - k_s \Delta x_n = 0 \tag{3.5}$$

where Δx_n is the deflection of the n-th post, T_n is a tension at the n^{th} stress fiber segment which is defined to be to the left of the n^{th} post, and M is the total number of posts underneath a cell. Since there is no stress fiber attached to the left of the first post, by definition the tension in this stress fiber segment is zero ($T_1 = 0$). The relationship between the rate of deflection of the i^{th} post and the rate of change in length of a stress fiber can be written as

(3.6)

In order to solve the equations 3.1- 3.6 listed above, the tension in the n^{th} stress fiber is rewritten from equation 3 as

$$T_n = a \frac{T_0(\eta_i v_0 - k_v v_i)}{k_v T_0 v_i + \eta_n v_0 a} \quad . \tag{3.7}$$

Equations 3.5, 3.6 and 3.7 lead to a nonlinear system for the displacement x_i. It was solved with two steps where the displacement x_i and the tension T_i were updated in sequential manner.

For assembly level, equation 2 was used to determine the level of assembly in each stress fiber segment. To express this in indicial notation, the equation for the assembly level can be written as,

$$\dot{\eta}_i = \left[(1-\eta_i)\frac{Ck_f}{\theta} \right] - \left[\left(1-\frac{T_i}{T_0} \right) \eta_i \frac{k_b}{\theta} \right] \qquad 1 \le i \le M. \qquad (3.8)$$

These equations were solved with explicit Euler's method (127) with initial conditions of $\eta_i = T_i = x_i = 0$ at $t = 0$. Once at steady state, the extension phase was begun where the number of total posts was increased by one. Simultaneously, a new activation signal C was begun in the whole cell. Once a new steady state was reach, the rear adhesion to post 1 was removed by setting the tension in the stress fiber T_2 to zero. The simulation was run until a new steady state in contractility was reached. Model parameters regarding 1D simulation are listed in Table 12.

Table 12. Model parameters for 1D simulation

Parameters	Description	Values	Units
k_s	Spring constant of a post	3	nN/μm
k_v	Force reduction coefficient with respect to strain rate	1.5	
$\dot{v}_0$	Maximum extension rate of a stress fiber	0.4	μm/s
T_{max}	Maximum tension that a stress fiber can generate	1	nN
k_f	Assembly rate constant	3	s^{-1}
k_b	Disassembly rate constant	2	s^{-1}
θ	Time decay constant	1	s

3.2.2.2 Two-Dimensional (2D) Simulation

A 2D computational model of the migrating cell was constructed using a finite element method, just as the above one-dimensional model was constructed using a finite element method. In the model, a cell was assumed as an isotropic, continuous material in which the stress fiber formation at any nodal point which is a midway point between two adjacent posts depends on the stresses at the position. As before in the 1D simulation, equation 1 is used to describe the activation signal. However, the assembly level in 2D has been generalized as

$$\dot{\eta}_{i,j} = \left[(1-\eta_{i,j})\frac{C_{i,j}k_f}{\theta} \right] - \left[\left(1-\frac{\sigma_{I(i,j)}}{\sigma_0} \right) \eta_{i,j} \frac{k_b}{\theta} \right], \qquad (3.9)$$

where σ_0 is the isometric stress, $\sigma_0 = \eta\sigma_{max}$. The stress σ_{max} is the maximum that a stress fiber can bear. Here, $\sigma_{I(i,j)}$ is the average first stress invariant, $\sigma_{I(i,j)} = (\sigma_{x(i,j),active} + \sigma_{y(i,j),active}) / 2$ where $\sigma_{x(i,j),\ active}$ and $\sigma_{y(i,j),active}$ are the active normal stresses in the *x*- and *y*-directions in i-th and j-th node in each direction, respectively. The first stress invariant was chosen as a parameter representing the tensional state at a certain node because it depicts the level of total stress in a cell and is independent of orientation or coordinate system. In 2D simulations, the constitutive equation for stresses σ_x and σ_y incorporates components of passive elasticity from the cytoskeleton and cytoplasmic structures and components of active stress derived from the Hill-like force-velocity relationship,

$$\sigma_{p(i,j)} = \sigma_{p(i,j),active} + \sigma_{p(i,j),passive} \tag{3.10}$$

where,

$$\sigma_{p(i,j),active} = \eta_{i,j}\sigma_{max}\left(1 + \frac{k_v\dot{\varepsilon}_{p(i,j)}}{\eta_{i,j}\dot{\varepsilon}_0}\right) \tag{3.11}$$

$$\sigma_{p(i,j),passive} = \frac{E\left((1-\upsilon)\varepsilon_{p(i,j)} + \upsilon\left(\varepsilon_{q(i,j)} + \varepsilon_{r(i,j)}\right)\right)}{(1+\upsilon)(1-2\upsilon)}. \tag{3.12}$$

Here, *p(i,j)* is either the *x*- or *y*-direction in the (i,j)th node where a state of plane stress is assumed, *q(i,j)* and *r(i,j)* are the two Cartesian directions other than *p*, $\dot{\varepsilon}_{p(i,j)}$ is the strain rate in the p^{th} direction, $\dot{\varepsilon}_0$ is the maximum strain rate that a stress fiber can bear, σ_0 is the isometric stress in a stress fiber, kv is a force constant that determines how much stress is generated from given strain rate, *v* is Poisson's ratio of a cell, and *E* is its elastic modulus. A linear isotropic stress-strain relationship is assumed for the passive elasticity of the cell. The structural analysis for stress-strain evaluation has been combined with a weak-form-based ODE solver for the stress fiber assembly level as a module in Comsol Multiphysics 3.5a (Comsol Inc.). A cell supported between four bracket-shaped posts has been chosen for its simplified dimensional constraints.

To simulate cell migration, the model has been solved separately for each step of the process – contraction, extension, and release – and the simulation did not progress into the next stage until the stress in the cell approaches the approximate steady state. Here we describe a simulation of a cell crawling diagonally from the upper right to the lower left in the figure. To start the contraction phase, the cell was bound to three posts at its corners

(Figure 20, *left*). The steady state values for assembly level, deformation, stresses, and strains were used as initial conditions for the following extension phase. At the start of the extension phase, a new adhesion to a fourth post was created and a new activation signal C was applied to the entire cell (Figure 20, *middle*). As before, the steady state values were subsequently used as the initial condition for the simulation during the release phase. Here, the post at the trailing edge (upper-right) was removed, and the simulation was run to find a new contractile state (Figure 20, *right*). Quadratic Lagrange elements in Comsol were used in the simulation. The side length of the square-shaped cell was drawn to 9 μm while the thickness was set to be 1 μm. The model parameters used in 2D simulation are listed in Table 13. In the simulation, the cell begins to contract from completely unassembled state, i.e. $\eta = 0$ at $t = 0$.

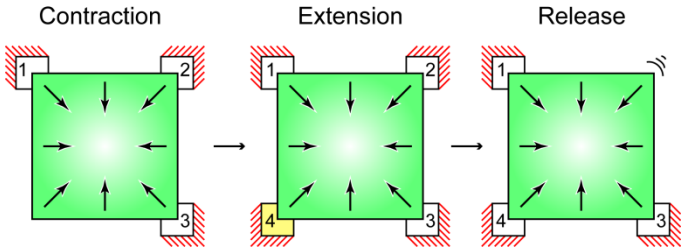

Figure 20. Schematic illustration of cell migration for two-dimensional (2D) simulations performed in Comsol. Initially the cell contracts against posts 1-3 and then migrates by extending towards post 4 and releasing from post 2.

Table 13. Model parameters for 2D simulation.

Parameters	Description	Values	References
E_{cell}	Young's modulus of a cell	250 Pa	(128)
ν_{cell}	Poisson's ratio of a cell	0.36	(129)
E_{sub}	Young's modulus of a substrate	1000 Pa	-
ν_{sub}	Poisson's ratio of a substrate	0.49	-
k_v	Force constant with respect to strain rate	1.5	Same as 1D
$\dot{\varepsilon}_0$	Maximum extension rate of a stress fiber	0.2 s^{-1}	(118)
σ_{max}	Maximum stress of a cell	25 Pa	-
k_f	Assembly rate constant	5 s^{-1}	-
k_b	Disassembly rate constant	3 s^{-1}	-
θ	Time decay constant	1 s	Same as 1D

3.3 Results and Discussion

3.3.1 1D Simulation Results

As was previously discussed in the model's description, a cell was simulated to undergo a contraction, extension, and release phase over the course of the simulations on posts (Figure 21 *Top*). The first steps in migration of a cell on one-dimensional posts are predicted to cause post deflections that are spatially and temporally different from each other. In the contraction phase, post deflections increased until they reached a steady-state where the activation signal decayed to a negligible level and tension developed in the stress fibers kept the assembly level from returning to zero. Spatially during the contraction phase, the largest deflections were observed at the edge posts (posts 1 and 6). Contrarily, the inner posts experienced smaller deflections because tensions in the stress fibers attached to the post were mostly counterbalancing with each other and left only small resultant forces to be supported by the posts. The result at the initial contraction phase shows the validity in our model because similar patterns of post deflections were observed in previous experimental findings (59,94,130).

At the beginning of the extension phase, the new post (post 7 in Figure 21) started to deflect toward a cell center. The previous edge post (post 6) also deflected inward due to the influence of the new activation signal. But shortly thereafter, the deflection of post 6 decreased along with the remaining inner posts (post 2 to post 5) in order to counterbalance the new deflection at post 7. Interestingly enough, the post on the trailing edge (post 1) deflected more noticeably in the centripetal direction, which resulted in its force being largest among all posts. This finding agrees with direct measurements of traction forces where the highest forces were observed at the tail region of a migrating cell (58).

When the adhesion to the post at the tail was released, a sudden rearrangement of forces occurred to satisfy force equilibrium. Post 2, which had previously been adjacent to the tail, deflected further inward due to the loss of counterbalancing force from the released stress fiber. Likewise, the rest of posts also deflected toward the leading edge in a transient fashion as the stress fibers within the cell adjusted to the new levels of tensions. The resulting steady state deflections were no longer symmetric about the geometric center of

the cell as had been previously seen in the contraction phase. Furthermore, simulation of the second step of migration – by one more extension and release – revealed that a cell shows similar contractile behavior as seen in the first cycle of migration (Figure 21).

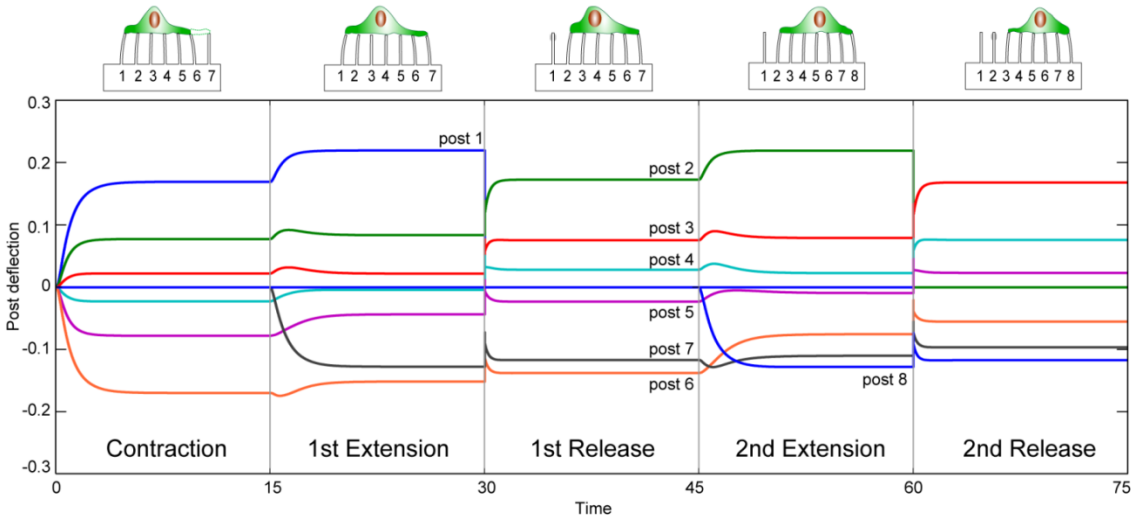

Figure 21. One-dimensional (1D) simulation of cell migration on an array of posts. (*Top*) Schematic illustration depicts a cell during each phase of migration. The deflection of the posts by the cell's traction forces have been added as a visual aid and are not drawn to scale. The black arrowheads denote the point of force equilibrium where the sums of the forces on either side of the cell are equal. (*Bottom*) Results of post deflections from the 1D simulation show that there are spatial and temporal changes in traction forces in each phase of migration.

To quantify the contractility of the whole cell over time, the strain energy stored in the posts was calculated (*solid line*, Figure 22). As expected, the strain energy rose rapidly during the contraction phase until it reached a steady state. The strain energy increased again following the second activation signal during the extension phase. Interestingly, contractility dropped upon adhesion release to a level that was lower than the steady-state during the contraction phase. This response during the release phase was due to the sudden loss in tension at post 1 that subsequently caused disassembly of stress fibers until a new assembly level and corresponding tensional state were reached. What is surprising is that the model indicates that a large amount of energy is lost during a migration cycle. Furthermore, simulating multiple migration cycles can cause the overall contractility to significantly decrease. Indeed, previous experimental studies have reported that adhesion detachment in a cell causes a remarkable loss of tension (26,131), strain energy (132) and phosphorylated myosin light chain(133). This result necessitated us to hypothesis a means

for a cell to recover its state of contractility to a steady level. We speculated that another activation signal may occur upon release to compensate the loss of contractility. Performing a new simulation of a complete migration cycle with this third activation signal revealed that a cell can recover its loss in strain energy in order to maintain a constant degree of contractility during migration (*dashed line*, Figure 22). In addition, it is noteworthy that an increase and drop in strain energy on extension and release, respectively, occurred during the second cycle of migration, and the strain energy loss is larger than the drop during the first release. Furthermore, the energy is restored back to the level at the first contraction phase when there is an additional activation signal on release. Interestingly it means a cell transfers energy from the cell's stress fibers to the elastic posts and then forever loses that energy when it detaches from a post. The post recoils back to its straight up configuration and dissipates its elastic energy to heat. The power turns out to be 2.7 attowatt, 3.3 attowatt. This power has nothing to do with the work a cell must do to propel itself through the viscous fluid that would surround it. It represents the rate the cell must do work on the substrate to crawl.

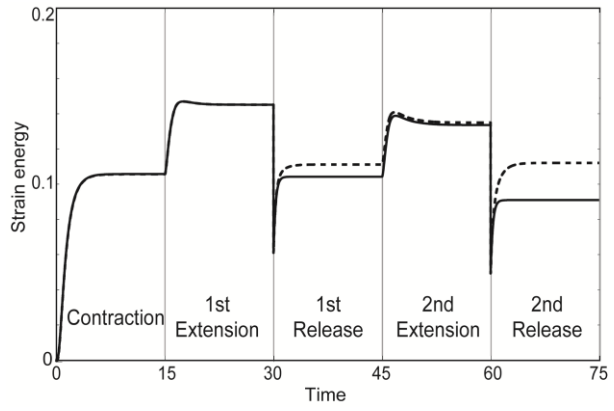

Figure 22. Strain energy in the posts by a cell's contraction in the 1D simulation. Strain energy increases during the extension phase, but drops during the release phase to a level below steady-state contraction (*solid line*). If another activation signal is initiated at the start of the release phase (*dotted line*), then strain energy can be restored to levels that are close to steady-state contraction.

3.3.2 2D Simulation Results

To check and compare the 1D simulation to what is observed *in vitro*, we constructed a 2D simulation of migration (Figure 23). A spatial plot of the assembly level during the contraction phase showed a high concentration of stress fibers in the vicinity of the

adhesions to the three supporting posts, which is in agreement with a previous model of cells contracting on posts in 2D (Figure 23 *A*) (1). These focal-like concentrations of stress fibers are also shown in the extension and release phases, although their degrees of magnitude are different. In the extension phase, the stress fibers that touch all four post adhesions have high value of eta, i.e. high assembly levels whereas the adhesions lose their stress fiber assembly levels upon the release of an adhesion.

To quantify the overall contractility of the cell, the strain energy of the posts were obtained by integrating the strain energy density over the area of each support (Figure 23 *B*). The contractility showed a remarkably similar behavior as observed in the simulation of 1D cell migration. Contractility was shown to increase upon new adhesion formation, but dropped upon release (*black line*). After release, an oscillation in strain energy occurs that quickly dampens and reaches steady state (*dotted line*). This oscillation is triggered to a large strain rate caused by removal of boundary condition at the tail region and dampened by transient interplay between constitutive equation (equation 3.10) and the linearized force-velocity relationship (equation 3.11) where a positive strain rate from the removal of a boundary condition affects the active stress to become larger than its isometric level which causes a large negative strain rate in the next time step which affects the active stress to be very low, close to zero. Remaining passive stress in the cell can then cause a large positive strain again that continues to a new loop of oscillation. It is noteworthy that the steady state level after the release is, again, below the steady state level in the contraction phase. As before, we applied a third activation signal at the time of release and found it was essential to maintaining cytoskeletal tension during migration (*gray line*). Therefore, the results from both our 1D and 2D migration simulations strongly suggest that cells use biochemical activation to supplement the loss in cytoskeletal tension upon adhesion release.

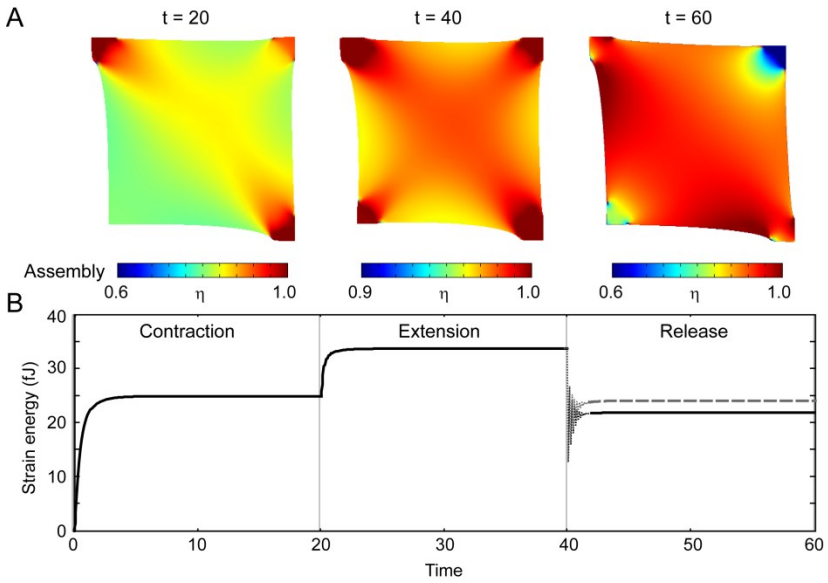

Figure 23. Simulation results from the 2D migration model. (A) Spatial map depicting the assembly level at the end of each phase of migration. (B) Strain energy in the posts increases during the contraction phase, increases further in the extension phase, and drops significantly during the release phase (*black line*). If an activation signal is added at the start of the release phase (*gray line*), contractility is restored to levels similar to those in the contraction phase. Oscillation at the beginning of release phase is due to transient interplay between constitutive equation (equation 3.10) and the linearized stress-strain rate relationship (equation 3.11). See the text for detailed explanation.

3.4 Discussion

We have described a computational model to address how cellular contractility is coordinated as a cell migrates across an array of posts. The model simulated the traction forces generated during one complete cycle of migration by incorporating activation signals that occurred during initial contraction and new adhesion formation, kinetic models of stress fiber assembly, and biomechanical relationships between traction stress and shortening velocity. Thus, this approach is fundamentally different from the diffusion-based models or the lumped parameter models for cell migration because it allowed for a close comparison between the results of the model and the measurements of traction forces seen with post arrays and deformable substrates. Although the simulations focused on cell migration on post arrays, the framework of the model can be applied to analyzing the contractile process of cell migration in a variety of cell assays or environments.

A cell migrating on a 1D post array had several spatiotemporal features commonly seen in cell migration: large forces at the trailing and leading edge and the forward progression of

the cell body. Interestingly, the large forces at the two edges of the cell were predicted solely by the condition of force equilibrium. This feature was in agreement with the finding the tail of a cell and the leading edge have the largest forces (35,58). Several studies have shown that cell retraction is closely related to increased levels of phosphorylated myosin that coordinates with tyrosine phosphorylation and calpain activity to release the adhesions at the rear (134-139). Together with weakened adhesion strength, the high force at the tail during the extension phase can contribute to rear detachment by overcoming the adhesion strength of focal adhesion (140).

Quantification of strain energy in both 1D and 2D simulations showed that there was a drop in cell contractility upon release. A loss of contractility has been observed in migration studies where tail retractions led to a dramatic reduction in deformation of the substrate (26,131). Moreover, strain energy exerted by migrating cells has been seen to have cyclic nature where strain energy in a substrate increases upon a new adhesion formation and decreases upon adhesion release (132). In addition, cell detachment with trypsin can significantly reduce the amount of phosphorylated myosin, although the result was obtained from whole cell detachment (133). Taken together, it is likely that new adhesions cause an increase in contractility and tail retraction causes a loss, but it is uncertain whether contractility falls below steady state levels seen in stationary cells.

Ultimately, our simulations raise an important question: how can a cell maintain its contractility after it takes its first step? When another activation signal was added to the release phase in both models, overall cell contractility could be maintained at levels similar to those in stationary cells. A study that performed a simultaneous visualization of Rho GTPases activity showed that Cdc42 and Rac1maintain a high activity level during the release phase and continue until the next protrusion cycle (141). Considering that Cdc42, like RhoA, can affect cytoskeletal contractility via myotonic dystrophy kinase-related Cdc42-binding kinase which phosphorylates myosin to regulate cell retraction (142), our simulations suggest that a cell might regulate another signaling pathway to maintain its tensional homeostasis during migration.

3.5 Conclusions and Future work

The work in this aim is the first time that anyone has used bio-chemo-mechanical model to study spatiotemporal dynamics of forces during a cell migration on post arrays. The simulation of migration using multiphysics contractility model provides a molecular perspective on how to interpret *in-vitro* or *in-vivo* cell migration.

The bio-chemical-mechanical model for migration can be used to examine a wider range of cell migration processes that are affected by mechanical factors in a substrate such as *duro*taxis, *hapto*taxis, and *topo*taxis (37,49,143). The model can also include the cytoskeletal forces that regulate adhesion maturation since they are driven by the balance of actin polymerization and actin-myosin contraction (140). Eventually, these efforts will need to incorporate the nature of cytoskeletal protrusions in order to adequately simulate a cell's advancement to a new adhesion spot and thereby provide important motility properties like velocity and orientation in addition to the traction forces predicted thus far.

In order for the model to crawl spontaneously, it should incorporate local integrin receptor concentration(114) or focal adhesion dynamics (144). We update the model in Aim 3 with addition of adhesion strength which represents the level of aggregation of focal adhesion proteins and integrins. This update allows the cell to form a new adhesion at the leading edge or release the adhesion at the tail. Force-dependent adhesion growth and force-induced adhesion release are also included in the adhesion dynamics subsection of aim 3.

4. Aim 3: Mechanics of 1D Fibroblast Migration on Microposts

4.1 Background

Cell migration, as with other biological functions, requires an integration of a number of molecular interactions that lead to movement of a cell. Numerous molecular players including focal adhesions, cytoskeletal filaments, myosin and signaling molecules eventually lead to active mechanical forces and change in mechanical properties of the cell. While traction forces at the cell front drive cell migration by pulling on the rear ends, helping them detach from the substrate, but the organization of the intracellular structures can affect the way the forces are transmitted through the cells. Complex cytoskeletal organization can determine the mechanical properties of the cell such as viscoelasticity. There have been numerous studies which have assumed, tested, or modeled the mechanical properties of cells or isolated stress fibers (145-149). However, how mechanical properties of a cell, along with traction forces, are regulated during its migration has been unknown. To study these phenomena, appropriate experimental and computational platforms are needed.

The multiphysics model that was developed in Aim 2 encapsulates biochemical and biomechanical activities in a cell. The model has predicted several features regarding spatiotemporal force dynamics and overall contractility during migration, but the most important contribution that the model can give is a framework for interpreting forces of migrating cells. In the model simulation, post deflections are an outcome of several inter-related factors: an activation signal, stress fiber assembly level, and velocity-dependent force generation govern the contraction of leading edge whereas the overall viscoelasticity of the cell cytoplasm and intracellular structures determines the propagation of the forces to the remaining posts. Data in our in-vitro experiments can be interpreted with perspective of these components from which specific characteristics about traction force and mechanical properties of the cell behind its migration can be elucidated. The goal of Aim 3 therefore is to understand biomechanics of live cell migration *in-vitro* related to the multiphysics model.

Fibroblasts have been used previously for studying force dynamics during migration (35,37,58,150). They move slowly and generate larger traction forces than fast-moving cells like keratocytes (151). Notably, both their leading edges and tails demonstrate strong force generation from traction force microscopy study and horizontal cantilever study, respectively (27,35,58,150). However, previous studies fail to provide for how a force at one adhesion evolves in relation to forces at other adhesions simultaneously. Furthermore, fibroblasts studied for traction forces have had a 2D morphology due to a flat substrate for their culture and assay where cytoskeletons are complicatedly structured (91), causing force at one focal adhesion to be a result of various tensions in many stress fibers linked to the adhesion. This configuration has made it difficult to make an appropriate comparison between forces at two adhesions. On the other hand, migration in 1D has been studied using micropatterned substrate, showing that 1D migration is rapid, uniaxial, independent of ECM ligand density, and dependent on myosin II contractility and microtubules which are similar to cell migration in 3D fibrils (152). Migrating fibroblasts on 1D fibrils also show a single lamella as well as a single tail (153) which allows for parity when understanding how these affect each other. However, the forces in this 1D migration remain unknown.

Here, we restrict 3T3 migration into one dimension by printing patterned lines of fibronectin on post arrays. We examine traction force generation of 1D cell migration with high time resolution, attempting to address how a change in force at the leading edge and tail affects changes in forces at other posts. Consistent with previous studies (35,98,150,154), we find that the most dynamic change in force is shown at both the leading edge and the tail. Interestingly, we show that the rise in force at the new adhesion caused decay in force at the adjacent adhesion, but it did not affect forces at the other posts. Moreover, force during adhesion release decreased and resembled viscoelastic relaxation while the cell membrane was still attached on the post at the tail. Interpretation of these findings on the basis of the multiphysics model suggests that a local activation signal that leads to myosin phosphorylation is responsible for the rise in force at a new adhesion, and low cell elasticity is responsible for the local exchange in forces between adjacent posts, but not others farther away. Together, we propose that a migrating cell

maintains a uniform tension across its whole body and is much softer than its surrounding environment.

4.2 Materials and Methods

4.2.1 Cell Culture

NIH 3T3 fibroblasts were obtained from C. Chen (UPenn) as a generous gift. This cell line was grown in DMEM (Lonza) plus 10% bovine serum (Gibco), 100 U ml^{-1} penicillin, 0.1 mg ml^{-1} streptomycin and 2 mM L-glutamine. Cells were incubated at 37 C/5% CO2. 2 x 10^4 cells in 0.1 mL media were seeded on microposts in one well of a 6-well-plate. To prevent further cell proliferation, 5 μg/ml of mitomycin-C (Sigma Aldrich) was added to the dish after seeding (155).

4.2.2 Live cell microscopy

Time-lapse image sequences were acquired by inverted bright-field microscopy (Ti-E, Nikon) equipped with an environmental control chamber with a heating unit (Nikon) and CO2 controller (In Vivo Scientific) using a 40x/1.4 NA Plan Apo phase objective lens (Nikon). Images were acquired at 5-second intervals. Images were captured using a high-resolution camera (Clara, Andor). Before taking bright-field time-lapse images, post bottoms were imaged by fluorescence illumination at 594 nm and used for the undeflected position of the posts.

4.2.3 Post arrays and micro-contact printing

Micropost arrays that were fabricated were 2.1 μm in diameter, 5.6 μm in height, and were 6 μm in post-to-post spacing, resulting in 38 nN/μm of post stiffness or 4 kPa of effective shear modulus considering Young's modulus of PDMS (Sylgard 184; Dow-Corning, Midland, MI) was 2.5 MPa (156). The arrays were printed with 50 μg/ml fibronectin (BD Bioscience) using a PDMS stamp that had patterns of arrays of lines with 6 μm widths and 12 μm edge-to-edge spacing so that cells could only migrate in one dimension on the arrays of posts. PDMS posts were stained with BSA conjugated with Alexa Fluor 594 for fluorescent visualization of post tops and bottoms. The deflection of the post (δ) was used

to report the local traction force (F) of a cell according to $F = k\delta = 3\pi r^4 E\delta/4h^3$ where k is a post's stiffness, r is its radius, h is its height, and E is the elastic modulus of PDMS.

4.2.4 Time-lapse Image Analysis

Bright-field time-lapse image sequences were analyzed using a custom-written Matlab program to obtain the centroids of the post tips. Migration velocities of cells on the posts and on the flat patterned surface were quantified based on the movement of the geometric centroid of the cell.

4.2.5 Mathematical Model

A multiphysics model was developed to predict the traction forces of a cell on posts during cell migration in aim 2 (157). Here, to better characterize features in live cell migration, we updated the model by adding viscoelasticity, a nonlinear Hill's muscle model, an activation signal by Rho GTPases pathways, and adhesion strength, different at each post, that enables the new adhesion at the leading edge and adhesion release at the tail when adhesion strength is weaker than the tension applied at the tail.

4.2.5.1 Viscoelasticity

A biological cell and its internal structure, such as its actin stress fibers, are viscoelastic in nature (147). Thus, we modeled a cell with standard linear solid model, or Zener model, wherein two springs and a dashpot are arranged both in series and parallel. On top of that, a myosin-based force generator was connected in parallel (Figure 24). In this configuration, actin-myosin is responsible for active tension generation, but, based on previous studies (158,159), the intermediate filaments and microtubules were assumed to be responsible for the passive elasticity which in our study we call cell elasticity. We assumed that the spring constants, or stiffness, of two springs in the model (k_{c1} and k_{c2}) are the same and its value (k_c) represents the cell elasticity.

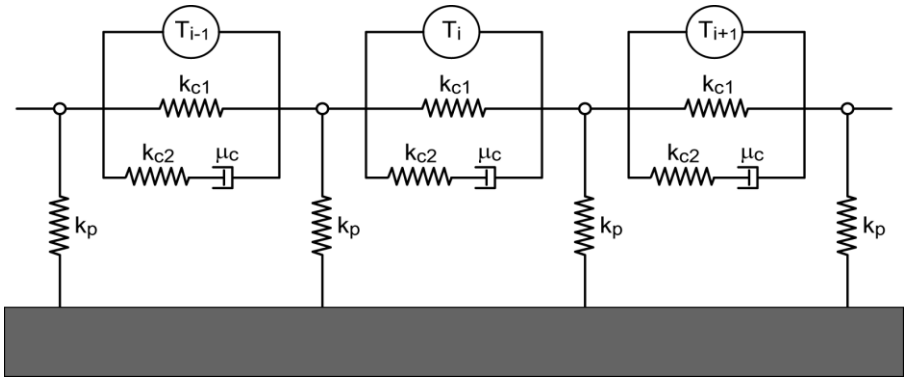

Figure 24. Viscoelastic cell model. The cell was modeled as a series of standard linear solid models with a tension generator in parallel, anchored on the posts with spring constant k_p. The springs k_{c1} and k_{c2} takes charge of instantaneous elastic response whereas the damper with damping coefficient μ_c provides drag forces that increase with shortening velocity.

4.2.5.2 Hill's Muscle Model

Instead of linearizing the originally nonlinear form of Hill's muscle model, we here use Hill's full non-linear force-velocity relationship in non-muscle myosin II. To guarantee the c1-continuity for the whole range of shortening velocities, especially around the isometric tension, the Hill model was combined with a Gompertz equation as follows:

$$\frac{T_i}{T_0} = \begin{cases} a\, e^{b\, e^{cv_i}} & \boldsymbol{v_i} > 0 \\ \frac{1-k_v v/v_0}{1+k_v v/v_0 k_m} & \boldsymbol{v_0} \le \boldsymbol{v_i} \le 0 \\ 0 & \boldsymbol{v_i} < \boldsymbol{v_0} \end{cases} \tag{4.2}$$

where T_0 is an isometric tension, v is a shortening velocity, v_{max} is a maximum shortening velocity, T_{max} is maximum tension, kv is a force constant that determines the sensitivity of tension against change in velocity, k_m is a muscle constant that affects the curvature of the force-velocity curve ($0.15<k_m<0.25$ for most muscle (125)) Gompertz constants $a = T_{max}, b = \log(\eta)\,, c = -\frac{kv\left(1+\frac{1}{k_m}\right)}{v_{max}\log(\eta)}$ were determined for the asymptote tension being T_{max} and ensuring c1-continuity at the point ($v=0, T=T_0$) as illustrated in Figure 25. This continuity around the isometric tension was proposed by Edman from experiment with frog muscle spindles (160).

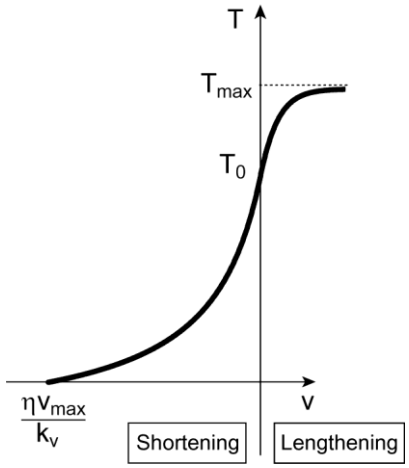

Figure 25. A plot of updated force-velocity relationship that maintains continuity around the isometric tension (T_0)

4.2.5.3 Assembly Level of Stress Fiber

Assembly level of stress fibers represents the level to which myosins are phosphorylated on a stress fiber. Its rate equation was used from the original model without changes (118,157) and is expressed by:

$$\frac{d\eta_i}{dt} = \left[k_f C_i(1-\eta_i)\right] - \left[k_b \eta_i \left(1 - \frac{T_i}{T_0}\right)\right] \quad (4.3)$$

where T_i is the local tension in the i-th fiber, T_0 is the isometric tension, and k_f and k_b are the forward and backward rate constants for assembly and disassembly of a stress fiber, respectively. The isometric tension T_0 is defined to be proportional to the assembly level of the stress fiber, $T_0 = \eta T_{\max}$, where $T_{\max}$ is the maximum isometric tension possible in a stress fiber.

4.2.5.4 Activation Signal

During focal adhesion formation, adhesion-generated signals regulate Rho GTPases which regulate several migration-related activities including actin polymerization and myosin-based contraction (161). Whereas Rac and Cdc42 regulate actin polymerization, Rho regulates myosin-based forces by activating Rho kinase which in turn phosphorylates the regulatory light chain of myosin II (5). Although actin polymerization is important for advancing the leading edge, as discussed in aim 2, its protrusive force has not effectively induced deflection of posts if tips of posts are flat in height (119). Thus, the activation

signal that contributes to the deflection of the new post at the leading edge was assumed to consist mostly of Rho. To be more physiologically similar to protein kinase signal transduction (162), the activation signal was updated to have a rising phase before it decays. The activation signal was expressed as:

$$C_i = A\, exp\left(\frac{-(t-t_0)}{\tau_1}\right)\left(1 - \frac{-(t-t_0)}{\tau_2}\right) \tag{4.4}$$

where τ_1 and τ_2 are time decaying constant, t_0 is the time when the signal starts to rise. A is a function of τ_1 and τ_2 with $A = \frac{1}{\left(\frac{\tau_1}{\tau_1+\tau_2}\right)\left(\frac{\tau_2}{\tau_1+\tau_2}\right)^{\tau_2/\tau_1}}$ so that the maximum amplitude of the activation signal is always one as illustrated in Figure 26. As previously assumed, a new activation signal was assumed to be triggered upon new adhesion formation. However, different from previous model (163), this signal was assumed to act locally on only the new stress fiber at the leading edge.

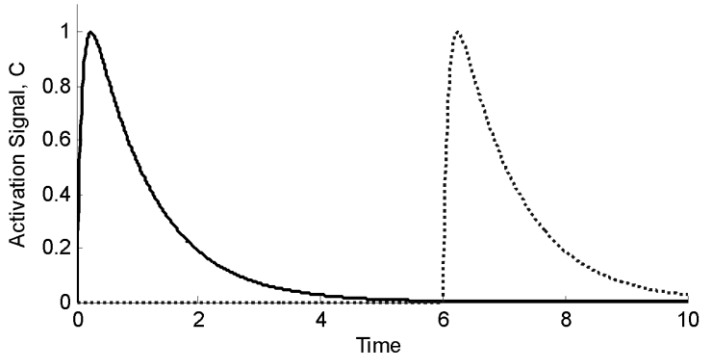

Figure 26. Activation signal as a function of time. Note that a new activation signal starts to rise as a cell forms a new adhesion. τ_1 = 0.8 and τ_2 = 0.8 are used for this example plot. The solid black curve represents a typical signal whereas the dotted curve represents a new activation signal due to the new adhesion at the leading edge.

4.2.5.5 Adhesion Dynamics

Adhesion strength correlates with the number of integrins and focal adhesion proteins linked to the actin cytoskeleton. It is expressed as a rate equation where adhesion growth is force-dependent upon ligation of an integrin to an ECM ligand while the adhesion at the tail disassembles with a constant rate as

$$\dot{S}_i = \begin{Bmatrix} -k_{sb} & i = n_{tail} \\ (1 - S_i)\frac{T_i}{T_0}k_{sf} & n_{tail} < i \leq n_{lead} \end{Bmatrix} \tag{4.5}$$

where k_{sf}, k_{sb} are forward and backward rate constants, respectively, S_i is the adhesion strength in i-th adhesion on post. Note that there are several assumptions made for the adhesion strength: 1) cell polarization is constant in one direction 2) No contraction until a receptor (integrin) is bound to the ligand (ECM) 3) Linkage between integrin and ECM is determined stochastically with a random function of a certain probability 4) Adhesion breaks when the tension at the tail exceeds the adhesion strength ($T_{tail} > S_{tail}$).

4.2.5.6 Model Calibration

Constants in the model were calibrated based on contraction of quiescent (non-migrating) 3T3 fibroblasts on lines of posts so that strain energy of the cell could match with the strain energy of the simulated model cell (Table 14, Figure 27). A cell contracting on 1D posts (Figure 27 A) showed fluctuation of individual forces through time especially at its edges (Figure 27 B). We found that the strain energy also fluctuated through time in the range between 6 fJ and 13 fJ with an average of 8.5 fJ (Figure 27 C). A sensitivity analysis was performed to study the effect of forward and backward rate constants, k_f and k_b, respectively on the strain energy. To do that, the model was simulated for its contraction phase until it approached the steady state through time (Figure 27 D). We used a practical criterion to identify "steady states" as states within 99% of the asymptotes they were approaching. Strain energy at the steady state (after 4 min in Figure 27 E) was taken as an output for the sensitivity analysis. 3D space of the strain energy as a function of k_f and k_b showed that the steady-state strain energy increased with an increasing k_f with more sensitivity than when an increasing k_b caused a decrease in strain energy (Figure 27 F). We chose values of the rate constants as well as other constants so that they could make the steady-state strain energy to be a range around the mean strain energy of a living cell (Table 14).

Table 14. Model Constants used for simulations unless otherwise specified.

Parameters	Description	Values	References
k_v	Force reduction coefficient with respect to strain rate	0.1	
v_{max}	Maximum shortening velocity	0.3 μm/min	(118)
T_{max}	Maximum tension of a cell	20 nN	Maximum force of a contracting cell
k_m	Hill muscle constant	0.25	
k_f	Assembly rate constant	3 min^{-1}	-
k_b	Disassembly rate constant	2 min^{-1}	-
k_{sf}	Assembly rate for adhesion dynamics	0.01 min^{-1}	-
k_{sb}	Disassembly rate for adhesion dynamics	0.001 min^{-1}	-
k_{c1}	Elasticity of a cell (Spring parallel to the Maxwell spring-dashpot)	0.1 nN/μm	
k_{c2}	Elasticity of a cell (Spring in Maxwell component (series with dashpot))	0.1 nN/μm	
μc	Viscosity of a cell	2 nN s/μm	
k_s	Spring constant of posts	38 nN/μm	Same as experiment
τ_1	Time decay constant 1	0.8 min	
τ_2	Time decay constant 2	0.8 min	

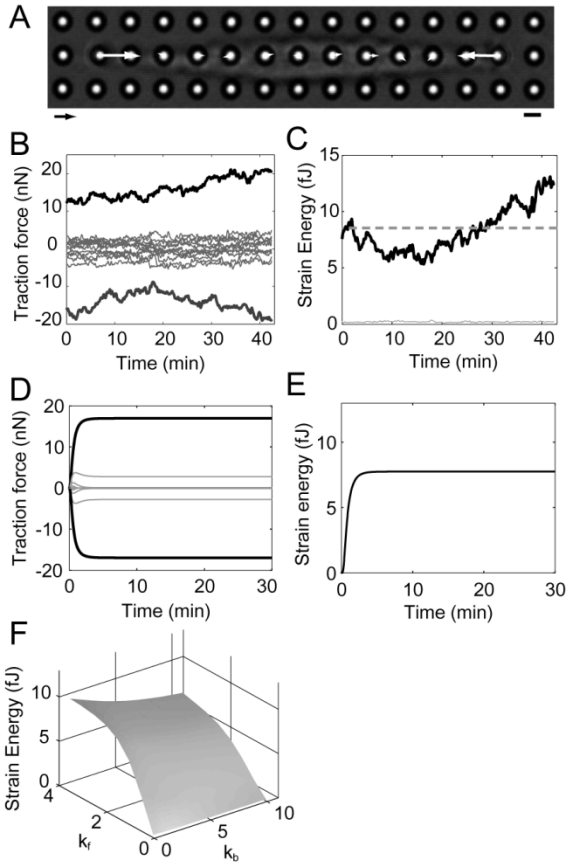

Figure 27. Model calibration was done based on traction forces of a non-migrating cell contracting on posts. (A) Bright-field image showing a cell on 13 posts with force vectors at t = 42 min. Arrow scale: 10 nN, bar scale: 3 μm. (B) Plot of traction forces with time showing that forces at either ends (black) are much larger than forces in the middle (gray) (C) Strain energy as a function of time. Gray dashed line represents the mean strain energy at 8.5 fJ. (D) An example simulation of traction forces from an initial condition of zero tension. Note that forces reach the steady-state after 4 min. kf and kb were 3 and 2, respectively. Other constants were based on Table 14. (E) Strain energy of the model reached a steady state of 7.8 fJ. (F) Sensitivity 3D space of steady-state strain energy with a function of k_f and k_b, showing that strain energy is more sensitive to k_f than to k_b.

4.3 Results

4.3.1 Large Forces at Leading Edges and Cell Tail Compared to Forces in Cell Middle

To investigate traction forces of 1D cell migration, we printed a line pattern of fibronectin on tips of micropost arrays and measured forces at all posts underneath the cell with high-resolution time-lapse microscopy (Figure 28). Within 4 hr after seeding, cells on posts began spreading onto 10-20 posts which continued over the next several hours. After ~8 hr, cells developed a polarized morphology along the line pattern with indicative features of migrating cells such as the narrow lammellipodial protrusion and tail formation, and began to migrate on posts by releasing a post at its tail as well as adhering to a new post at its leading edge. After ~30 hrs, cells became quiescent and lost their polarized morphology, resulting in no further motility. To capture the dynamic signature of migrating cells on posts, we chose to conduct all traction force experiments 8 hr to 20 hr after seeding. Cells in this time range crawled on posts at 10.3 (± 2.0) μm/hr and with an average length of 71 (± 6.3) μm (Table 15), which is in the range that is similar to those of cells migrating on line patterns on flat PDMS surface (9.7 (± 1.8) μm/hr in velocity and 95.1 (± 4.1) μm in length).

Importantly, as a fibroblast migrates on posts, we found large forces at the leading edge and the tail whereas posts in the interior region of a cell showed very low forces for most of time during migration (Figure 28 B and C). However, the temporal response of forces was not static but dynamic (Figure 28 C): upon membrane adhesion, the force at the new post rose up to the peak of 10-20 nN in around 5-10 min, which was followed by a dynamic decay to near zero although its duration varied with each adhesion (Figure 28 C, top). We call this contraction at the leading edge as “leading edge contraction” for later use. We also found that the force after the peak decays almost to zero as the force at the new adhesion rose to its peak. Force at the tail was also dynamically changing until it was released. At the period of adhesion release, the force started to decrease before the membrane detached (shown as an inverted filled triangle in Figure 28 C, bottom).

Furthermore, it is noteworthy that the forces on posts in the interior region of migrating cells were mostly near zero with a range of ±2 nN (Figure 28 C middle). We also quantified strain energy of all posts as a mean of measuring total contractile work done by a cell on posts. We found that strain energy fluctuated with time, but the amount of the fluctuation was not synchronized with events of new adhesions or tail release; the change in strain energy during these events was not significantly larger than the overall fluctuation of the strain energy throughout the time (Figure 28 D).

Table 15. Velocity and length of migrating cells on 1D posts

	Distance (μm)	Time (min)	Velocity (μm/hr)
Cell 1	12	27	26.7
Cell 2	12	100	7.2
Cell 3	6	240	1.5
Cell 4	6	193	1.9
Cell 5	18	79	13.7
Cell 6	12	120	6.0
Cell 7	36	176	12.3
Cell 8	18	85	12.7
Cell 9	9	108	5.0
Cell 10	21	67	18.8
Cell 11	24	113	12.7
Cell 12	6	64	5.6
Average	15	114	10.3
Standard deviation	2.5	16.8	2.0

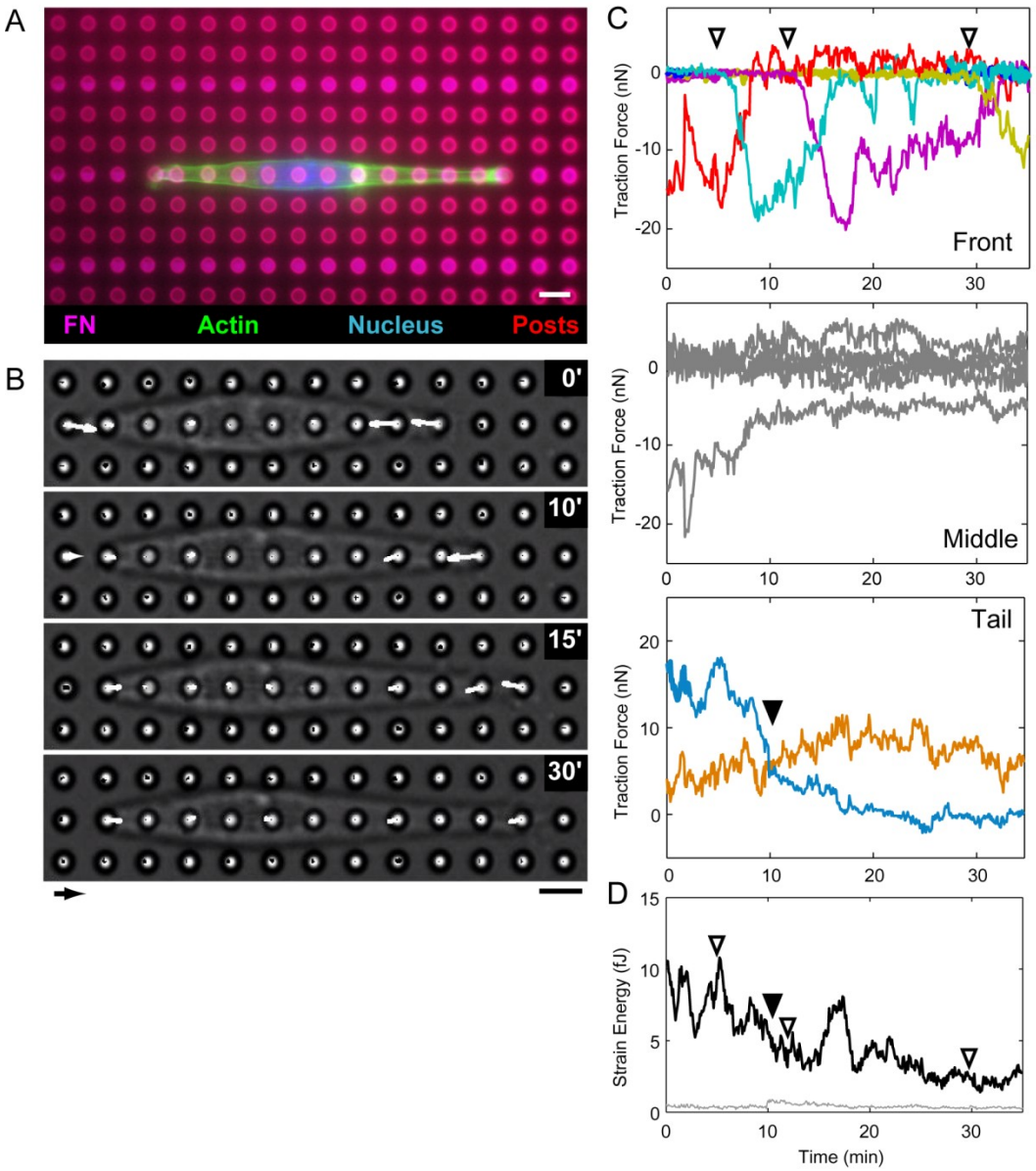

Figure 28. Fibroblast on line-patterned posts migrated with dynamic force generation. (A) Fluorescent image of a representative 3T3 cell stained with actin and nucleus on posts (red) showing 1D line pattern of fibronectin (purple). scale bar: 6 μm (B) Bright field time-lapse images of a cell migrating directionally from left to right. Note that the cell show large forces at its leading edge and at the tail throughout the migration. Arrow scale: 10 nN, bar scale: 6 μm (C) Traces of traction forces at each post underneath the cell in B over time. (Top) Forces at the front of the cell rose with the adhesion (open triangles) and decayed out as the force at the new post increased. (Middle) Most of forces at the middle stayed at around zero with a ±5 nN range. (Bottom) Force at the tail (blue, first post in the second row on array shown in B) decreased to zero while the force at the adjacent post (dark yellow, second post in B) slowly increased. Note that the force at the tail decreased slightly further after the visible membrane attachment is removed (filled arrow). (D) Strain energy as a function of time. Note that three adhesions and one release did not change the strain energy compared to overall fluctuation of the profile.

4.3.2 Low Forces in the Interior Region Suggests Low Cell Elasticity and Uniform Tension across the Cell

Migrating cells showed large forces only at the edges and very small forces in their interior region. To comprehend these contractile forces, we adopted a bio-chemo-mechanical contractility model (1) and tested the traction force distribution of cells in response to varying force constant k_v during their early contractile phase in which all stress fibers are stimulated with an activation signal (Figure 29 *top row*). This dimensionless constant k_v affects the slope of force with respect to the shortening velocity so that decreasing k_v, in the force-velocity relationship, makes the tension to be always near the value of isometric tension in a certain range of shortening velocity. Since shortening velocity merely affects the determination of tension in any stress fibers, decreasing k_v eventually leads to almost uniform tension for all stress fibers in a whole cell. Our simulation showed that only low k_v can simulate the very low forces in the interior and large forces at both edges whereas large k_v leads to still significant forces in the cell interior. This result implies that a migrating cell maintains a uniform tension throughout its body because the low force constant k_v causes the tension to be always around the magnitude of the isometric tension. Furthermore, even if the force constant is low, we found from the model simulation that cell elasticity, which is modeled as the stiffness of one of the springs in our Zener model, should be much smaller than the post stiffness in order for the cell to show low forces in the middle (Figure 29 *bottom row*).

4.3.3 Rapid Rise in Force at a New Adhesion Affects Forces at the Adjacent Post without Affecting Other Posts

At the leading edge of a migrating cell, force began to develop about 20 sec after the membrane was observed to attach to the new post (Figure 30 A). The force at the new post rose monotonically until it reached a peak at around 5-10 min (Figure 30 B). Interestingly, as the force rose at the new post, the force at the previously leading edge decreased (Figure 30 C). This trend occurred throughout 24 events and 12 cells although the time for the force to reach its peak, the force magnitude at the peak, and the time evolution of the force at the adjacent post varied per each event of leading edge contractions (Figure 31). Quantification of change in the forces at other posts during the time when the force at the

new post reached its peak showed that the changes in force in the middle or at the tail were significantly smaller than the change in force at the adjacent post (Figure 30 D).

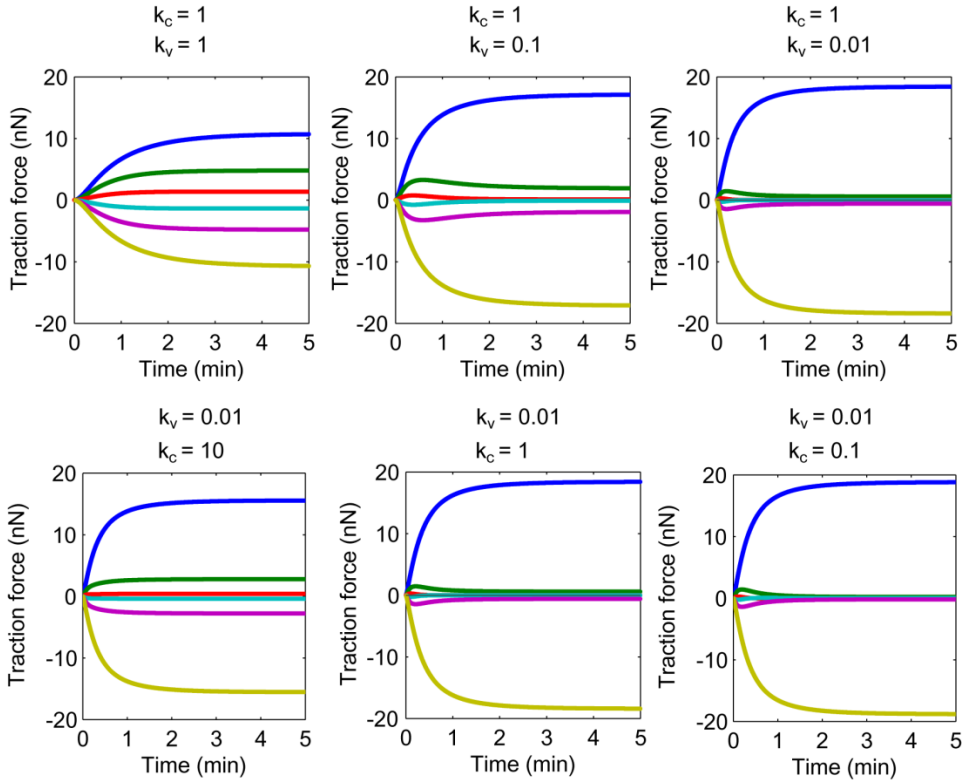

Figure 29. Low force constant and low cell elasticity simulates low forces in the middle posts. Traction forces during the first 5 minutes of contraction phase with k_v = 1, 0.1, and 0.01 (*left to right, top row*), and k_c = 10, 1, 0.1 nN/um (*left to right, bottom row*).

4.3.4 Forces during Leading Edge Contraction Suggests Low Cell Elasticity

During contraction at the leading edge, the change in force at the adjacent post was significantly larger than changes in force at the posts that were not adjacent. To demonstrate this result, we investigated an effect of cell elasticity on changes in forces of individual cells during leading edge contraction by using values of 10, 1, and 0.1 nN/μm of cell elasticity in the model (Figure 32). We chose this range of values by the assumption that the elasticity of a living mesenchymal cell is smaller than the elasticity (38 nN/μm) of the substrate (164). The simulation showed that, if a cell had larger elasticity than the elasticity of the substrate, the force at the new leading edge affected not only force at the adjacent post, but also forces in the middle posts (Figure 32 A). When the cell elasticity was smaller than the elasticity of the substrate, however, no posts in the middle or at the

tail except the adjacent post were affected by the force at the new post (Figure 32 B and C), suggesting that the elasticity of a fibroblast that protrudes and contracts its leading edge might be much lower than the elasticity of the substrate.

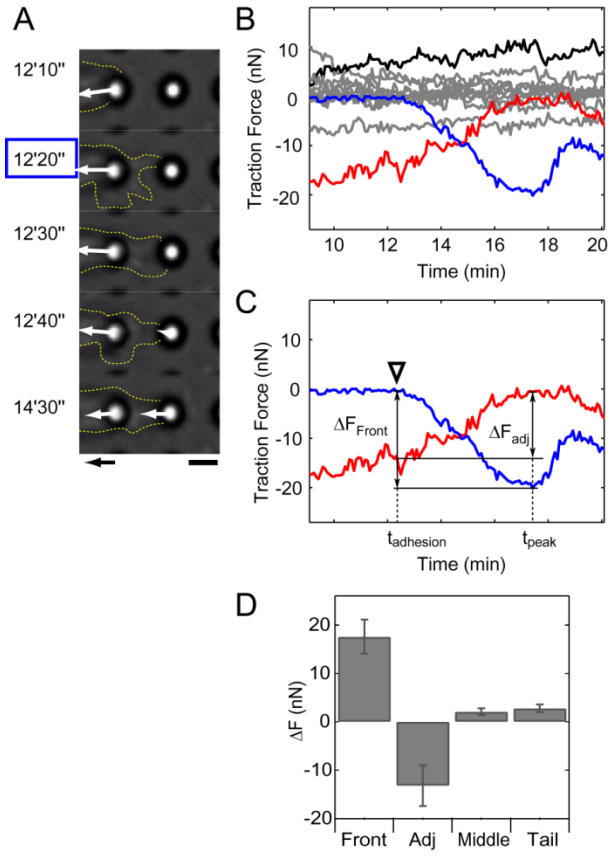

Figure 30. Rise in force at the leading edge caused the force at the adjacent post to decrease. (A) Phase time-lapse images showing cell membrane (yellow dotted line) attachment and force development at the new post. Note that force started to develop 20 seconds after membrane attachment. Arrow scale: 10 nN, Bar scale: 3 μm. (B) Traction forces of all posts under a cell during the contraction at the new post (blue). A force profile at the adjacent, middle and tail are shown in red, gray and black, respectively. (C) Change in force at each post was quantified based on two time points, t_a and t_p. t_a represents the time when the membrane first attaches to a post and t_p represents the time when the force at the new post reaches its peak value. (D) Change in force at a cell's front, adjacent, middle, and tail. Data are collected from 24 events and 12 cells. Note that the force at the adjacent post changed significantly larger than those at the middle or tail.

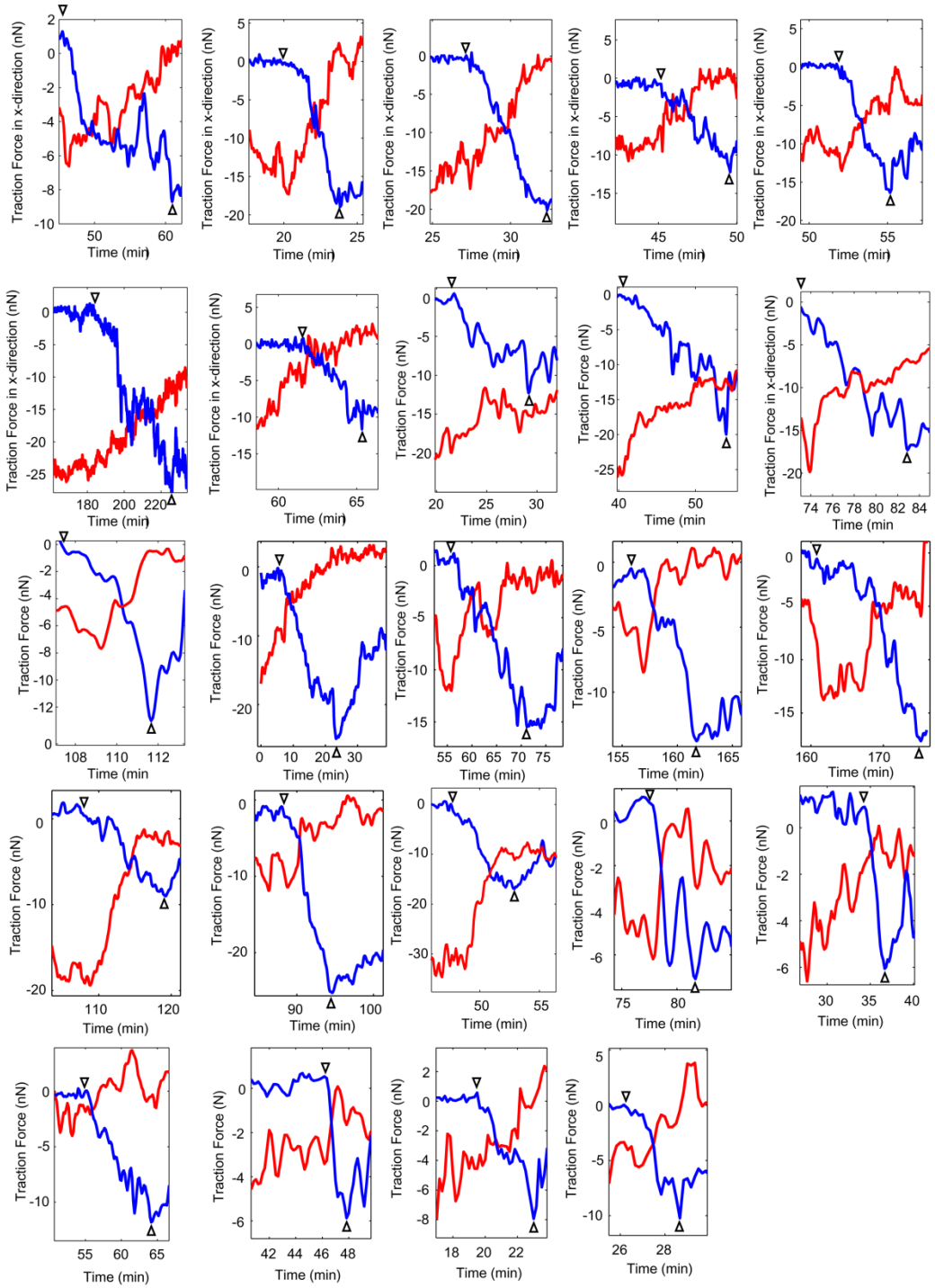

Figure 31. Traction forces during leading edge contraction. Forces at the new post (blue) and the adjacent post (red) for all 24 events and 12 cells are shown. The time of membrane attachment onto a new post (t_a) and the time that a force at the new post reached its peak (t_p) were marked with an inverted triangle (**∇**) and upright triangle (**Δ**), respectively.

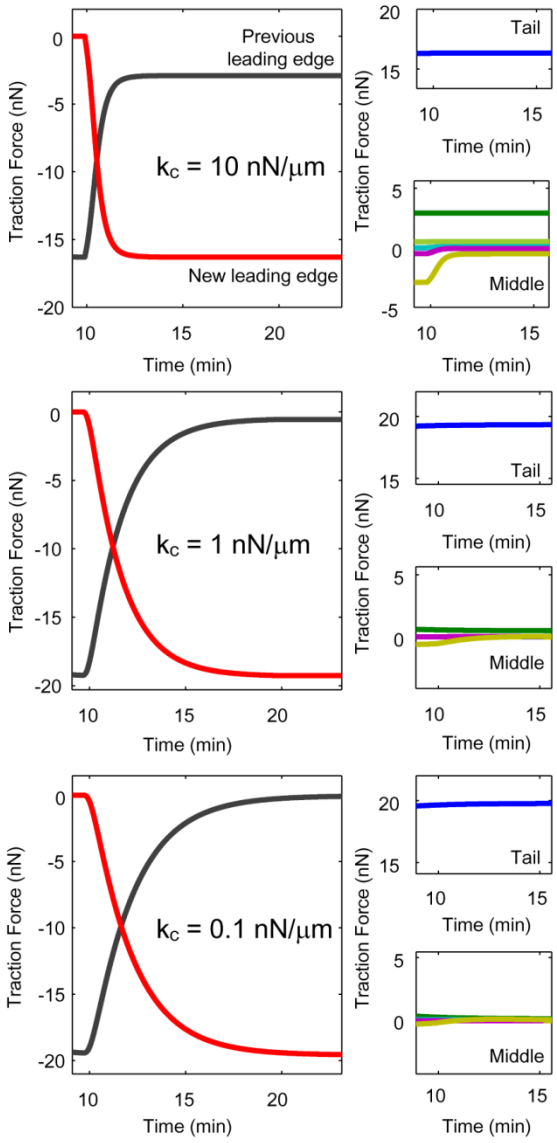

Figure 32. Effect of cell elasticity on the two posts at the leading edge and other posts. during leading edge contraction Note that there is a change in deflections at the posts in the middle when cell elasticity is large (10 nN/um)

4.3.5 Instantaneous Release of a Post Causes Instantaneous Rise in Force at the Adjacent Post

To investigate the traction force of the post at the tail, we measured the force profile with time at the tail while examining the membrane activity during the adhesion release. Interestingly, for most cells, a substantial amount of force was removed before the visible cell membrane detached from the post (Figure 33 A). The time taken for the force at the tail to decrease until the visible cell membrane is removed from a post was around 20 ± 12

sec. This observation implies that when a cell releases its tail, the cytoskeletal tension might be removed prior to the removal of actual cytoskeletal elements from the post.

To study whether the force at the tail affects forces at other posts, we quantified the change in forces for the post at the tail, adjacent to the tail, and other posts (Figure 33 B) during the tail release (Figure 34). We defined the time period of tail release to be the time from when the post at the tail showed the local peak force before it continuously dropped to zero (t_{br} in Figure 33 C), to the time of complete membrane removal from the post (t_{ar} in Figure 33 A and C). Interestingly, the drop in force at the tail caused an increase in force at the adjacent post (Figure 33 B and C). However, the changes in forces in the middle or at the leading edge were significantly smaller than those at the adjacent post (Figure 33 D, $p < 0.01$).

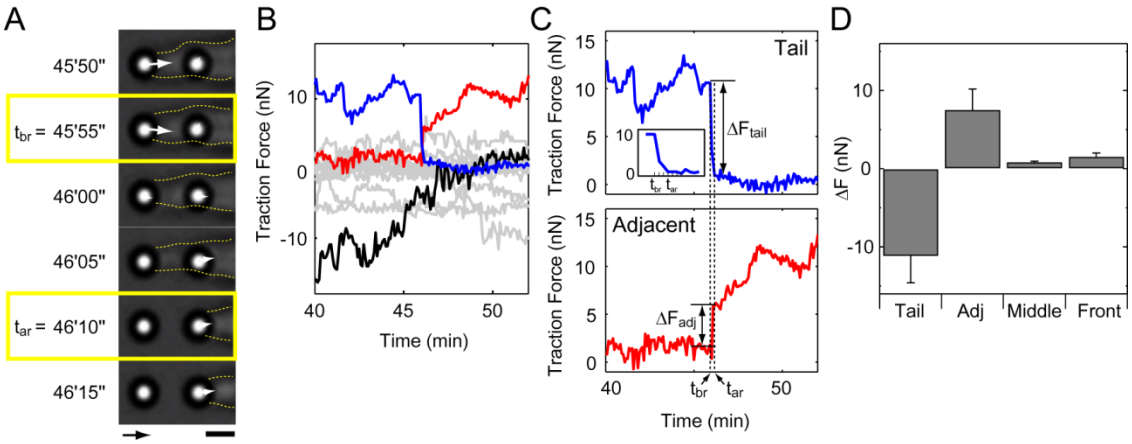

Figure 33. Drop in force at the tailcauses a rise in force at the adjacent post but has no effects on other posts. (A) Time-lapse phase contrast images showing a tail-release event on posts. Note that the visual cell membrane remained attached (46'00" and 46'05") after significant force (at 45'55") was removed. (B) Plot of traction forces at the tail (blue), the post adjacent to the tail (red), middle (gray) and leading edge (black) over time during tail release. (C) Plot of individual force at the tail (top) and at the adjacent post (bottom) with showing ΔF measurement. Force change was measured in reference to the two time points: t_{br} and t_{ar}.where t_{br} is the time after which force constantly drops to zero and t_{ar} is the time when the visible cell membrane is completely removed around the post. Arrow scale: 10 nN, Bar scale: 3 µm

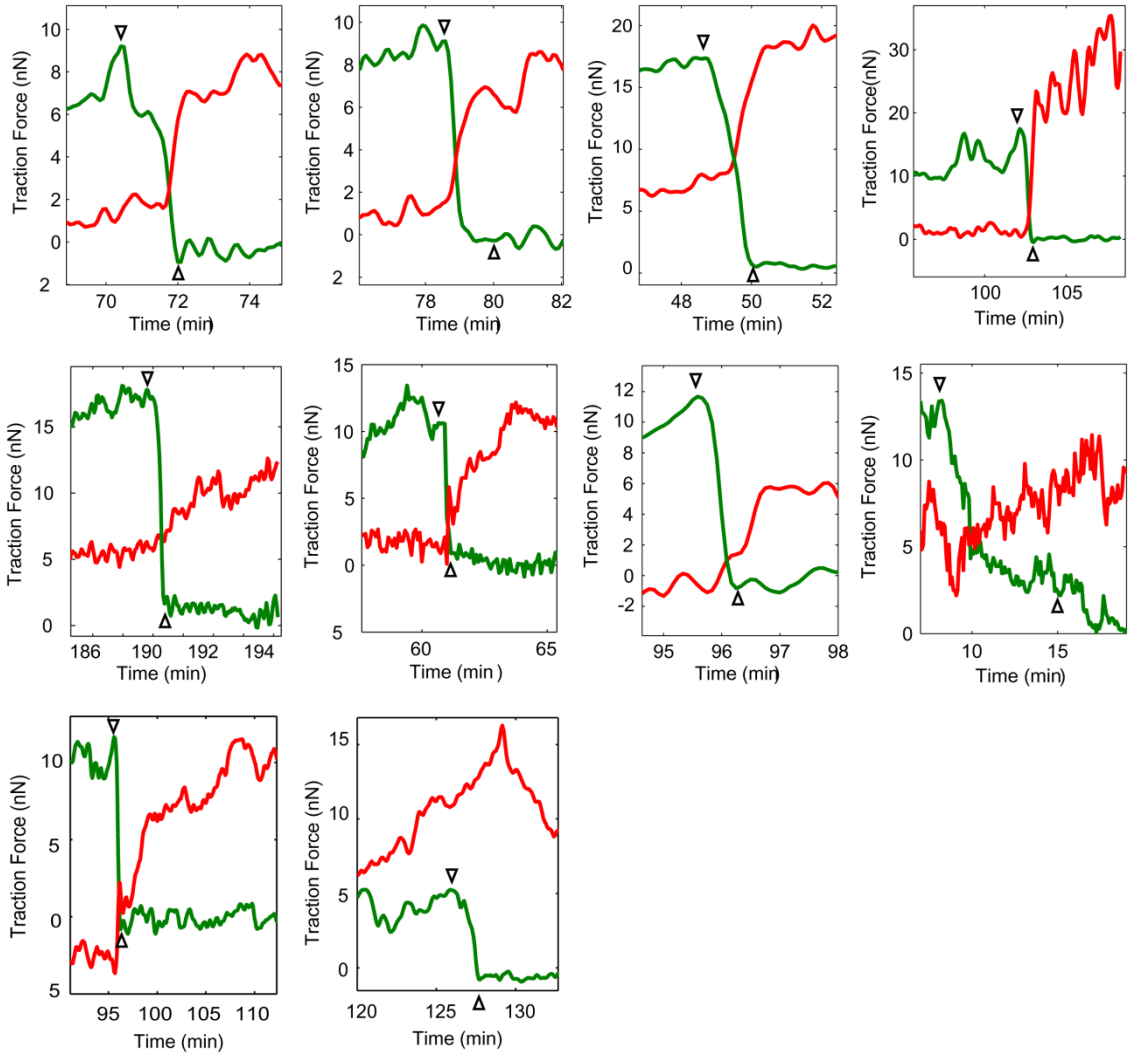

Figure 34. Traction forces during tail releases for all cases. Forces at the tail (green) and the adjacent (red).for 10 events and 8 cells are shown. The time that a force at the tail reached its peak before adhesion release (t_{br}) and the time of membrane detachment from the post (t_{ar}) were marked with an inverted triangle (**∇**) and upright triangle (**Δ**), respectively.

4.3.6 Forces during Tail Release Also Suggest Uniform Cytoskeletal Tension and Cell Elasticity Lower Than Substrate Elasticity

The decrease in force at the tail coincided with an increase in force at the adjacent post, but posts in the middle or front had no significant changes in force. To predict this finding, we simulated the model in which it releases the post at the tail. In the model, it was assumed that a cell begins to release an adhesion at the tail when the tension at the adhesion exceeds the adhesion strength. During the process of releasing, the stress fiber linked to the adhesion at the tail was assumed to disassemble its level of assembly in a rate a hundred

times (200 s^{-1}) larger than a normal backward rate constant (k_b = 2 s^{-1}), causing the tension in the fiber to decrease to zero in a short time. As the tension dropped in the stress fiber, the force at the tail also decreased in a manner that is similar to a viscoelastic relaxation (Figure 35 *left column*).

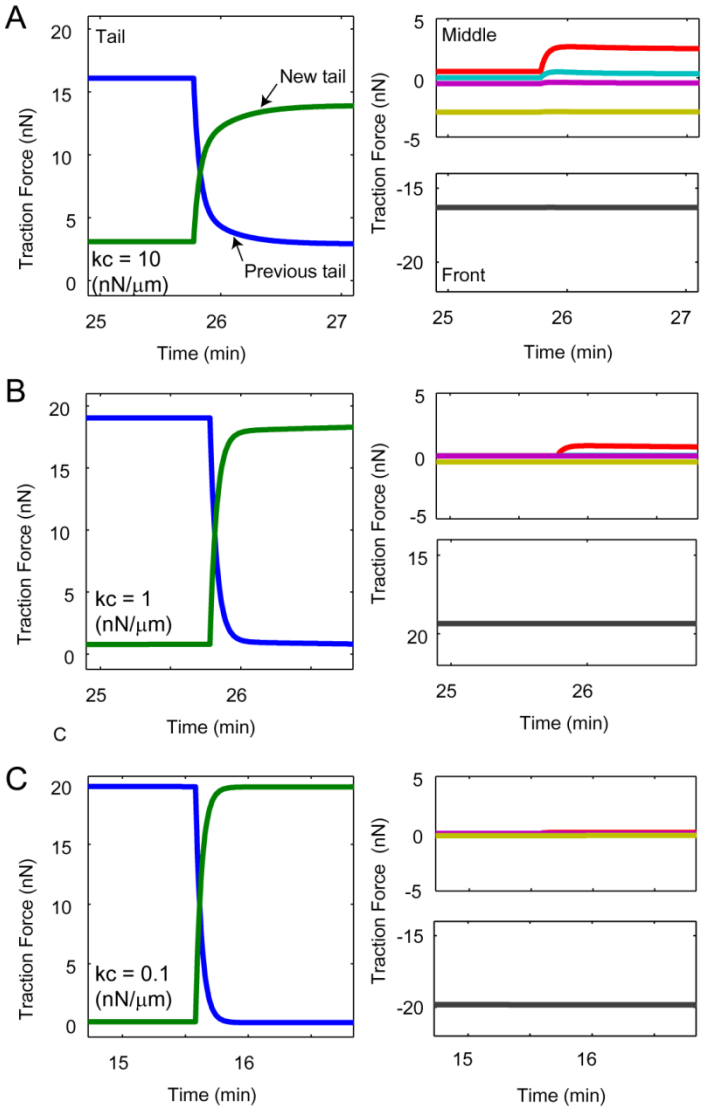

Figure 35. Viscoelastic change in forces during tail release. mu and kv were maintained to be 2 nN s/um and 0.01.

As in the case of simulations of leading edge contraction, the effect of cell stiffness (10, 1 and 0.1 nN/μm) on traction forces of all posts under a cell during the tail release was tested. A drop in force at the tail caused an increase in force at the adjacent post for all three cases of cell elasticity, but it also changed some of the middle posts when the cell had

a large stiffness (Figure 35 A). When the cell had a moderate or low elasticity, however, the change in force at the tail merely affected the change in force at other posts (Figure 35 B and C), suggesting that a cell that releases its tail might have a cell elasticity lower than the elasticity of a substrate.

4.4 Discussion

How a cell employs forces to migrate is an important fundamental question for understanding cell motility. Previous studies using traction force microscopy typically showed large forces at the leading edge and weak forces in the middle and tail at a few discrete time points during migration, proposing a frontal-towing model (35,37,150). In the study using MEMS-based horizontal cantilever, however, forces at the tail of a cell showed the largest force whereas forces at the leading edge were lower than forces at the tail (58). Our data show that both leading edge and tail exhibit large forces compared to forces in the middle, but their temporal profiles are not steady, but dynamically changing. Based on our finding, we speculate the reason why force at the tail was measured to be low in traction force microscopy study is that forces were measured not exactly from the end point of the tail, but from some points between the tail and cell center (150). Our results show that force at the middle is low compared to the force at the end of the tail. Furthermore, the reason why a force at the leading edge was measured to be low can be from a cell's morphology where in their 2D structure, lammellipodial region spread out broadly, so only a portion of forces in the lammellipodial region might have been measured by the cantilever (58).

The multiphysics model which we have presented suggests that a migrating 3T3 fibroblast should have an elasticity much lower than that of the micropost and maintain uniform tension throughout the cell in order to show these experimental findings: 1) very low forces in the cell interior compared to leading edge or tail, 2) no effect of increase in force at the leading edge on the forces in the middle or tail regions and 3) no effect of reduction in force at the tail during tail release on forces in middle or front region. Previously, elasticity of 3T3 fibroblasts has been studied using atomic force microscopy (AFM), showing adaptation of cell elasticity to the substrate elasticity (148). However, in this

study, the cell stiffness was measured from the fixed cells whose mechanical properties are significantly different from those of living cells (165). Elasticity of living, Dictyostelium discoideum was studied using AFM, showing the elasticity of migrating cells (10 kPa) was much smaller than that of underlying agarose film (150 kPa) (166). Using microspheres injected into cytoplasm, Kole *et al.* showed that the elasticity of migrating 3T3 fibroblasts was very soft (2 – 33 Pa) compared to substrate stiffness (~3 GPa) (164).

Model-based interpretation of the live cell migration also suggests that a migrating cell maintains uniform tension throughout the cell. Consequently, this also means that tension in the migrating cell does not follow, or is very insensitive to, Hill's muscle model where a tension decreases with increasing shortening velocity. Rather, small forces in the cell interior suggest that stress fibers which connect adhesions on all posts try to maintain the same level of tension although this tension could vary with time simultaneously in all stress fibers. If cytoskeletal tension is sensitive to a shortening velocity of its stress fibers, it would create a gradient in tension throughout the cell where there is less tension in a stress fiber at the boundary than in the cell interior which would result in the significant amount of forces even in cell interior. Similarly, if the tension at the leading edge is sensitive to its shortening velocity, it would make the tension in the leading edge less than the tension in the middle because the non-zero shortening velocity at the leading edge would create a tension of which magnitude is less than the magnitude of isometric tension. However, our results with migrating fibroblasts do not show these force read-outs, suggesting that Hill model might not be appropriate for migrating cells. There is a study which has shown that force and shortening velocity of contraction of single myoblasts measured using the two parallel microscale plates follows a trend of Hill's muscle model (79). The original bio-chemo-mechanical model also has recapitulated the contraction of smooth muscle cells on micropost arrays (94,118). Thus, our experimental results and model simulations suggest that once fibroblasts are polarized and actively migrating, they develop forces in a velocity-independent manner.

One of the major experimental findings different from our model simulation is that, in the experiment, force at the leading edge started to decay after it reached a peak, whereas in the simulation, the force at the leading edge rose and stayed at its isometric force (Figures

30 and 32). The experimental finding suggests that the leading edge of a migrating cell might not have a steady-state tension. In the model, the isometric tension developed in the stress fiber prevents the stress fiber assembly from disassembling by forcing the backward term in the assembly level rate equation to zero. It follows that this leads to steady-state assembly level as well as cytoskeletal tension after the forward term triggered by the activation signal goes to zero. In order for the model to have a decaying trend after the peak, the backward term in the assembly level rate equation should not completely decay to zero even when the tension becomes isometric tension which implies that isometric tension might not be enough to completely prevent the stress fiber from disassembly. This idea suggests that the acto-myosin association is not just a catch-bond, but a two-state catch bond (167), where the life-time of an actin-myosin bond may slightly decrease when it is under isometric tension.

An important question about the tail release is how much cytoskeletal tension contributes to the detachment of an adhesion at the tail. In our experiments on fibroblasts, a significant reduction in force started to occur after the force at the tail had a local maximum at around 10 nN or above. For about 20 sec afterward, the force fell to, and remained at zero. Then the cell membrane completely detached from the post. Interestingly, in most of the tail releasing events, the force at the tail slightly increased about 1 min before the force drop, suggesting that there may be an increased activity of myosin phosphorylation when focal adhesion turn-over start to occur. Reduction in integrin-cytoskeletal linkages and an increase in myosin activity might be compatible because focal adhesion disassembly can activate the activity of focal adhesion kinase (FAK) (72,139) which is a signaling protein that has a role in weakening cytoskeleton–integrin linkages under force (168-170). Thus, it is likely that both traction forces and rapid adhesion turn-over contribute to the release of the cell tail.

During the rapid drop in force at the tail, the cell membrane remained attached and the force profile showed a viscoelastic relaxation behavior (Figure 33 C *inset*). When a stress fiber is cut by laser-snipping, the profile of the end points of the stress fiber has shown viscoelastic relaxation behavior (171). Among three types of cytoskeletal filaments, actin fibers have been shown to be responsible for viscoelastic response of cells when studied

using AFM (147). Thus, with rapid disassembly of the focal adhesion, viscoelastic relaxation of the force at the released post might be from the viscoelasticity of the stress fibers.

Another important question is how migration affects the total contractility of a cell which can be quantified by strain energy stored in posts under a cell. Previously, Del Alamo et al. observed from dictyostelium cells that the total strain energy of the cell increased with new adhesion and decreased with release (132). This finding is different from our results where 3T3 maintains a similar level of the strain energy during both leading edge contraction and tail release (Figure 28 D). We speculate that, during the leading edge contraction, the force at the new adhesion develops to a level similar to the level that the previous leading edge (adjacent post) has had. Similarly, during the tail release, the increase in force at the new tail (adjacent post) recovers the force lost from the old tail. Different biomechanical properties of different cell types (Dictyostelium discoideum vs. human mesenchymal cells) might be a possible source of inconsistency between our finding and the previous study.

Cell migration on micropost arrays has been studied for different cell types (154) and collective cell migration (57). Reducing the dimension of cell migration and matching it with a multiphysics model simulation have led to a finding of spatiotemporal relationships among the forces at each adhesion of single fibroblasts and biomechanical properties inferred by the model. Unraveling the hypothesis underlying the model-based discoveries will depend on the experiments of spatiotemporal visualization for structures of cytoskeletons and focal adhesions, and also for the signaling activities of Rho GTPases. The prediction via an appropriate multiphysics model will reveal certain aspects difficult to observe experimentally. Tailoring the model with further experiments might achieve the goal of expanding it into physiologically relevant in-vivo situation, e.g. collective cell migration within a 3D gel, or stem cell migration from a tissue scaffold into a damaged tissue.

5. Overall Conclusions and Future Directions

5.1 Specific Aims

The work in this dissertation is focused on contractile forces of both migrating and stationary cells. We use a combination of experimental and computational techniques to test hypotheses related to the relationship between contractility and mechanical properties of a cell and a substrate, focal adhesion strength, and spatiotemporal response of cell contractility during cell migration. We further test hypotheses about the dynamics of contractile forces at cell edges and their effects on other posts during cell migration.

In the experimental study in Aim 1, the substrate stiffness alone could affect the average contractile forces without a need to affect spreading of cells. The cell spread area, on the other hand, decreased the average contractile forces: individual cell forces were distributed non-uniformly under the cell: there were small forces on cell interior and large forces on cell periphery. Use of post arrays with different spacing showed that a cell's contractility responds more sensitively to the number of adhesions rather than the cell area. Interestingly, focal adhesion size of cells followed the same trend that the force data showed, suggesting that focal adhesion size and the local forces are closely correlated, almost mirroring each other. Both the cell area and the substrate stiffness are critical in that they can affect stem cell differentiation with Rho-mediated fashion (41,76). Understanding the role of each mechanical factor is the important step in designing biocompatible tissue construct for tissue repair.

In computational study in Aim 2, we observed forces at cell tail and leading edge of migrating cells are larger than force in the middle. Upon a migration cycle, in both 1D and 2D, strain energy exerted by a cell dropped from the level at the previous contraction phase, suggesting that cells lose their contractile energy as they step further forward. This computational prediction is beneficial since it is impossible to do the experiment where we can set a time for a cell to extend or release. Not only in the environment of post arrays, the model can be readily adapted to the different mechanical set-up.

In Aim 3, we updated the model by adding viscoelasticity and adhesion dynamics, and used it to interpret the temporal changes in forces of 1D fibroblast migration. From the force profile at the leading edge, tail and interior region of a cell, we found the change in force at leading edge or tail affects only an adjacent post, but not others. To simulate this contractile behavior, the multiphysics model suggests that a cell maintains its tension uniformly across the cell and its elasticity to be much lower than a substrate.

5.2 Future Recommendations

This work demonstrated the contractile force generation of cells in a variety of mechanical environments during migration or contraction. In this section, recommendations will be made for extension of aims that have been presented in this dissertation.

5.2.1 Finding Appropriate Force Metric for Mechanotransduction

Our studies find different role of substrate stiffness, cell spread area and micropost density on the traction force. We have used total force, average force and strain energy as a force metric to quantify contractility of a cell. However, it can be helpful to find the most effective metric that affect, via mechanotransduction, important cell functions such as proliferation, cell differentiation or cancer progression which are mediated by Rho GTPases –based contractility (41,42,76,172,173). Substrate stiffness, for example, is shown to induce increased Rho activation which leads to increased proliferation and diminished differentiation (170,171) whereas increased cell area causes increased cell proliferation and osteogenetic differentiation via RhoA-mediated contractility (74,76). Hence it would be useful to perform contractility studies of mesenchymal stem cells with quantifying Rho activation using FRET biosensor (174) to find which force metric is correlated with Rho activation and stem cell differentiation. Based on our finding in Aim 1, we speculate that the average force might best represent Rho activation because it has a positive relationship with stiffness and an inverse-like relationship with spread area.

5.2.2 Comparison of Force Measurement Techniques

As described in Chapter 1, several force-measuring tools have been developed to study traction forces. Traction force microscopy (TFM) and micropost arrays are the two most

widely-used force assays at present. Although they have been designed to measure the same traction forces, they have distinctive characteristic which is a continuous versus discrete contact surface. Thus, it would be helpful to compare the spatiotemporal force results from both substrates. While the polyacrylamide gel has a disadvantage of the inaccuracy in finding exact source of the force application, it has also advantage of allowing better visualization of focal adhesions and biochemical signaling due to its continuous nature. For example, high refractive index silicone gel was recently applied to enable both total internal reflection fluorescence and traction force microscopy (175). In Aim 3, we had a component of adhesion strength, but were not able to test if adhesion grows or decays as we predicted due to the distance between the objective and the post tips. Thus we expect TFM might be able to elucidate the focal adhesion dynamics during cell migration. A side-by-side comparison could highlight the relative strengths and weakness of each force assay.

5.2.3 Collective cell migration

During embryonic morphogenesis and cancer cell invasion, cells do not migrate as single entities, but connected, both physically and functionally, to other cell types (176). In contrast to single cell migration, however, little is known about how mechanotransduction propagates during collective cell migration. Hence it would be interesting to understand how cells translate mechanical factors from neighboring cells, or the surrounding ECM, into coordinated multicellular motility. Specifically, it would be worthwhile to find out which molecular players are involved in the migratory response of multicellular structures to varying rigidity, topology and adhesive area. To visualize the activities of specific proteins during migration, quantitative live imaging skills could be adopted (141). In combination with our force sensors, this live imaging skill can help build a platform to measure spatio-temporal signaling activities at cytoskeletons, adherens junctions and focal adhesion in migrating multi-cells.

It would be also interesting to tailor and expand the multiphysics migration model into a collective cell migration model, and use it for the prediction of in-vivo acts of mass cell migration – e.g. collective cell migration within a 3D gel, or stem cell migration from a

tissue scaffold into a damaged tissue. One could also test how cells in 3D sense three-dimensional mechanical cues in-vivo. I believe that prediction via an appropriate multiphysics model will reveal certain aspects difficult to observe experimentally. This multidisciplinary understanding of the biomechanical principles behind collective cell movement will lead to the development of appropriate strategies for controlling collective cell migration during morphogenesis, wound healing, and cancer invasion.

5.3 Final Thoughts

This thesis attempts to address the question of how cells sense mechanical factors in their environment by generating forces and how they use forces to migrate. Although the work contained in this thesis is considerable, it is just a small piece in a billion-piece puzzle. The area of cell contractility and migration is so inconceivably vast that it has filled up many journals, consortium, conferences and research grants. Mechanotransduction and cell migration is definitely important for many important biological processes and human diseases such as wound healing and cancer progression. This thesis answers fundamental questions about mechanosensation and cell migration. It is my desire that it will help build the groundwork that will ultimately contribute to improvement of human health.

References

1. Deshpande, V. S., R. M. McMeeking, and A. G. Evans. 2006. A bio-chemo-mechanical model for cell contractility. Proc Natl Acad Sci U S A 103:14015-14020.
2. Cramer, L. P., M. Siebert, and T. J. Mitchison. 1997. Identification of novel graded polarity actin filament bundles in locomoting heart fibroblasts: implications for the generation of motile force. J Cell Biol 136:1287-1305.
3. Vicente-Manzanares, M., X. Ma, R. S. Adelstein, and A. R. Horwitz. 2009. Non-muscle myosin II takes centre stage in cell adhesion and migration. Nat Rev Mol Cell Biol 10:778-790.
4. Jiang, M. Y., and M. P. Sheetz. 1994. Mechanics of myosin motor: force and step size. Bioessays 16:531-532.
5. Burridge, K., and K. Wennerberg. 2004. Rho and Rac take center stage. Cell 116:167-179.
6. Smith, M. L., D. Gourdon, W. C. Little, K. E. Kubow, R. A. Eguiluz, S. Luna-Morris, and V. Vogel. 2007. Force-induced unfolding of fibronectin in the extracellular matrix of living cells. PLoS Biol 5:e268.
7. Geiger, B., J. P. Spatz, and A. D. Bershadsky. 2009. Environmental sensing through focal adhesions. Nat Rev Mol Cell Biol 10:21-33.
8. Hynes, R. O. 1992. Integrins: versatility, modulation, and signaling in cell adhesion. Cell 69:11-25.
9. Alberts, B. 2002. Molecular biology of the cell. Garland Science, New York.
10. Alexandrova, A. Y., K. Arnold, S. Schaub, J. M. Vasiliev, J. J. Meister, A. D. Bershadsky, and A. B. Verkhovsky. 2008. Comparative dynamics of retrograde actin flow and focal adhesions: formation of nascent adhesions triggers transition from fast to slow flow. PLoS One 3:e3234.
11. Choi, C. K., M. Vicente-Manzanares, J. Zareno, L. A. Whitmore, A. Mogilner, and A. R. Horwitz. 2008. Actin and alpha-actinin orchestrate the assembly and

maturation of nascent adhesions in a myosin II motor-independent manner. Nat Cell Biol 10:1039-1050.

12. Geiger, B., A. Bershadsky, R. Pankov, and K. M. Yamada. 2001. Transmembrane crosstalk between the extracellular matrix--cytoskeleton crosstalk. Nat Rev Mol Cell Biol 2:793-805.

13. Pellegrin, S., and H. Mellor. 2007. Actin stress fibres. J Cell Sci 120:3491-3499.

14. Even-Ram, S., A. D. Doyle, M. A. Conti, K. Matsumoto, R. S. Adelstein, and K. M. Yamada. 2007. Myosin IIA regulates cell motility and actomyosin-microtubule crosstalk. Nat Cell Biol 9:299-309.

15. Vicente-Manzanares, M., J. Zareno, L. Whitmore, C. K. Choi, and A. F. Horwitz. 2007. Regulation of protrusion, adhesion dynamics, and polarity by myosins IIA and IIB in migrating cells. J Cell Biol 176:573-580.

16. Galbraith, C. G., and M. P. Sheetz. 1998. Forces on adhesive contacts affect cell function. Curr Opin Cell Biol 10:566-571.

17. Saez, A., A. Buguin, P. Silberzan, and B. Ladoux. 2005. Is the mechanical activity of epithelial cells controlled by deformations or forces? In Biophysical Journal. L52-L54.

18. Lee, G. M., and R. F. Loeser. 1999. Cell surface receptors transmit sufficient force to bend collagen fibrils. Exp Cell Res 248:294-305.

19. Meshel, A. S., Q. Wei, R. S. Adelstein, and M. P. Sheetz. 2005. Basic mechanism of three-dimensional collagen fibre transport by fibroblasts. Nat Cell Biol 7:157-164.

20. Stopak, D., N. K. Wessells, and A. K. Harris. 1985. Morphogenetic rearrangement of injected collagen in developing chicken limb buds. Proc Natl Acad Sci U S A 82:2804-2808.

21. Montell, D. J. 2008. Morphogenetic cell movements: diversity from modular mechanical properties. Science 322:1502-1505.

22. Harris, A. K., P. Wild, and D. Stopak. 1980. Silicone rubber substrata: a new wrinkle in the study of cell locomotion. Science 208:177-179.

23. Chrzanowska-Wodnicka, M., and K. Burridge. 1996. Rho-stimulated contractility drives the formation of stress fibers and focal adhesions. J Cell Biol 133:1403-1415.

24. Helfman, D. M., E. T. Levy, C. Berthier, M. Shtutman, D. Riveline, I. Grosheva, A. Lachish-Zalait, M. Elbaum, and A. D. Bershadsky. 1999. Caldesmon inhibits nonmuscle cell contractility and interferes with the formation of focal adhesions. Mol Biol Cell 10:3097-3112.

25. Burton, K., and D. L. Taylor. 1997. Traction forces of cytokinesis measured with optically modified elastic substrata. Nature 385:450-454.

26. Burton, K., J. H. Park, and D. L. Taylor. 1999. Keratocytes generate traction forces in two phases. Mol Biol Cell 10:3745-3769.

27. Dembo, M., and Y. L. Wang. 1999. Stresses at the cell-to-substrate interface during locomotion of fibroblasts. Biophys J 76:2307-2316.

28. Lee, J., M. Leonard, T. Oliver, A. Ishihara, and K. Jacobson. 1994. Traction forces generated by locomoting keratocytes. J Cell Biol 127:1957-1964.

29. Dembo, M., T. Oliver, A. Ishihara, and K. Jacobson. 1996. Imaging the traction stresses exerted by locomoting cells with the elastic substratum method. Biophys J 70:2008-2022.

30. Pelham, R. J., Jr., and Y. Wang. 1997. Cell locomotion and focal adhesions are regulated by substrate flexibility. Proc Natl Acad Sci U S A 94:13661-13665.

31. Wang, Y. L., and R. J. Pelham, Jr. 1998. Preparation of a flexible, porous polyacrylamide substrate for mechanical studies of cultured cells. Methods Enzymol 298:489-496.

32. Bernardo, J. M., and A. F. M. Smith. 2000. Bayesian theory. Wiley, Chichester ; New York.

33. Landau, L. D., E. M. Lifshi*t*s, A. d. M. Kosevich, and L. P. Pitaevski*i. 1986. Theory of elasticity. Pergamon Press, Oxford [Oxfordshire] ; New York.

34. Balaban, N. Q., U. S. Schwarz, D. Riveline, P. Goichberg, G. Tzur, I. Sabanay, D. Mahalu, S. Safran, A. Bershadsky, L. Addadi, and B. Geiger. 2001. Force and focal adhesion assembly: a close relationship studied using elastic micropatterned substrates. Nat Cell Biol 3:466-472.

35. Munevar, S., Y. Wang, and M. Dembo. 2001. Traction force microscopy of migrating normal and H-ras transformed 3T3 fibroblasts. Biophys J 80:1744-1757.

36. Discher, D. E., P. Janmey, and Y. L. Wang. 2005. Tissue cells feel and respond to the stiffness of their substrate. Science 310:1139-1143.

37. Lo, C. M., H. B. Wang, M. Dembo, and Y. L. Wang. 2000. Cell movement is guided by the rigidity of the substrate. Biophys J 79:144-152.

38. Isenberg, B. C., P. A. Dimilla, M. Walker, S. Kim, and J. Y. Wong. 2009. Vascular smooth muscle cell durotaxis depends on substrate stiffness gradient strength. Biophys J 97:1313-1322.

39. Folkman, J., and A. Moscona. 1978. Role of cell shape in growth control. Nature 273:345-349.

40. Engler, A. J., C. Carag-Krieger, C. P. Johnson, M. Raab, H. Y. Tang, D. W. Speicher, J. W. Sanger, J. M. Sanger, and D. E. Discher. 2008. Embryonic cardiomyocytes beat best on a matrix with heart-like elasticity: scar-like rigidity inhibits beating. J Cell Sci 121:3794-3802.

41. Engler, A. J., S. Sen, H. L. Sweeney, and D. E. Discher. 2006. Matrix elasticity directs stem cell lineage specification. Cell 126:677-689.

42. Paszek, M. J., N. Zahir, K. R. Johnson, J. N. Lakins, G. I. Rozenberg, A. Gefen, C. A. Reinhart-King, S. S. Margulies, M. Dembo, D. Boettiger, D. A. Hammer, and V. M. Weaver. 2005. Tensional homeostasis and the malignant phenotype. Cancer Cell 8:241-254.

43. Levental, K. R., H. Yu, L. Kass, J. N. Lakins, M. Egeblad, J. T. Erler, S. F. Fong, K. Csiszar, A. Giaccia, W. Weninger, M. Yamauchi, D. L. Gasser, and V. M. Weaver. 2009. Matrix crosslinking forces tumor progression by enhancing integrin signaling. Cell 139:891-906.

44. Engler, A., L. Bacakova, C. Newman, A. Hategan, M. Griffin, and D. Discher. 2004. Substrate compliance versus ligand density in cell on gel responses. Biophys J 86:617-628.

45. Gaudet, C., W. A. Marganski, S. Kim, C. T. Brown, V. Gunderia, M. Dembo, and J. Y. Wong. 2003. Influence of type I collagen surface density on fibroblast spreading, motility, and contractility. Biophys J 85:3329-3335.

46. Rajagopalan, P., W. A. Marganski, X. Q. Brown, and J. Y. Wong. 2004. Direct comparison of the spread area, contractility, and migration of balb/c 3T3 fibroblasts adhered to fibronectin- and RGD-modified substrata. Biophys J 87:2818-2827.

47. Reinhart-King, C. A., M. Dembo, and D. A. Hammer. 2005. The dynamics and mechanics of endothelial cell spreading. Biophys J 89:676-689.

48. Arnold, M., E. A. Cavalcanti-Adam, R. Glass, J. Blummel, W. Eck, M. Kantlehner, H. Kessler, and J. P. Spatz. 2004. Activation of integrin function by nanopatterned adhesive interfaces. Chemphyschem 5:383-388.

49. Harris, A. 1973. Behavior of cultured cells on substrata of variable adhesiveness. Exp Cell Res 77:285-297.

50. Inoue, S., Y. Iida, Y. Otani, Y. Hirano, and Y. Tabata. 2009. Adhesion behavior of human adipo-stromal cells on self-assembled monolayers with different surface densities or gradients of RGD peptide. J Biomater Sci Polym Ed 20:495-510.

51. Cukierman, E., R. Pankov, D. R. Stevens, and K. M. Yamada. 2001. Taking cell-matrix adhesions to the third dimension. Science 294:1708-1712.

52. Beningo, K. A., M. Dembo, and Y. L. Wang. 2004. Responses of fibroblasts to anchorage of dorsal extracellular matrix receptors. Proc Natl Acad Sci U S A 101:18024-18029.

53. Maskarinec, S. A., C. Franck, D. A. Tirrell, and G. Ravichandran. 2009. Quantifying cellular traction forces in three dimensions. Proc Natl Acad Sci U S A 106:22108-22113.

54. Legant, W. R., J. S. Miller, B. L. Blakely, D. M. Cohen, G. M. Genin, and C. S. Chen. 2010. Measurement of mechanical tractions exerted by cells in three-dimensional matrices. Nat Methods 7:969-971.

55. Discher, D., C. Dong, J. J. Fredberg, F. Guilak, D. Ingber, P. Janmey, R. D. Kamm, G. W. Schmid-Schonbein, and S. Weinbaum. 2009. Biomechanics: cell research and applications for the next decade. Ann Biomed Eng 37:847-859.

56. Even-Ram, S., and K. M. Yamada. 2005. Cell migration in 3D matrix. Curr Opin Cell Biol 17:524-532.

57. du Roure, O., A. Saez, A. Buguin, R. H. Austin, P. Chavrier, P. Silberzan, and B. Ladoux. 2005. Force mapping in epithelial cell migration. Proc Natl Acad Sci U S A 102:2390-2395.

58. Galbraith, C. G., and M. P. Sheetz. 1997. A micromachined device provides a new bend on fibroblast traction forces. Proc Natl Acad Sci U S A 94:9114-9118.

59. Tan, J. L., J. Tien, D. M. Pirone, D. S. Gray, K. Bhadriraju, and C. S. Chen. 2003. Cells lying on a bed of microneedles: an approach to isolate mechanical force. Proc Natl Acad Sci U S A 100:1484-1489.

60. Lemmon, C. A., N. J. Sniadecki, S. A. Ruiz, J. L. Tan, L. H. Romer, and C. S. Chen. 2005. Shear force at the cell-matrix interface: enhanced analysis for microfabricated post array detectors. Mech Chem Biosyst 2:1-16.

61. Ghibaudo, M., A. Saez, L. Trichet, A. Xayaphoummine, J. Browaeys, P. Silberzan, A. Buguin, and B. Ladoux. 2008. Traction forces and rigidity sensing regulate cell functions. Soft Matter 4:1836-1843.

62. Moore, S. W., P. Roca-Cusachs, and M. P. Sheetz. 2010. Stretchy proteins on stretchy substrates: the important elements of integrin-mediated rigidity sensing. Dev Cell 19:194-206.

63. Tan, J. L., W. Liu, C. M. Nelson, S. Raghavan, and C. S. Chen. 2004. Simple approach to micropattern cells on common culture substrates by tuning substrate wettability. Tissue Eng 10:865-872.

64. Liu, Z., J. L. Tan, D. M. Cohen, M. T. Yang, N. J. Sniadecki, S. A. Ruiz, C. M. Nelson, and C. S. Chen. 2010. Mechanical tugging force regulates the size of cell-cell junctions. Proc Natl Acad Sci U S A 107:9944-9949.

65. Nelson, C. M., R. P. Jean, J. L. Tan, W. F. Liu, N. J. Sniadecki, A. A. Spector, and C. S. Chen. 2005. Emergent patterns of growth controlled by multicellular form and mechanics. Proc Natl Acad Sci U S A 102:11594-11599.

66. Ruiz, S. A., and C. S. Chen. 2008. Emergence of patterned stem cell differentiation within multicellular structures. Stem Cells 26:2921-2927.

67. Vogel, V., and M. Sheetz. 2006. Local force and geometry sensing regulate cell functions. Nat Rev Mol Cell Biol 7:265-275.

68. Chen, C. S. 2008. Mechanotransduction - a field pulling together? J Cell Sci 121:3285-3292.

69. Schwartz, M. A. 2010. Integrins and extracellular matrix in mechanotransduction. Cold Spring Harb Perspect Biol 2:a005066.

70. Ridley, A. J., M. A. Schwartz, K. Burridge, R. A. Firtel, M. H. Ginsberg, G. Borisy, J. T. Parsons, and A. R. Horwitz. 2003. Cell migration: integrating signals from front to back. Science 302:1704-1709.

71. Geiger, B., A. Bershadsky, R. Pankov, and K. M. Yamada. 2001. Transmembrane extracellular matrix--cytoskeleton crosstalk. Nat Rev Mol Cell Biol 2:793-805.

72. Puklin-Faucher, E., and M. P. Sheetz. 2009. The mechanical integrin cycle. J Cell Sci 122:179-186.

73. Klein, E. A., L. Yin, D. Kothapalli, P. Castagnino, F. J. Byfield, T. Xu, I. Levental, E. Hawthorne, P. A. Janmey, and R. K. Assoian. 2009. Cell-cycle control by physiological matrix elasticity and in vivo tissue stiffening. Curr Biol 19:1511-1518.

74. Chen, C. S., M. Mrksich, S. Huang, G. M. Whitesides, and D. E. Ingber. 1997. Geometric control of cell life and death. Science 276:1425-1428.

75. Huang, S., C. S. Chen, and D. E. Ingber. 1998. Control of cyclin D1, p27(Kip1), and cell cycle progression in human capillary endothelial cells by cell shape and cytoskeletal tension. Mol Biol Cell 9:3179-3193.

76. McBeath, R., D. M. Pirone, C. M. Nelson, K. Bhadriraju, and C. S. Chen. 2004. Cell shape, cytoskeletal tension, and RhoA regulate stem cell lineage commitment. Dev Cell 6:483-495.

77. Wang, N., E. Ostuni, G. M. Whitesides, and D. E. Ingber. 2002. Micropatterning tractional forces in living cells. Cell Motil Cytoskeleton 52:97-106.

78. Saez, A., A. Buguin, P. Silberzan, and B. Ladoux. 2005. Is the mechanical activity of epithelial cells controlled by deformations or forces? Biophys J 89:L52-54.

79. Mitrossilis, D., J. Fouchard, A. Guiroy, N. Desprat, N. Rodriguez, B. Fabry, and A. Asnacios. 2009. Single-cell response to stiffness exhibits muscle-like behavior. Proc Natl Acad Sci U S A 106:18243-18248.

80. Califano, J. P., and C. A. Reinhart-King. 2010. Substrate Stiffness and Cell Area Predict Cellular Traction Stresses in Single Cells and Cells in Contact. Cell Mol Bioeng 3:68-75.

81. Engler, A., L. Bacakova, C. Newman, A. Hategan, M. Griffin, and D. Discher. 2004. Substrate compliance versus ligand density in cell on gel responses. Biophysical Journal 86:617-628.

82. Reinhart-King, C. A., M. Dembo, and D. A. Hammer. 2003. Endothelial cell traction forces on RGD-derivatized polyacrylamide substrata. Langmuir 19:1573-1579.

83. Tolic-Norrelykke, I. M., and N. Wang. 2005. Traction in smooth muscle cells varies with cell spreading. J Biomech 38:1405-1412.

84. Fu, J., Y. K. Wang, M. T. Yang, R. A. Desai, X. Yu, Z. Liu, and C. S. Chen. 2010. Mechanical regulation of cell function with geometrically modulated elastomeric substrates. Nat Methods 7:733-736.

85. Rape, A. D., W. H. Guo, and Y. L. Wang. 2011. The regulation of traction force in relation to cell shape and focal adhesions. Biomaterials 32:2043-2051.

86. Yeung, T., P. C. Georges, L. A. Flanagan, B. Marg, M. Ortiz, M. Funaki, N. Zahir, W. Ming, V. Weaver, and P. A. Janmey. 2005. Effects of substrate stiffness on cell morphology, cytoskeletal structure, and adhesion. Cell Motil Cytoskeleton 60:24-34.

87. Sniadecki, N. J., and C. S. Chen. 2007. Microfabricated silicone elastomeric post arrays for measuring traction forces of adherent cells. Methods Cell Biol 83:313-328.

88. del Rio, A., R. Perez-Jimenez, R. Liu, P. Roca-Cusachs, J. M. Fernandez, and M. P. Sheetz. 2009. Stretching single talin rod molecules activates vinculin binding. Science 323:638-641.

89. Giannone, G., and M. P. Sheetz. 2006. Substrate rigidity and force define form through tyrosine phosphatase and kinase pathways. Trends Cell Biol 16:213-223.

90. Cai, Y., N. Biais, G. Giannone, M. Tanase, G. Jiang, J. M. Hofman, C. H. Wiggins, P. Silberzan, A. Buguin, B. Ladoux, and M. P. Sheetz. 2006. Nonmuscle myosin IIA-dependent force inhibits cell spreading and drives F-actin flow. Biophys J 91:3907-3920.

91. Hotulainen, P., and P. Lappalainen. 2006. Stress fibers are generated by two distinct actin assembly mechanisms in motile cells. J Cell Biol 173:383-394.

92. Park, C. Y., D. Tambe, A. M. Alencar, X. Trepat, E. H. Zhou, E. Millet, J. P. Butler, and J. J. Fredberg. 2010. Mapping the cytoskeletal prestress. Am J Physiol Cell Physiol 298:C1245-1252.

93. Tee, S. Y., J. Fu, C. S. Chen, and P. A. Janmey. 2011. Cell shape and substrate rigidity both regulate cell stiffness. Biophys J 100:L25-27.

94. McGarry, J. P., J. Fu, M. T. Yang, C. S. Chen, R. M. McMeeking, A. G. Evans, and V. S. Deshpande. 2009. Simulation of the contractile response of cells on an array of micro-posts. Philos Transact A Math Phys Eng Sci 367:3477-3497.

95. Deeg, J. A., I. Louban, D. Aydin, C. Selhuber-Unkel, H. Kessler, and J. P. Spatz. 2011. Impact of local versus global ligand density on cellular adhesion. Nano Lett 11:1469-1476.

96. Rodriguez, A. G., S. J. Han, M. Regnier, and N. J. Sniadecki. 2011. Substrate stiffness increases twitch power of neonatal cardiomyocytes in correlation with changes in myofibril structure and intracellular calcium. Biophys J 101:2455-2464.

97. Goffin, J. M., P. Pittet, G. Csucs, J. W. Lussi, J. J. Meister, and B. Hinz. 2006. Focal adhesion size controls tension-dependent recruitment of alpha-smooth muscle actin to stress fibers. J Cell Biol 172:259-268.

98. Beningo, K. A., M. Dembo, I. Kaverina, J. V. Small, and Y. L. Wang. 2001. Nascent focal adhesions are responsible for the generation of strong propulsive forces in migrating fibroblasts. J Cell Biol 153:881-888.

99. Stricker, J., Y. Aratyn-Schaus, P. W. Oakes, and M. L. Gardel. 2011. Spatiotemporal constraints on the force-dependent growth of focal adhesions. Biophys J 100:2883-2893.

100. Bray, D. 2001. Cell movements : from molecules to motility. Garland Pub., New York.

101. Chicurel, M. 2002. Cell biology. Cell migration research is on the move. Science 295:606-609.

102. Chaplain, M. A. 2000. Mathematical modelling of angiogenesis. J Neurooncol 50:37-51.

103. Gerisch, A., and M. A. Chaplain. 2008. Mathematical modelling of cancer cell invasion of tissue: local and non-local models and the effect of adhesion. J Theor Biol 250:684-704.

104. Thackham, J. A., D. L. McElwain, and I. W. Turner. 2009. Computational approaches to solving equations arising from wound healing. Bull Math Biol 71:211-246.

105. Tranquillo, R. T., D. A. Lauffenburger, and S. H. Zigmond. 1988. A stochastic model for leukocyte random motility and chemotaxis based on receptor binding fluctuations. J Cell Biol 106:303-309.

106. Lauffenburger, D. A., and A. F. Horwitz. 1996. Cell migration: a physically integrated molecular process. Cell 84:359-369.

107. Sheetz, M. P., D. Felsenfeld, C. G. Galbraith, and D. Choquet. 1999. Cell migration as a five-step cycle. Biochem Soc Symp 65:233-243.

108. Devreotes, P. N., and S. H. Zigmond. 1988. Chemotaxis in eukaryotic cells: a focus on leukocytes and Dictyostelium. Annu Rev Cell Biol 4:649-686.

109. Carter, S. B. 1967. Haptotaxis and the mechanism of cell motility. Nature 213:256-260.

110. Li, S., P. Butler, Y. Wang, Y. Hu, D. C. Han, S. Usami, J. L. Guan, and S. Chien. 2002. The role of the dynamics of focal adhesion kinase in the mechanotaxis of endothelial cells. Proc Natl Acad Sci U S A 99:3546-3551.

111. Mogilner, A., and G. Oster. 1996. Cell motility driven by actin polymerization. Biophys J 71:3030-3045.

112. Kirfel, G., A. Rigort, B. Borm, and V. Herzog. 2004. Cell migration: mechanisms of rear detachment and the formation of migration tracks. Eur J Cell Biol 83:717-724.

113. Rigort, A., J. Grunewald, V. Herzog, and G. Kirfel. 2004. Release of integrin macroaggregates as a mechanism of rear detachment during keratinocyte migration. Eur J Cell Biol 83:725-733.

114. DiMilla, P. A., K. Barbee, and D. A. Lauffenburger. 1991. Mathematical model for the effects of adhesion and mechanics on cell migration speed. Biophys J 60:15-37.

115. Gracheva, M. E., and H. G. Othmer. 2004. A continuum model of motility in ameboid cells. Bull Math Biol 66:167-193.

116. Maree, A. F., A. Jilkine, A. Dawes, V. A. Grieneisen, and L. Edelstein-Keshet. 2006. Polarization and movement of keratocytes: a multiscale modelling approach. Bull Math Biol 68:1169-1211.

117. Dokukina, I. V., and M. E. Gracheva. A model of fibroblast motility on substrates with different rigidities. Biophys J 98:2794-2803.

118. Deshpande, V. S., R. M. McMeeking, and A. G. Evans. 2007. A model for the contractility of the cytoskeleton including the effects of stress-fibre formation and dissociation. Proceedings of the Royal Society a-Mathematical Physical and Engineering Sciences 463:787-815.

119. Mathur, A., P. Roca-Cusachs, O. M. Rossier, S. J. Wind, M. P. Sheetz, and J. Hone. 2011. New approach for measuring protrusive forces in cells. Journal of Vacuum Science & Technology B 29.

120. Li, S., J. L. Guan, and S. Chien. 2005. Biochemistry and biomechanics of cell motility. Annu Rev Biomed Eng 7:105-150.

121. Chaudhuri, O., S. H. Parekh, W. A. Lam, and D. A. Fletcher. 2009. Combined atomic force microscopy and side-view optical imaging for mechanical studies of cells. Nat Methods 6:383-387.

122. Guo, B., and W. H. Guilford. 2006. Mechanics of actomyosin bonds in different nucleotide states are tuned to muscle contraction. Proc Natl Acad Sci U S A 103:9844-9849.

123. Prass, M., K. Jacobson, A. Mogilner, and M. Radmacher. 2006. Direct measurement of the lamellipodial protrusive force in a migrating cell. J Cell Biol 174:767-772.

124. Parekh, S. H., O. Chaudhuri, J. A. Theriot, and D. A. Fletcher. 2005. Loading history determines the velocity of actin-network growth. Nat Cell Biol 7:1219-1223.

125. McMahon, T. A. 1984. Muscles, reflexes, and locomotion. Princeton University Press, Princeton, N.J.

126. Hill, A. V. 1938. The heat of shortening and the dynamic constants of muscle. Proceedings of the Royal Society of London Series B-Biological Sciences 126:136-195.

127. Euler, L. 1824. Institutionum calculi integralis. Impensis Academiae Imperialis Scientiarum, Petropoli.

128. Guilak, F., J. R. Tedrow, and R. Burgkart. 2000. Viscoelastic properties of the cell nucleus. Biochem Biophys Res Commun 269:781-786.

129. Trickey, W. R., F. P. Baaijens, T. A. Laursen, L. G. Alexopoulos, and F. Guilak. 2006. Determination of the Poisson's ratio of the cell: recovery properties of chondrocytes after release from complete micropipette aspiration. J Biomech 39:78-87.

130. Rape, A. D., W. H. Guo, and Y. L. Wang. The regulation of traction force in relation to cell shape and focal adhesions. Biomaterials 32:2043-2051.

131. Roy, P., W. M. Petroll, C. J. Chuong, H. D. Cavanagh, and J. V. Jester. 1999. Effect of cell migration on the maintenance of tension on a collagen matrix. Ann Biomed Eng 27:721-730.

132. Del Alamo, J. C., R. Meili, B. Alonso-Latorre, J. Rodriguez-Rodriguez, A. Aliseda, R. A. Firtel, and J. C. Lasheras. 2007. Spatio-temporal analysis of eukaryotic cell motility by improved force cytometry. Proc Natl Acad Sci U S A 104:13343-13348.

133. Ren, X. D., R. Wang, Q. Li, L. A. Kahek, K. Kaibuchi, and R. A. Clark. 2004. Disruption of Rho signal transduction upon cell detachment. J Cell Sci 117:3511-3518.

134. Zeng, Q., D. Lagunoff, R. Masaracchia, Z. Goeckeler, G. Cote, and R. Wysolmerski. 2000. Endothelial cell retraction is induced by PAK2 monophosphorylation of myosin II. J Cell Sci 113 (Pt 3):471-482.

135. Huang, X., D. Wu, H. Jin, D. Stupack, and J. Y. Wang. 2008. Induction of cell retraction by the combined actions of Abl-CrkII and Rho-ROCK1 signaling. J Cell Biol 183:711-723.

136. Sen, S., A. J. Engler, and D. E. Discher. 2009. Matrix strains induced by cells: Computing how far cells can feel. Cell Mol Bioeng 2:39-48.

137. Wildt, B., D. Wirtz, and P. C. Searson. 2009. Programmed subcellular release for studying the dynamics of cell detachment. Nat Methods 6:211-213.

138. Crowley, E., and A. F. Horwitz. 1995. Tyrosine phosphorylation and cytoskeletal tension regulate the release of fibroblast adhesions. J Cell Biol 131:525-537.

139. Palecek, S. P., A. Huttenlocher, A. F. Horwitz, and D. A. Lauffenburger. 1998. Physical and biochemical regulation of integrin release during rear detachment of migrating cells. J Cell Sci 111 (Pt 7):929-940.

140. Parsons, J. T., A. R. Horwitz, and M. A. Schwartz. 2010. Cell adhesion: integrating cytoskeletal dynamics and cellular tension. Nat Rev Mol Cell Biol 11:633-643.

141. Machacek, M., L. Hodgson, C. Welch, H. Elliott, O. Pertz, P. Nalbant, A. Abell, G. L. Johnson, K. M. Hahn, and G. Danuser. 2009. Coordination of Rho GTPase activities during cell protrusion. Nature 461:99-103.

142. Groeger, G., and C. D. Nobes. 2007. Co-operative Cdc42 and Rho signalling mediates ephrinB-triggered endothelial cell retraction. Biochem J 404:23-29.

143. Kim, D. H., C. H. Seo, K. Han, K. W. Kwon, A. Levchenko, and K. Y. Suh. 2009. Guided Cell Migration on Microtextured Substrates with Variable Local Density and Anisotropy. Adv Funct Mater 19:1579-1586.

144. Deshpande, V. S., M. Mrksich, R. M. McMeeking, and A. G. Evans. 2008. A bio-mechanical model for coupling cell contractility with focal adhesion formation. Journal of the Mechanics and Physics of Solids 56:1484-1510.

145. Deguchi, S., T. Ohashi, and M. Sato. 2006. Tensile properties of single stress fibers isolated from cultured vascular smooth muscle cells. J Biomech 39:2603-2610.

146. Hochmuth, R. M. 2000. Micropipette aspiration of living cells. J Biomech 33:15-22.

147. Ketene, A. N., P. C. Roberts, A. A. Shea, E. M. Schmelz, and M. Agah. Actin filaments play a primary role for structural integrity and viscoelastic response in cells. Integr Biol (Camb).

148. Solon, J., I. Levental, K. Sengupta, P. C. Georges, and P. A. Janmey. 2007. Fibroblast adaptation and stiffness matching to soft elastic substrates. Biophys J 93:4453-4461.

149. Ingber, D. E. 1997. Tensegrity: the architectural basis of cellular mechanotransduction. Annu Rev Physiol 59:575-599.

150. Pelham, R. J., Jr., and Y. Wang. 1999. High resolution detection of mechanical forces exerted by locomoting fibroblasts on the substrate. Mol Biol Cell 10:935-945.

151. Oliver, T., J. Lee, and K. Jacobson. 1994. Forces exerted by locomoting cells. Semin Cell Biol 5:139-147.

152. Doyle, A. D., F. W. Wang, K. Matsumoto, and K. M. Yamada. 2009. One-dimensional topography underlies three-dimensional fibrillar cell migration. J Cell Biol 184:481-490.

153. Petrie, R. J., A. D. Doyle, and K. M. Yamada. 2009. Random versus directionally persistent cell migration. Nat Rev Mol Cell Biol 10:538-549.

154. Ricart, B. G., M. T. Yang, C. A. Hunter, C. S. Chen, and D. A. Hammer. 2012. Measuring traction forces of motile dendritic cells on micropost arrays. Biophys J 101:2620-2628.

155. Kanazawa, S., T. Fujiwara, S. Matsuzaki, K. Shingaki, M. Taniguchi, S. Miyata, M. Tohyama, Y. Sakai, K. Yano, K. Hosokawa, and T. Kubo. bFGF regulates PI3-kinase-Rac1-JNK pathway and promotes fibroblast migration in wound healing. PLoS One 5:e12228.

156. Rodriguez, A. G., S. J. Han, M. Regnier, and N. J. Sniadecki. Substrate stiffness increases twitch power of neonatal cardiomyocytes in correlation with changes in myofibril structure and intracellular calcium. Biophys J 101:2455-2464.

157. Han, S. J., and N. J. Sniadecki. 2010. Simulations of the contractile cycle in cell migration using a bio-chemical-mechanical model. Comput Methods Biomech Biomed Engin 14:459-468.

158. Haga, H., S. Sasaki, K. Kawabata, E. Ito, T. Ushiki, and T. Sambongi. 2000. Elasticity mapping of living fibroblasts by AFM and immunofluorescence observation of the cytoskeleton. Ultramicroscopy 82:253-258.

159. Wang, N., K. Naruse, D. Stamenovic, J. J. Fredberg, S. M. Mijailovich, I. M. Tolic-Norrelykke, T. Polte, R. Mannix, and D. E. Ingber. 2001. Mechanical behavior in living cells consistent with the tensegrity model. Proc Natl Acad Sci U S A 98:7765-7770.

160. Edman, K. A. 1988. Double-hyperbolic force-velocity relation in frog muscle fibres. J Physiol 404:301-321.

161. Huttenlocher, A., and A. R. Horwitz. Integrins in cell migration. Cold Spring Harb Perspect Biol 3:a005074.

162. Heinrich, R., B. G. Neel, and T. A. Rapoport. 2002. Mathematical models of protein kinase signal transduction. Mol Cell 9:957-970.

163. Han, S. J., and N. J. Sniadecki. 2011. Simulations of the contractile cycle in cell migration using a bio-chemical-mechanical model. Comput Methods Biomech Biomed Engin 14:459-468.

164. Kole, T. P., Y. Tseng, I. Jiang, J. L. Katz, and D. Wirtz. 2005. Intracellular mechanics of migrating fibroblasts. Mol Biol Cell 16:328-338.

165. Sanchez, D., N. Johnson, C. Li, P. Novak, J. Rheinlaender, Y. Zhang, U. Anand, P. Anand, J. Gorelik, G. I. Frolenkov, C. Benham, M. Lab, V. P. Ostanin, T. E. Schaffer, D. Klenerman, and Y. E. Korchev. 2008. Noncontact measurement of the local mechanical properties of living cells using pressure applied via a pipette. Biophys J 95:3017-3027.

166. Haupt, B. J., M. Osbourn, R. Spanhoff, S. de Keijzer, A. Muller-Taubenberger, E. Snaar-Jagalska, and T. Schmidt. 2007. Asymmetric elastic properties of Dictyostelium discoideum in relation to chemotaxis. Langmuir 23:9352-9357.

167. Thomas, W. E., V. Vogel, and E. Sokurenko. 2008. Biophysics of catch bonds. Annu Rev Biophys 37:399-416.

168. Felsenfeld, D. P., P. L. Schwartzberg, A. Venegas, R. Tse, and M. P. Sheetz. 1999. Selective regulation of integrin--cytoskeleton interactions by the tyrosine kinase Src. Nat Cell Biol 1:200-206.

169. Galbraith, C. G., K. M. Yamada, and M. P. Sheetz. 2002. The relationship between force and focal complex development. J Cell Biol 159:695-705.

170. von Wichert, G., B. Haimovich, G. S. Feng, and M. P. Sheetz. 2003. Force-dependent integrin-cytoskeleton linkage formation requires downregulation of focal complex dynamics by Shp2. EMBO J 22:5023-5035.

171. Colombelli, J., A. Besser, H. Kress, E. G. Reynaud, P. Girard, E. Caussinus, U. Haselmann, J. V. Small, U. S. Schwarz, and E. H. Stelzer. 2009. Mechanosensing in

actin stress fibers revealed by a close correlation between force and protein localization. J Cell Sci 122:1665-1679.

172. Provenzano, P. P., and P. J. Keely. Mechanical signaling through the cytoskeleton regulates cell proliferation by coordinated focal adhesion and Rho GTPase signaling. J Cell Sci 124:1195-1205.

173. Sterpetti, P., L. Marucci, C. Candelaresi, D. Toksoz, G. Alpini, L. Ugili, G. S. Baroni, G. Macarri, and A. Benedetti. 2006. Cell proliferation and drug resistance in hepatocellular carcinoma are modulated by Rho GTPase signals. Am J Physiol Gastrointest Liver Physiol 290:G624-632.

174. Pertz, O., L. Hodgson, R. L. Klemke, and K. M. Hahn. 2006. Spatiotemporal dynamics of RhoA activity in migrating cells. Nature 440:1069-1072.

175. Gutierrez, E., E. Tkachenko, A. Besser, P. Sundd, K. Ley, G. Danuser, M. H. Ginsberg, and A. Groisman. High refractive index silicone gels for simultaneous total internal reflection fluorescence and traction force microscopy of adherent cells. PLoS One 6:e23807.

176. Friedl, P., and D. Gilmour. 2009. Collective cell migration in morphogenesis, regeneration and cancer. Nat Rev Mol Cell Biol 10:445-457.

Appendix A: Matlab Code for Mathematical Model in Aim 2

```
% contracting cell with matrix form and Euler method
% a cell on 7 posts
clear all;
close all;
M=8; %number of posts
kf = 3; %forward rate ()
kb = 2; %backward rate (depolymerization rate)
ks = 3.0; % spring constant of posts
Tmax = 1; %maximum tension
theta = 1; %decaying constant

%--- UH
MyEpsA = 1e-03; %size of perturbation
h = 0.0005; %step size for Euler

v0 = -0.3; % reference shortening rate
kv = 1.5; %fractional reduction in tension w.r.t. shortening rate

tmax = 75; % total time
N=tmax/h;
textend1 = 15; %time that a fiber is extended to the new post
Nextend1 = textend1/h;
trel1 = 2*textend1; % time of releasing old post
Nrel1 = trel1/h;
textend2 = 3*textend1; %time that a fiber is extended to the new post
Nextend2 = textend2/h;
trel2 = 4*textend1; % time of releasing old post
Nrel2 = trel2/h;

%Inital Memory Allocation including IC
eta = zeros(M,N); %there is no fiber at first row
x = zeros(M,N);
xdot = zeros(M,N);
T = zeros(M,N);
F = zeros(M,1);
y = zeros(M,N);
A = zeros(M,M);
% Tmat for T calculation
Tmat = zeros(M,M);
m_value = M-2;
a = Tmax*kv/v0;
mstart = 1;

for n=1:(N-1)
% for n = 1:((16/h)-1),

    t=n*h;
    if n> Nrel1 %at time of release
        mstart = 2;
        eta(2,n) = 0; %effect on eta
        x(1,n) = 0;
    end

    if n> Nrel2 %at time of release
        mstart = 3;
        eta(3,n) = 0; %effect on eta
        x(2,n) = 0;
    end

    if n > Nextend1
      %when extended
      m_value = M-1;
      tnew = t - textend1;
%                 eta(mstart:M-1,n+1)  =  eta(mstart:M-1,n)+  h*((1-eta(mstart:M-1,n))*exp(-
t/theta)*kf/theta ...
%             -(eta(mstart:M-1,n)-T(mstart:M-1,n)/Tmax)*kb/theta); %local activation
```

```
%         eta(M,n+1) = eta(M,n)+ h*((1-eta(M,n))*exp(-tnew/(theta))*kf/theta ...
%             -(eta(M,n)-T(M,n)/Tmax)*kb/theta); %local activation
      if n > Nextend2 %when extended
          m_value = M;
          tnew = t - textend2;
      end
      eta(mstart:m_value,n+1)  =  eta(mstart:m_value,n)+  h*((1-eta(mstart:m_value,n))*exp(-
tnew/theta)*kf/theta ...
          -(eta(mstart:m_value,n)-T(mstart:m_value,n)/Tmax)*kb/theta); %local activation
    else
      eta(mstart:m_value,n+1)  =  eta(mstart:m_value,n)+  h*((1-eta(mstart:m_value,n))*exp(-
t/theta)*kf/theta ...
         -(eta(mstart:m_value,n)-T(mstart:m_value,n)/Tmax)*kb/theta);
    end

%     if n> Nrel1 %activation on release
%         trel = t+1.95 - trel1;
%         eta(:,n+1) = eta(:,n)+ h*((1-eta(:,n))*exp(-trel/(theta))*kf/theta ...
%             -(eta(:,n)-T(:,n)/Tmax)*kb/theta);
%     end

    for i=mstart:m_value
        if i == mstart
            Tmat(i,i) = 10000;
        else
            Tmat(i,i) = -1;
        end
        if i<m_value
            Tmat(i,i+1) = 1;
        end
    end
    if m_value<M
        Tmat(M,M) = -10000;
    end
    if mstart>1
        Tmat(1,1) = 10000;
        Tmat(1,2) = 0;
    end
    if mstart>2
        Tmat(2,1) = 10000;
        Tmat(2,2) = 0;
    end

    %eta hard stop at 1
    if max(eta(:,n+1)>=1) ==1
        for i=1:M
            if eta(i,n+1)>=1
                eta(i,n+1)=1;
            end
        end
    end
    if min(eta(:,n)==0)==1 %if all members are 0 value in eta(:,n)
        x(:,n+1) = x(:,n);
    else
        %making A matrix and F vector
        A = zeros(M,M); %clearing A
        for i=mstart:m_value
            %for diagonal
            if i==mstart
                A(i,i) = -a;
                F(i) = eta(i+1,n)*Tmax;
            elseif i==m_value
                A(i,i) = -a;
                F(i) = -eta(i,n)*Tmax;
            else
                A(i,i) = -2*a;
                F(i) = eta(i+1,n)*Tmax - eta(i,n)*Tmax;
            end
            %for sub-diagonal components
```

```
            if i<m_value
                A(i,i+1) = a;
                A(i+1,i) = a;
            end
        end
        if mstart>1
           A(1,1) = 1;
           A0(1,1) = 1;
        end
        if m_value < M
            A(M,M) = 1;
            A0(M,M) = 1;
            F(M) = 0;
        end
        if m_value < M-1
            A(M-1,M-1) = 1;
            F(M-1) = 0;
            A(M,M) = 1;
            F(M) = 0;
        end

        %--- UH
        A0 = A;
        %---- Perturbations
%         A(mstart, mstart) = A(mstart, mstart) - MyEpsA * a;
        %--------------------
        % UH >> This perturbation is better.
        [Q0, D0] = eig(A0);
        index = find(abs(diag(D0)) < eps * max(abs(diag(D0))));
        A = A + Q0(:,index)*Q0(:,index)'*MyEpsA;
        %--------------------

        %xdot(:,n) = inv(A)*(F-ks*x(:,n));
        xdot(:,n) = A \ (F-ks*x(:,n));
        x(:,n+1) = x(:,n)+h*xdot(:,n);
    end
%     T(:,n+1) = Tmat\(ks*x(:,n+1));
    for i=mstart:M
        if i>mstart
            T(i,n+1)               =              Tmax*(eta(i,n+1)-kv/v0*(xdot(i,n)-xdot((i-
1),n)*(i>1)));%pinv(Tmat)*(ks*x(:,n+1));
        end
    end
    if n> Nrel1 %at time of release
        eta(2,n+1) = 0; %effect on eta
        x(1,n+1) = 0;
    end

    if n> Nrel2 %at time of release
        eta(3,n+1) = 0; %effect on eta
        x(2,n+1) = 0;
    end
%     if mstart>1
%         T(2,n+1) = 0; %effect on eta
%         x(1,n+1) = 0;
%     end
end
t=h:h:tmax;

% Results
% set(0,'DefaultAxesColorOrder',[0 0 0],...)
for i=2:M
    plot(t,T(i,:)./Tmax)
    hold all;
end
title('tension(T/Tmax)')
xlabel('time(t/theta)');
ylabel('T/Tmax');
```

```
legend('segment2','segment3','segment4','segment5','segment6','segment7','segment8','segmen
t9','segment10','segment11',-1);
hold off

figure;
for i=2:M
    plot(t,eta(i,:))
    hold all;
end
title('Activation level')
xlabel('time');
ylabel('eta');
legend('segment2','segment3','segment4','segment5','segment6','segment7','segment8','segmen
t9','segment10','segment11',-1);
hold off

figure;
for i=1:M
    plot(t,x(i,:))
    hold all;
end
title('deflection')
xlabel('time');
ylabel('post deflection');
legend('post1','post2','post3','post4','post5','post6','post7','post8',-1);
axis([0 75 -0.3 0.3])
hold off

t1=h:h:textend2;
figure;
for i=1:M
    plot(t1,x(i,1:Nextend2))
    hold all;
end
title('deflection')
xlabel('time');
ylabel('post deflection');
legend('post1','post2','post3','post4','post5','post6','post7','post8',-1);
axis([0 45 -0.3 0.3])
hold off

t2=textend2+h:h:tmax;
figure;
for i=1:M
    plot(t2,x(i,Nextend2+1:N))
    hold all;
end
title('deflection')
xlabel('time');
ylabel('post deflection');
legend('post1','post2','post3','post4','post5','post6','post7','post8',-1);
axis([45 75 -0.3 0.3])
hold off

% figure;
% totalx = zeros(1,tmax/h);
% for i=1:M
%     totalx = totalx + abs(x(i,:));
% end
% plot(t,ks*totalx)
% title('total forces')
% xlabel('Time (min)');
% ylabel('Total forces (nN)');

figure;
SE = zeros(1,tmax/h);
for i=1:M
    SE = SE + 0.5*ks*abs(x(i,:)).^2;
end
```

```
plot(t,SE)
title('Strain energy')
xlabel('Time');
ylabel('Strain energy');

figure;
plot(t1,SE(1:Nextend2))
title('Strain energy')
xlabel('Time');
ylabel('Strain energy');
axis([0 45 0 0.20])

figure;
plot(t2,SE(Nextend2+1:N))
title('Strain energy')
xlabel('Time');
ylabel('Strain energy');
axis([45 75 0 0.20])


figure;
FB = zeros(1,tmax/h);
for i=1:M
    FB = FB + ks*x(i,:);
end
plot(t,FB)
title('Force balance')
xlabel('Time');
ylabel('Force sum');
```

Appendix B: Matlab Code for Mathematical Model in Aim 3

```
%% Initialization
clear all;
close all;
kf = 3; %forward rate ()
kb = 2; %backward rate (backward rate)
ksf = .01; %forward rate for adhesion dynamics
ksb = 0.001; %backward rate for adhesion dynamics

Mtail = 1; %post number at the cell tail
Mlead = 6; %initial number of posts
Mnew = Mlead+1; %post number at the new adhesion

MyEpsA = 1e-03; %size of perturbation
%% Hill Constants
Tmax = 20; %maximum tension (nN)
vmax = -0.3; % reference shortening rate (um/min)
kv = .1; %fractional reduction in tension w.r.t. shortening rate
km = 0.25; %Muscle constant affecting curvature

%% Viscoelasticy of SLS 031012
kc1 = 0.1; %spring parallel to the maxwell spring-dashpot
kc2 = 0.1; %spring in maxwell component (series with dashpot)
muc = 2; %viscosity of a cell (nN s/um)
ks = 38; % nN/um, spring constant array of posts

% To make imperfect catch-bond
epse = 0.0; %epsilon eta
%% Activation Signal Constants
tau1=.8;
tau2=0.8;

%% Time
h = 0.005; %step size for Euler
tmax = 60; % total time
N=tmax/h+1;

%% Protrusion velocity and post spacing
v_pro = 2.25; %protrusion velocity (um/min)
d = 6; %post-to-post spacing (um)
p_b_link = 0.2; %probability to form a linkage between integrin and ligand

%% Cell parameters
ka = ones(Mnew,1)*100; % initial elasticy of adhesion
ka(Mnew,1) = 0; %zero adhesion at the new adhesion initially
ka_step = 0.00005*100;
Smax = 1.01;
S = ones(Mlead,N)*Smax; % initial adhesion strength
b_rel = zeros(Mlead,1); %boolean for release: b_rel(i)=1 means i-th SF is being released.

% S(Mnew,1) = 0; %zero adhesion at the new adhesion initially
S_step = 0.00003;
S_release_ratio = 0.3;
S_mature = 0.8;
rh = ones(Mnew,1); %rectangle handle

xdot = zeros(Mlead,N);
x = zeros(Mlead,N); %position of the end point of actin touching FA
xpost = zeros(Mlead,N); %position of each post
eta = zeros(Mlead-1,N); %there is no fiber at first
T = zeros(Mlead-1,N);
Tdot = zeros(Mlead-1,N);
F = zeros(Mlead-Mtail+1,1);
K = zeros(Mlead-Mtail+1,Mlead); %elasticity matrix for cell
```

```
% a = Tmax*km/vmax;
% mu_new = a - muc; %new viscotic coefficient
t_extend = 0;
n=0;
b_newadhesion = false;

b_link = false;
b_linked = false;
b_over = false;

b_release = false;
b_releasei = 0; %count for steps after release
b_release_limit = 1000;
x_pro = d*(Mlead-1);

% Write a video file
vidObj = VideoWriter('adhesion moving.avi');
open(vidObj);
set(gca,'nextplot','replacechildren');

set(gcf,'Position',[0, 100, 900, 600])
fscale = 0.1; %scale factor for force plot

%% Time course
for n=1:N
    t=(n-1)*h;
    % Graphic - adhesion (spacing between points = d = 5)
    x_real = x(:,n);
    xpost_real = xpost(:,n);
    x_origin = zeros(size(x(:,n)));
    x_real(Mnew) = 0;
    xpost_real(Mnew) = 0;
    x_origin(Mnew) = 0;


    for i=Mtail:Mnew
        x_real(i) = x_real(i) + d*(i-1);
        x_origin(i) = x_origin(i) + d*(i-1);
        xpost_real(i) = xpost_real(i) + d*(i-1);
    end
    %% protrusion advances with v_pro
    if b_linked == true
        x_pro = x_pro; %no protrusion until adhesion matures.
    elseif b_over == true
        x_pro = x_pro - (d-1);
        b_over = false;
%         x_pro = x_pro ; %protrusion becomes stochastic
    else
        x_pro = x_pro + random('Normal',v_pro,v_pro)*h;
    end
%% Overlap
    if x_pro >= xpost_real(Mnew)
        b_link = random('bino',1,p_b_link);
        if b_link==true

        else
            b_over = true;
        end
    end
    %% Visualizing
    if mod(n-1,2000)==0
        subplot(2,1,1)
        delete(findobj(gca,'Type','line'));
        delete(findobj(gca,'Type','text'));
        delete(findobj(gca,'Type','quiver'));
        y_cs=zeros(2,2*(Mlead-Mtail+1)); %cs: cell shape
        y_cs(:,1) = [x_real(Mtail); 1.4];
```

```
        for i=Mtail:Mlead-1
            y_cs(:,i-Mtail+2) = [(x_real(i)+x_real(i+1))/2; min(i-Mtail+1,Mlead-i)+1.4];
        end
        y_cs(:,Mlead-Mtail+2) = [x_pro; 0.5+1.4];
        y_cs(:,Mlead-Mtail+3) = [x_pro; 1.4];
        jj=0;
        for i=Mlead:-1:Mtail
            jj=jj+1;
            y_cs(:,Mlead-Mtail+3+jj) = [x_real(i); 1.4];
        end
        c = fnplt(cscvn(y_cs));
        fill(c(1,:),c(2,:),'g')
        for i=Mtail:Mlead
            if S(i,n)>0
                rh(i) = line([x_real(i)-S(i,n),x_real(i)+S(i,n)],[1,1],...
'LineWidth',S(i,n)*5,'Color',hsv2rgb([S(i,n)/Tmax,1,1])); %Adhesions
            end
        end

%         hold on,
%         plot(y_cs(1,:),y_cs(2,:),'o'), hold off

        hold on
        qscale = 10; % scaling factor for all vectors
        h1 = quiver(x_origin(Mtail:Mlead),-0.1*ones(size(x_origin(Mtail:Mlead))),...
            xpost(Mtail:Mlead,n),zeros(Mlead-Mtail+1,1),0,... % the '0' turns off auto-
scaling
            'LineWidth',2,'Color','k','MaxHeadSize',0.2); %force plot 'AutoScaleFactor',0.3,

        hU = get(h1,'UData') ;
        hV = get(h1,'VData') ;
        set(h1,'UData',qscale*hU,'VData',qscale*hV)

        text(0,5,['t = ' num2str(t)],'FontSize',12)
        title('Animation')
        axis([-3 90 -5 7])
%         colorbar('location','southoutside')
        axis off
        hold off
        subplot(2,1,2)
        tnow = 0:h:t;
        for i=1:Mlead
            plot(tnow,x(i,1:n)*ks,'LineWidth',2)
            hold all;
%             axis([0 tmax -Tmax Tmax])
        end
        title('Traction Forces')
        xlabel('Time (min)');
        ylabel('Traction force (nN)');
        hold off
        drawnow
        currFrame = getframe(gcf);
        writeVideo(vidObj,currFrame);
    end

%% Adhesion
    if b_link == true % When the integrin is linked to a ligand in ECM
        b_linked = true;
        t_extend = t;
        Mlead = Mnew;
        Mnew = Mnew+1;

        xdot_old = xdot(:,1:n);
        x_old = x(:,1:n);
        xpost_old = xpost(:,1:n);
        eta_old = eta(:,1:n);
```

```
    T_old = T(:,1:n);
    Tdot_old = Tdot(:,1:n);
    S_old = S(:,1:n);
    ka_old = ka;
    b_rel_old = b_rel;

    xdot = zeros(Mlead,N);
    x = zeros(Mlead,N);
    xpost = zeros(Mlead,N);
    eta = zeros(Mlead-1,N);
    T = zeros(Mlead-1,N);
    Tdot = zeros(Mlead-1,N);
    ka = zeros(Mnew,1);
    S = zeros(Mlead,N);
    b_rel = zeros(Mnew,1);

    xdot(1:Mlead-1,1:n) = xdot_old(1:Mlead-1,1:n);
    x(1:Mlead-1,1:n) = x_old(1:Mlead-1,1:n);
    xpost(1:Mlead-1,1:n) = xpost_old(1:Mlead-1,1:n);
    eta(1:Mlead-2,1:n) = eta_old(1:Mlead-2,1:n);
    T(1:Mlead-2,1:n) = T_old(1:Mlead-2,1:n);
    Tdot(1:Mlead-2,1:n) = Tdot_old(1:Mlead-2,1:n);
    ka(Mtail:Mnew-1) = ka_old(Mtail:Mnew-1);
    S(1:Mlead-1,1:n) = S_old(1:Mlead-1,1:n);
    b_rel(1:Mlead-1) = b_rel_old(1:Mlead-1);

    F = zeros(Mlead-Mtail+1,1);
    K = zeros(Mlead-Mtail+1,Mlead-Mtail+1); %elasticity matrix for cell
    rh = ones(Mnew,1); %line handle
    b_link = false;
end
tnew = t - t_extend;
%% Matured Adhesion
if b_linked && (S(Mlead,n) > S_mature)
    b_over = false;
    b_linked = false;
end
%% Release
if T(Mtail,n)/Tmax > S(Mtail,n) % When the old adhesion is released
    b_release = true;
    b_rel(Mtail) = 1;
    b_release_first = true;

end
%% Complete Release
if (b_release == true)&&(abs(x(Mtail,n)) < 0.001)
    Mtail = Mtail+1;
    S_old = S;

    ka_old = ka;

    ka = zeros(Mnew,1);
    S = zeros(Mnew,N);

    ka(Mtail:Mnew) = ka_old(Mtail:Mnew);
    S(1:Mlead,1:n) = S_old(1:Mlead,1:n);

    F = zeros(Mlead-Mtail+1,1);
    K = zeros(Mlead-Mtail+1,Mlead-Mtail+1); %elasticity matrix for cell
    b_release = false;
end
%% Adhesion Dynamics
for i=Mtail:Mlead
    if i==Mtail
        S(i,n+1) = S(i,n)+ h*(- ksb);
    elseif i==Mlead
```

```
            S(i,n+1)       =       S(i,n)+       h*((Smax-S(i,n))*b_linked*T(i-1,n)/((eta(i-
1,n)+eps)*Tmax)*ksf);
        else
            S(i,n+1)  =  S(i,n)+  h*((Smax-S(i,n))*max(T(i-1,n),T(i,n))/((max(eta(i,n),eta(i-
1,n))+eps)*Tmax)*ksf);
        end
    end

%% General Contraction
    % eta
    b_rel_factor = 10;
    eta(Mtail:Mlead-2,n+1)       =       eta(Mtail:Mlead-2,n)+       h*((1-eta(Mtail:Mlead-
2,n))*activationC(t,tau1,tau2)*kf/theta ...
      -(eta(Mtail:Mlead-2,n)+epse*eta(Mtail:Mlead-2,n)+b_rel_factor*b_rel(Mtail:Mlead-
2).*eta(Mtail:Mlead-2,n)-T(Mtail:Mlead-2,n)/Tmax).*(eta(Mtail:Mlead-
2,n)+epse*eta(Mtail:Mlead-2,n)+b_rel_factor*b_rel(Mtail:Mlead-2).*eta(Mtail:Mlead-
2,n)>=T(Mtail:Mlead-2,n)/Tmax)*kb/theta); %(1-S(Mtail:Mlead-2,n+1)).*
%               eta(Mtail:Mlead-1,n+1)   =   eta(Mtail:Mlead-1,n)+   h*((1-eta(Mtail:Mlead-
1,n))*activationC(t)*kf/theta ...
%       -(eta(Mtail:Mlead-1,n)-T(Mtail:Mlead-1,n)/Tmax)*kb/theta);
    eta(Mlead-1,n+1)             =             eta(Mlead-1,n)+             h*((1-eta(Mlead-
1,n))*activationC(tnew,tau1,tau2)*kf/theta ...
      -(eta(Mlead-1,n)+epse*eta(Mlead-1,n)+b_rel(Mlead-1)*(1-S(Mlead-1,n+1))*eta(Mlead-
1,n)-T(Mlead-1,n)/Tmax).*((eta(Mlead-1,n)+epse*eta(Mlead-1,n))>=T(Mlead-
1,n)/Tmax)*kb/theta); %local activation

    %eta hard stop at 1 and 0
    if max(eta(:,n+1)>1) ==1
        for i=1:Mlead-1
            if eta(i,n+1)>=1
                eta(i,n+1)=1;
            end
        end
    elseif max(eta(:,n+1)<0) ==1
        for i=1:Mlead-1
            if eta(i,n+1) < 0
                eta(i,n+1)=0;
            end
        end
    end
    %% x -- making A matrix and F vector
    A = zeros(Mlead-Mtail+1,Mlead-Mtail+1); %clearing A
    for i=1:Mlead-Mtail+1
        %for diagonal
        if i==1
            A(i,i) = -ks-kc1-kc2;
            K(i,i) = kc2/muc*(ks+kc1);
            F(i) = -kc2/muc*S(Mtail-1+i,n+1)/Smax*(T(Mtail-1+i,n))-Tdot(Mtail-1+i,n);
        elseif i==Mlead-Mtail+1 %last component
            A(i,i) = -ks;
            K(i,i) = kc2/muc*ks;
            F(i) = 0;
        else
            A(i,i) = -ks-kc1-kc2;
            K(i,i) = kc2/muc*(ks+kc1);
            F(i) = -kc2/muc*S(Mtail-1+i,n+1)/Smax*(T(Mtail-1+i,n))-Tdot(Mtail-1+i,n);
        end
        %for off-diagonal components
        if i<(Mlead-Mtail+1)
%             A(i,i+1) = mu_new;
%             A(i+1,i) = mu_new;
            A(i,i+1) = kc1+kc2;
            for jj=(i+1):(Mlead-Mtail+1)
                A(jj,i) = -ks;
            end
            K(i,i+1) = - kc2/muc*kc1;
            for jj=(i+1):(Mlead-Mtail+1)
                K(jj,i) = kc2/muc*ks;
```

```
            end
        end
    end

        xdot(Mtail:Mlead,n) = A \ (K*x(Mtail:Mlead,n) + F);
        x(Mtail:Mlead,n+1) = x(Mtail:Mlead,n)+h*xdot(Mtail:Mlead,n);

    %% T - from Hill's muscle model
        for i=Mtail:Mlead-1
%             Ttemp = Tmax*(eta(i,n+1) - kv/vmax*(xdot(i+1,n)-xdot(i,n)));%linear
            v=xdot(i+1,n)-xdot(i,n);
            if eta(i,n+1)==0 && v==0
                Ttemp=0;
            else
                Ttemp=eta(i,n+1)*Tmax*(vmax/kv-v)/(vmax/kv+v/km);
            end

            if v > 0
                T(i,n+1)=Ttemp;
            elseif v < vmax/kv
                T(i,n+1) = 0;
            else
                T(i,n+1) = Ttemp;
            end
        end
        %% Tdot
        Tdot(:,n+1)  =  (T(:,n+1)-T(:,n))/(h);  %this  contains  an  error  because  it  uses
previous time step
end
% Close the file.
close(vidObj);

t=0:h:tmax;

% Results
% set(0,'DefaultAxesColorOrder',[0 0 0],...)
%% Tension
figure
for i=1:Mlead-1
    plot(t,T(i,1:N),'LineWidth',2)
    hold all;
end
% for i=1:Mlead-1
%     plot(t,T(i,1:nfinal)./Tmax)
%     hold all;
% end

title('Tension')
xlabel('Time');
ylabel('Tension');
% axis([0 45 -1.1 1.1])
legend('segment1','segment2','segment3','segment4','segment5','segment6','segment7','segmen
t8','segment9','segment10','segment11','segment12',-1);
hold off

%% Assembly Level
figure;
for i=1:Mlead-1
    plot(t,eta(i,1:N),'LineWidth',2)
    hold all;
end
% for i=1:Mlead-1
%     plot(t,eta(i,1:nfinal))
%     hold all;
% end
title('Assembly level')
xlabel('time');
```

```
ylabel('eta');
legend('segment1','segment2','segment3','segment4','segment5','segment6','segment7','segmen
t8',-1);
hold off

%% Deflections
figure;
for i=1:Mlead
    plot(t,xpost(i,1:N),'LineWidth',2)
    hold all;
end
title('post deflection')
xlabel('time');
ylabel('post deflection');
% legend('node1','node2','node3','node4','node5','node6','node7','node9',...
%     'node10','node11','node12','node13','node14','node15','node16','node17','node18',-1);
legend('post1','post2','post3','post4','post5','post6','post7','post9',...
    'post10','post11','post12','post13','post14','post15','post16','post17','post18',-1);
% axis([0 tmax -0.4 0.4])
hold off
%% Forces
figure;
for i=1:Mlead
    plot(t,xpost(i,1:N)*ks,'LineWidth',2)
    hold all;
end
xlabel('Time (min)');
ylabel('Traction Force (nN)');
legend('post1','post2','post3','post4','post5','post6','post7','post9',
'post10','post11','post12','post13','post14','post15','post16','post17','post18',-1);
hold off
%% X-dots
figure;
for i=1:Mlead
    plot(t,xdot(i,1:N),'LineWidth',0.5)
    hold all;
end

xlabel('Time');
ylabel('dx/dt');
% legend('node1','node2','node3','node4','node5','node6','node7','node9',...
%     'node10','node11','node12','node13','node14','node15','node16','node17','node18',-1);
legend('post1','post2','post3','post4','post5','post6','post7','post9',...
    'post10','post11','post12','post13','post14','post15','post16','post17','post18',-1);
hold off
%% Strain Energy
figure;
SE = zeros(1,tmax/h+1);
x1 = xpost;
for i=1:Mlead
    SE = SE + 0.5*ks*abs(x1(i,1:N)).^2;
end
plot(t,SE)
title('Strain energy')
xlabel('Time');
ylabel('Strain energy');
% axis([0 tmax 0 0.16])
```

Appendix C: Matlab Code for Time-lapse Post Analysis

```
clear all; close all; clc;
%% Getting the video file
[FileName,PathName] = uigetfile('*.avi','Select avi file');
obj=VideoReader(FileName); %read a post RGB video
vidFrames = read(obj);%,[1 420]);

%clearvars -except vidFrames1 obj
%% Getting the bottom image
[FileName_bot,PathName_bot] = uigetfile('*.tif','Select tif file');
%read
bot_image = imread(FileName_bot);
vidFrames_bot = zeros(size(bot_image));
%% setting for post recognition
pin_spacing = 6; %um
area_lim=0.05;
ecc_lim=0.02;
cent_lim=0.5;
ecc_max=0.7;
manual_flagA = 0;
manual_flagB = 0;
area_maxB=280;
area_minB=200;
area_min=31;
area_max=85;
%% reading the video specs
nFrames = length(vidFrames(1,1,1,:));
vidHeight = obj.Height;
vidWidth = obj.Width;

X = vidFrames(:,:,1,1);

%% rotating... - rotating once
imshow(X), drawnow
cmap = colormap;
uiwait(msgbox('Click on upper left post to be analyzed and upper right post to be analyzed
to set rotation angle. Click OK to continue.','mage Rotation','modal'));
hold on;

[rot_y1 rot_x1]=ginput(1);
plot(rot_y1,rot_x1,'b+');
[rot_y2 rot_x2]=ginput(1);
plot(rot_y2,rot_x2,'b+');

posts_between=inputdlg(['How many posts between blue rotation points?'; '(including posts
marked by rotation points):';'                                                    '],'Post
Spacing');
y_spacing=sqrt((rot_x2-rot_x1)^2+(rot_y2-rot_y1)^2)/(str2double(posts_between{1})-1);
ROIstep=round(y_spacing);
convert=pin_spacing/y_spacing;
x_spacing=y_spacing;

rot_angle = -atan2((rot_x1-rot_x2),(rot_y2-rot_y1))*180/pi;
Xr=imrotate(X,rot_angle,'bilinear','crop');
hold off;

%% shifting correction (tracking one post)
% find a center of one post
imshow(Xr), drawnow
uiwait(msgbox(['Drag Rectangle to Crop One Post to be tracked. Click OK to Continue.'],'One
Post Cropping','modal'));
k = waitforbuttonpress;
point1 = get(gca,'CurrentPoint');    % button down detected
finalRect = rbbox;                   % return figure units
```

```
point2 = get(gca,'CurrentPoint');    % button up detected
point1 = point1(1,1:2);              % extract x and y
point2 = point2(1,1:2);
p1 = min(point1,point2);             % calculate locations
o1 = abs(point1-point2);         % and dimensions
x = [p1(1) p1(1)+o1(1) p1(1)+o1(1) p1(1) p1(1)];
y = [p1(2) p1(2) p1(2)+o1(2) p1(2)+o1(2) p1(2)];
hold on
axis manual
plot(x,y,'g','linewidth',2)
halfROIx = ceil(o1(1)/2);
halfROIy = ceil(o1(2)/2);
centerx = p1(1) + halfROIx;
centery = p1(2) + halfROIy;

%% min max area determination
Xred = vidFrames(:,:,1,1);
Xredr=imrotate(Xred,rot_angle,'bilinear','crop');
A = Xredr(centery-halfROIy:centery+halfROIy,centerx-halfROIx:centerx+halfROIx);
alp = graythresh(A); % beginning threshold value

A_bw=im2bw(A,alp);
A_bw2=bwmorph(A_bw,'clean');
A_bw3=bwfill(A_bw2,'holes',8);
A_bw4=bwmorph(A_bw3,'majority');
A_bw5=bwmorph(A_bw4,'clean');
regA=regionprops((A_bw5),'Area','Centroid','EquivDiameter','Eccentricity','Image');

%finding centroid for each region 073008 SH
centA_each = cat(1,regA.Centroid);
distA_each = sqrt((halfROIx-centA_each(:,1)).^2+(halfROIy-centA_each(:,2)).^2);
%comparing each distance for each indexed area
[minA indA] = min(distA_each);

areaA=regA(indA).Area;

area_max=areaA+10;
area_min=areaA-30;

Br=imrotate(bot_image,rot_angle,'bilinear','crop');
B = imadjust(Br(centery-halfROIy:centery+halfROIy,centerx-halfROIx:centerx+halfROIx));
alpB = graythresh(B); % beginning threshold value

B_bw=im2bw(B,alp);
B_bw2=bwmorph(B_bw,'clean');
B_bw3=bwfill(B_bw2,'holes',8);
B_bw4=bwmorph(B_bw3,'majority');
B_bw5=bwmorph(B_bw4,'clean');
regB=regionprops(logical(B_bw5),'Area','Centroid','EquivDiameter','Eccentricity','Image');

ROIcent = [ROIstep/2,ROIstep/2];
centB_each = cat(1,regB.Centroid);
distB_each = sqrt((ROIcent(1,1)-centB_each(:,1)).^2+(ROIcent(1,2)-centB_each(:,2)).^2);
%comparing each distance for each indexed area
[minB indB] = min(distB_each);

areaB=regB(indB).Area;
area_maxB=areaB+5;
area_minB=areaB-50;

vidFramesD = uint8(zeros(size(vidFrames)));
%% actual tracking
wh = waitbar(0,'Please wait...');
for k = 1: nFrames
    Xred = vidFrames(:,:,1,k);
    X = vidFrames(:,:,:,k);
```

```
    Xadj = imadjust(X,stretchlim(X,0));
    Xredadj = imadjust(Xred,stretchlim(Xred,0));
    Xredr=imrotate(Xredadj,rot_angle,'bilinear','crop');
    Xr=imrotate(Xadj,rot_angle,'bilinear','crop');
    bot_image_r=imrotate(bot_image,rot_angle,'bilinear','crop');

%     vidFrames(:,:,1,k) = Xredr;

    A                   =                   Xredr(centery-halfROIy:centery+halfROIy,centerx-
halfROIx:centerx+halfROIx); %M:rows(y-axis), N:columns(x-axis)

    alp = graythresh(A); % beginning threshold value

    A_bw=im2bw(A,alp);
    A_bw2=bwmorph(A_bw,'clean');
    A_bw3=bwfill(A_bw2,'holes',8);
    A_bw4=bwmorph(A_bw3,'majority');
    A_bw5=bwmorph(A_bw4,'clean');
    regA=regionprops((A_bw5),'Area','Centroid','EquivDiameter','Eccentricity','Image');

    %finding centroid for each region 073008 SH
    centA_each = cat(1,regA.Centroid);
    distA_each = sqrt((halfROIx-centA_each(:,1)).^2+(halfROIy-centA_each(:,2)).^2);
    %comparing each distance for each indexed area
    [minA indA] = min(distA_each);

    areaA=regA(indA).Area;
    eccA=regA(indA).Eccentricity;
    centA=regA(indA).Centroid;
    diaA = regA(indA).EquivDiameter;
    %           imshow(A_bw5), drawnow
%     if or(or(isempty(areaA), areaA<area_min),or(areaA>area_max,eccA>ecc_max));
%      center_loopingRGB;
%     end

    %Gaussian Fitting
    Adouble=cast(A,'double');
    Anormalized=Adouble/max(max(Adouble));
    x=linspace(-halfROIx,halfROIx,2*halfROIx+1);                                y=linspace(-
halfROIy,halfROIy,2*halfROIy+1);
    [X,Y]=meshgrid(x,y);
    c=diaA*4;
    b=centA(1,2)-halfROIy;
    a=centA(1,1)-halfROIx;
    params=[a b c 1];
    [trueparam,er]=fminsearch(@(p)errfun(p,Anormalized,X,Y),params); %Gaussian Fitting
    aa=trueparam(1);
    bb=trueparam(2);
    cc=trueparam(3);
    dd=trueparam(4);
    myfit = dd*exp(-(X-aa).^2/cc - (Y-bb).^2/cc);
    centA_GSfit(1,1)=halfROIx+aa+1;
    centA_GSfit(1,2)=halfROIy+bb+1;

    % saving centers into centerx and centery and shift the image acoording
    % to the difference
    if k==1
        centerx = round(centA_GSfit(1,1)+p1(1)-1);
        centery = round(centA_GSfit(1,2)+p1(2)-1);
        oldcenterx = centerx;
        oldcentery = centery;
    else
        centerx = round(centA_GSfit(1,1)+centerx-halfROIx-1);
        centery = round(centA_GSfit(1,2)+centery-halfROIy-1);
    end
```

```
    diffx = centerx - oldcenterx;
    diffy = centery - oldcentery;
    xform = [ 1   0   0
          0   1   0
         -diffx -diffy  1 ];
    tform_translate = maketform('affine',xform);
%     [DeshakedFrame xdata ydata]= imtransform(vidFrames(:,:,:,k), tform_translate);
    DeshakedFrame = imtransform(Xr, tform_translate,...
                    'XData', [1 (size(Xr,2)+ xform(3,1))],...
                    'YData', [1 (size(Xr,1)+ xform(3,2))]);
    DeshakedFrame_bot = imtransform(bot_image_r, tform_translate,...
                    'XData', [1 (size(Xr,2)+ xform(3,1))],...
                    'YData', [1 (size(Xr,1)+ xform(3,2))]);

    DF2 = uint8(zeros(size(Xr)));
    minysize = min(size(DeshakedFrame,1),size(DF2,1));
    minxsize = min(size(DeshakedFrame,2),size(DF2,2));
    DF2(1:minysize,1:minxsize,:) = DeshakedFrame(1:minysize,1:minxsize,:);
    vidFramesD(:,:,:,k) = DF2;

    DF2bot = uint8(zeros(size(bot_image_r)));
    minysize_bot = min(size(DeshakedFrame_bot,1),size(DF2bot,1));
    minxsize_bot = min(size(DeshakedFrame_bot,2),size(DF2bot,2));
    DF2bot(1:minysize_bot,1:minxsize_bot)                                                    =
DeshakedFrame_bot(1:minysize_bot,1:minxsize_bot);
    vidFrames_bot(:,:,:,k) = DF2bot;

    %waitbar
    waitbar(k/nFrames)
end
close(wh)
%% movie making with shifted frames
% Prepare the new file.
vidObj = VideoWriter(regexprep(FileName,'.avi',' deshaked.avi'),'Uncompressed AVI');
% Preallocate movie structure.
mov(1:nFrames) = ...
    struct('cdata', zeros(vidHeight, vidWidth, 3, 'uint8'),...
           'colormap', []);

% Read one frame at a time.
for k = 1 : nFrames
    mov(k).cdata = vidFramesD(:,:,:,k);%/max(max(vidFramesD(:,:,1,k)));
%     imshow(vidFramesD(:,:,:,k)),drawnow
end

% Play back the movie once at the video's frame rate.
open(vidObj)
writeVideo(vidObj,mov);
% Close the file.
close(vidObj);

%% cropping ROI
Xr1 = vidFramesD(:,:,1,1);
Xrn = vidFramesD(:,:,1,nFrames);
Maximize(gcf);
% subplot(2,1,1),imshow(Xr1),
% subplot(2,1,2),imshow(Xrn), drawnow
subplot(1,1,1),imshow(Xrn), drawnow

uiwait(msgbox(['Drag Rectangle to Crop Image at the bottom image. Set the Crop Box outside
of the posts to be analyzed such that it is not touching any posts. Crop box will
automatically resize to units of ' num2str(ROIstep) ' pixels by ' num2str(ROIstep) ' pixels.
Also note that the current area_max = ' num2str(area_max) ', area_min=' num2str(area_min) ',
area_maxB='  num2str(area_maxB)  ',  area_minB='  num2str(area_minB)  '.  Click  OK  to
Continue.'],'Image Cropping','modal'));
k = waitforbuttonpress;
point1 = get(gca,'CurrentPoint');    % button down detected
```

```
finalRect = rbbox;                   % return figure units
point2 = get(gca,'CurrentPoint');    % button up detected
point1 = point1(1,1:2);              % extract x and y
point2 = point2(1,1:2);
p1 = min(point1,point2);             % calculate locations
o1 = abs(point1-point2);         % and dimensions
offset=ceil(o1/ROIstep)*ROIstep;
x = [p1(1) p1(1)+offset(1) p1(1)+offset(1) p1(1) p1(1)];
y = [p1(2) p1(2) p1(2)+offset(2) p1(2)+offset(2) p1(2)];
hold on
axis manual
plot(x,y,'g','linewidth',3)

[Xc R]=imcrop(Xr,[p1 offset]);

%% post analysis - memory allocation
I1=Xc;
I2=Xc(:,:,1);
hold off

% Find and label centers
m = round(R(2));
n = round(R(1));
HW = [R(4) R(3)];
hw = ceil(HW/ROIstep);
col=hw(2);
row=hw(1);

i = 0;
k1 = 0;
p = 0;
final_areaA = zeros(m,n);
final_eccA = zeros(m,n);
% I6a = zeros(size(I2));
I7 = zeros(size(I2));
J7 = zeros(size(I2));
Ix = zeros(size(hw));
Iy = zeros(size(hw));
Jx = zeros(size(hw));
Jy = zeros(size(hw));

%% center tracking
% centr2_top = zeros(hw(1)*hw(2),2,nFrames);
wh = waitbar(0,'Please wait...');
prev_14y=0;
prev_14x=0;
prev_15y=0;
prev_15x=0;

bot_image_r=imrotate(bot_image,rot_angle,'bilinear','crop');

% hROI = [-14 3];
% p1_bot= p1 + hROI;
% bot_image_c=imcrop(bot_image_r,[p1_bot offset]);

bot_image_c=imcrop(bot_image_r,[p1 offset]);

for k = 1:nFrames
    Xr = vidFramesD(:,:,1,k);
%     bot_image_r = vidFrames_bot(:,:,1,k);
%     performed in vidFrmaes
    Xc=imcrop(Xr,[p1 offset]);
    Xc_adj = imadjust(Xc,stretchlim(Xc,0));

    I2=Xc_adj; % post top
    J2=imadjust(bot_image_c,stretchlim(bot_image_c,0)); % post bottom
```

```
    k1 = 0;
    i = 0;
    for M = 1:ROIstep:(hw(1)*ROIstep+1-ROIstep); %row
       i = i + 1;
%        i = 2;
       j = 0;
%        j = 13;
       for N = 1:ROIstep:(hw(2)*ROIstep+1-ROIstep); %column
          j = j + 1;

          %%%%%%%%%%%%%%%%%%%%%
          % Local Threshold I %
          %%%%%%%%%%%%%%%%%%%%%

          A = I2(M:M+(ROIstep-1),N:N+(ROIstep-1)); %M:rows(y-axis), N:columns(x-axis)
          alp = graythresh(A); % beginning threshold value

          A_bw=im2bw(A,alp*1.13);
          A_bw2=bwmorph(A_bw,'clean');
          A_bw3=bwfill(A_bw2,'holes',8);
          A_bw4=bwmorph(A_bw3,'majority');
          A_bw5=bwmorph(A_bw4,'clean');
          regA=regionprops(logical(A_bw5),'Area','Centroid','Eccentricity',…
          'EquivDiameter','Image');

              %finding centroid for each region 073008 SH
              ROIcent = [ROIstep/2,ROIstep/2];
              centA_each = cat(1,regA.Centroid);
              if k==1
                  distA_each     =     sqrt((ROIcent(1,1)-centA_each(:,1)).^2+(ROIcent(1,2)-
centA_each(:,2)).^2);
              else
                  distA_each           =           sqrt((centr2_top((i-1)*col+j,1,k-1)-N+1-
centA_each(:,1)).^2+(centr2_top((i-1)*col+j,2,k-1)-M+1-centA_each(:,2)).^2);
              end
              %comparing each distance for each indexed area
              [minA indA] = min(distA_each);

              areaA=regA(indA).Area;
              eccA=regA(indA).Eccentricity;
              centA=regA(indA).Centroid;
              diaA = regA(indA).EquivDiameter;

              final_areaA(i,j)=areaA;
              final_eccA(i,j)=eccA;

              if or(or(isempty(areaA), areaA<area_min),or(areaA>area_max,eccA>ecc_max));
                 center_looping;
              end

          % saving centers into Ix,Iy (top)
          Ix(i,j) = N+centA(1,1)-1;
          Iy(i,j) = M+centA(1,2)-1;

          %%%%%%%%%%%%%%%%%%%%%
          % Local Threshold J %
          %%%%%%%%%%%%%%%%%%%%%
          if k==1
              B = J2(M:M+(ROIstep-1),N:N+(ROIstep-1)); %M:rows(y-axis), N:columns(x-axis)
              alp = graythresh(B); % beginning threshold value

              B_bw=im2bw(B,alp);
              B_bw2=bwmorph(B_bw,'clean');
              B_bw3=bwfill(B_bw2,'holes',8);
              B_bw4=bwmorph(B_bw3,'majority');
              B_bw5=bwmorph(B_bw4,'clean');
```

```
regB=regionprops(logical(B_bw5),'Area','Centroid','EquivDiameter','Eccentricity','Image');

              ROIcent = [ROIstep/2,ROIstep/2];
              centB_each = cat(1,regB.Centroid);
              distB_each       =       sqrt((ROIcent(1,1)-centB_each(:,1)).^2+(ROIcent(1,2)-
centB_each(:,2)).^2);
              %comparing each distance for each indexed area
              [minB indB] = min(distB_each);

              areaB=regB(indB).Area;
              eccB=regB(indB).Eccentricity;
              centB=regB(indB).Centroid;
              diaB = regB(indB).EquivDiameter;
              final_areaB(i,j)=areaB;
              final_eccB(i,j)=eccB;
    %           imshow(B_bw5), drawnow
              if or(or(isempty(areaB), areaB<area_minB),or(areaB>area_maxB,eccB>ecc_max));
                 center_loopingB;
              end
              J6=B_bw5;
              J6a(:,:,i,j)=B_bw5;

              J7(M:M+(ROIstep-1),N:N+(ROIstep-1)) = J6;

              % saving centers into Jx, Jy (bottom) SH
%               Jx(i,j) = N+centB(1,1)-1;
%               Jy(i,j) = M+centB(1,2)-1;
              Jx(i,j) = N+centB(1,1)-1;
              Jy(i,j) = M+centB(1,2)-1;
              p = p+1;
              k1 = k1 + 1;
              LongIx(k1) = Ix(i,j);
              LongIy(k1) = Iy(i,j);
              LongJx(k1) = Jx(i,j);
              LongJy(k1) = Jy(i,j);
          else
              p = p+1;
              k1 = k1 + 1;
              LongIx(k1) = Ix(i,j);
              LongIy(k1) = Iy(i,j);
              LongJx(k1) = Jx(i,j);
              LongJy(k1) = Jy(i,j);
          end
       end
    end

    %Shifting bottom centers to center of the unoccupied top centers
    dx = LongIx(1) - LongJx(1);
    dy = LongIy(1) - LongJy(1);
    LongJx = LongJx + dx;
    LongJy = LongJy + dy;

    IIa = bwmorph(I7,'remove');
    ix = LongIx;
    iy = LongIy;
    jx = LongJx;
    jy = LongJy;

    centr_top.Centroid=[transpose(ix) transpose(iy)];
    centr_bottom.Centroid=[transpose(jx) transpose(jy)];

    %final centers through lots of conversions... centr2_top, centr2_bot
    centr2_top(:,:,k)=cat(1,centr_top.Centroid);
    centr2_bot(:,:,k)=cat(1,centr_bottom.Centroid);
```

```
    % Calculate number of posts
    nposts_top=length(centr2_top(:,:,k));

    %waitbar
    waitbar(k/nFrames,wh, ['k=' num2str(k) '/' num2str(nFrames)])
end
close(wh)
%% Showing without movie making
for k = 1%: nFrames
    Xr = vidFramesD(:,:,:,k);
    Xc=imcrop(Xr,[p1 offset]);

    I2=Xc(:,:,1); % post top

    imshow(I2),
    hold on;
    plot(centr2_top(:,1,k),centr2_top(:,2,k),'b*');
    plot(centr2_bot(:,1,k),centr2_bot(:,2,k),'r*');
%                                                       text(10,140,['k=            '
num2str(k)],'FontName','Arial','FontSize',18,'Color','w','FontWeight','bold','BackgroundCol
or','k')

    hold off
    drawnow
    axis tight;
end
%% Making video showing top centers and bottom centers
vidObj2 = VideoWriter(regexprep(FileName,'.avi',' centers.avi'));
open(vidObj2);
set(gca,'nextplot','replacechildren');
set(gcf,'Position',[0, 300, 900, 400])
for k = 1: nFrames
    Xr = vidFramesD(:,:,:,k);
%     Xr=imrotate(X,rot_angle,'bilinear','crop'); % rotation is already
%     performed in vidFrmaes
    Xc=imcrop(Xr,[p1 offset]);

    I2=Xc(:,:,1); % post top

    imshow(I2),
    hold on;
    plot(centr2_top(:,1,k),centr2_top(:,2,k),'b*');
    plot(centr2_bot(:,1,k),centr2_bot(:,2,k),'r*');
    text(10,130,['k=                                                                '
num2str(k)],'FontName','Arial','FontSize',18,'Color','w','FontWeight','bold','BackgroundCol
or','k')

    hold off
    drawnow
    axis tight;

    currFrame = getframe(gcf);
    writeVideo(vidObj2,currFrame);
end
% Close the file.
close(vidObj2);

%rearrange grids to fit form needed later in program:
y_top(:,:)=double(centr2_top(:,1,:));
x_top(:,:)=double(centr2_top(:,2,:));

y_bot(:,:)=double(centr2_bot(:,1,:));
x_bot(:,:)=double(centr2_bot(:,2,:));

n=length(x_top(:,1));
```

```
% Sort center data based on y coordinate...
for k=1:nFrames
    [sort1_x_top(:,k),ind1_top(:,k)]=sort(x_top(:,k));
    [sort1_x_bot(:,k),ind1_bot(:,k)]=sort(x_bot(:,k));
end
col=1;

for i=2:length(sort1_x_top(:,1));
   if sort1_x_top(i,1) < (sort1_x_top(1,1)+ROIstep/2+1);
      col=col+1;
   end
end

row=floor(n/col);
% Now sort each row by x coordinate
for k=1:nFrames
    for i = 1:n
       s_y_top(i,k)=y_top(ind1_top(i,k));
       s_y_bot(i,k)=y_bot(ind1_bot(i,k));
    end
    sort1_y_top(1,1:n,k)=transpose(s_y_top(:,k));
    sort1_y_bot(1,1:n,k)=transpose(s_y_bot(:,k));
end
for k=1:nFrames
    for i=1:row;
       temp_x_top=[sort1_x_top((1+(i-1)*col):(i*col),k)];
       temp_y_top=[sort1_y_top(1,(1+(i-1)*col):(i*col),k)];
       temp_x_bot=[sort1_x_bot((1+(i-1)*col):(i*col),k)];
       temp_y_bot=[sort1_y_bot(1,(1+(i-1)*col):(i*col),k)];

       [sort2_y_top,ind2_top(:,k)]=sort(temp_y_top);
       [sort2_y_bot,ind2_bot(:,k)]=sort(temp_y_bot);

       for j=1:col;
          s_x_top(j)=temp_x_top(ind2_top(j));
          s_x_bot(j)=temp_x_bot(ind2_bot(j));
       end
       sort2_x_top=transpose(s_x_top);
       sort2_x_bot=transpose(s_x_bot);

       sort1_x_top((1+(i-1)*col):(i*col),k)=sort2_x_top;
       sort1_y_top(1,(1+(i-1)*col):(i*col),k)=sort2_y_top;
       sort1_x_bot((1+(i-1)*col):(i*col),k)=sort2_x_bot;
       sort1_y_bot(1,(1+(i-1)*col):(i*col),k)=sort2_y_bot;
    end
end

for k = 1: nFrames
    for i=1:row
       for j=1:col
          actual_x_top(i,j,k)=sort1_x_top(col*(i-1)+j,k);
          actual_y_top(i,j,k)=sort1_y_top(1,col*(i-1)+j,k);
          actual_x_bot(i,j,k)=sort1_x_bot(col*(i-1)+j,k);
          actual_y_bot(i,j,k)=sort1_y_bot(1,col*(i-1)+j,k);
          direct_x_top(i,j,k)=x_top(col*(i-1)+j,k);
          direct_y_top(i,j,k)=y_top(col*(i-1)+j,k);
          direct_x_bot(i,j,k)=x_bot(col*(i-1)+j,k);
          direct_y_bot(i,j,k)=y_bot(col*(i-1)+j,k);
       end
    end
end
for k = 1: nFrames
    for i=1:row;
       for j=1:col;
          delta_x(i,j,k)=actual_x_top(i,j,k)-actual_x_bot(i,j,k);
          delta_y(i,j,k)=actual_y_top(i,j,k)-actual_y_bot(i,j,k);
          direct_delta_x(i,j,k)=direct_x_top(i,j,k)-direct_x_bot(i,j,k);
```

```
          direct_delta_y(i,j,k)=direct_y_top(i,j,k)-direct_y_bot(i,j,k);
       end
    end
end
uiwait(msgbox(['Centroid analysis is done. Please stop the program by pressing ctrl+c then
decide   which   posts   are   cell   posts.   Click   OK   to   Continue.'],'Cell   Post
Designation','modal'));

% % showing the movie of BF
% % movie(CroppedFrames,3)
% for the posts that are always underneath a cell
delta_y(2,1:12,:,2) = 1;
delta_x(2,1:12,:,2) = 1;
delta_y(2,13,24:715,2) = 1;
delta_x(2,13,24:715,2) = 1;
delta_y(2,14,453:715,2) = 1;
delta_x(2,14,453:715,2) = 1;
delta_y(1,12,1:430,2) = 1;
delta_x(1,12,1:430,2) = 1;
% %adhesion
%
% %release
%% Shift the result with average deflections of all empty posts- Skip
total_empty_x = zeros(nFrames,1);
total_empty_y = zeros(nFrames,1);
dtotal_empty_x = zeros(nFrames,1);
dtotal_empty_y = zeros(nFrames,1);
border_num = zeros(nFrames,1);
for k=1:nFrames
    for i=1:row;
       for j=1:col;
           if delta_x(i,j,k,2) ==0
                total_empty_x(k)=total_empty_x(k)+delta_x(i,j,k,1);
                total_empty_y(k)=total_empty_y(k)+delta_y(i,j,k,1);
                dtotal_empty_x(k)=total_empty_x(k)+direct_delta_x(i,j,k);
                dtotal_empty_y(k)=total_empty_y(k)+direct_delta_y(i,j,k);
                border_num(k) = border_num(k)+1;
           end
       end
    end
end
avg_grid_err_x=total_empty_x./border_num;
avg_grid_err_y=total_empty_y./border_num;
davg_grid_err_x=dtotal_empty_x./border_num;
davg_grid_err_y=dtotal_empty_y./border_num;
for k=1:nFrames
    delta_x2(:,:,k,1)=delta_x(:,:,k,1)-avg_grid_err_x(k);
    delta_y2(:,:,k,1)=delta_y(:,:,k,1)-avg_grid_err_y(k);
    direct_delta_x2(:,:,k) = direct_delta_x(:,:,k)-davg_grid_err_x(k);
    direct_delta_y2(:,:,k) = direct_delta_y(:,:,k)-davg_grid_err_y(k);
end
%% Shifting with average deflections of empty posts by each column
for k=1:nFrames
    nn=1;
    while nn<=col
        border_num = 0;
        total_empty_x=0;
        total_empty_y=0;
        dtotal_empty_x=0;
        dtotal_empty_y=0;
        for j=nn
            for i=1:row
                if delta_y(i,j,k,2) ==0
                    total_empty_x=total_empty_x+delta_x(i,j,k,1);
                    total_empty_y=total_empty_y+delta_y(i,j,k,1);
                    dtotal_empty_x=dtotal_empty_x+direct_delta_x(i,j,k);
                    dtotal_empty_y=dtotal_empty_y+direct_delta_y(i,j,k);
                    border_num = border_num+1;
```

```
                end
            end
        end

        avg_grid_err_x=total_empty_x/border_num;
        avg_grid_err_y=total_empty_y/border_num;
        davg_grid_err_x=dtotal_empty_x/border_num;
        davg_grid_err_y=dtotal_empty_y/border_num;

        delta_x2(:,nn,k,1)=delta_x(:,nn,k,1)-avg_grid_err_x;
        delta_y2(:,nn,k,1)=delta_y(:,nn,k,1)-avg_grid_err_y;
        direct_delta_x2(:,nn,k) = direct_delta_x(:,nn,k)-davg_grid_err_x;
        direct_delta_y2(:,nn,k) = direct_delta_y(:,nn,k)-davg_grid_err_y;
        nn=nn+1;
    end
end
%% Shifting with average deflections of empty posts by every two columns- Skip
for k=1:nFrames
    nn=1;
    while nn<col
        border_num = 0;
        total_empty_x=0;
        total_empty_y=0;
        dtotal_empty_x=0;
        dtotal_empty_y=0;
        for j=nn:nn+1
            for i=1:row
                if delta_y(i,j,k,2) ==0
                    total_empty_x=total_empty_x+delta_x(i,j,k,1);
                    total_empty_y=total_empty_y+delta_y(i,j,k,1);
                    dtotal_empty_x=dtotal_empty_x+direct_delta_x(i,j,k);
                    dtotal_empty_y=dtotal_empty_y+direct_delta_y(i,j,k);
                    border_num = border_num+1;
                end
            end
        end

        avg_grid_err_x=total_empty_x/border_num;
        avg_grid_err_y=total_empty_y/border_num;
        davg_grid_err_x=dtotal_empty_x/border_num;
        davg_grid_err_y=dtotal_empty_y/border_num;

        delta_x2(:,nn:nn+1,k,1)=delta_x(:,nn:nn+1,k,1)-avg_grid_err_x;
        delta_y2(:,nn:nn+1,k,1)=delta_y(:,nn:nn+1,k,1)-avg_grid_err_y;
        direct_delta_x2(:,nn:nn+1,k) = direct_delta_x(:,nn:nn+1,k)-davg_grid_err_x;
        direct_delta_y2(:,nn:nn+1,k) = direct_delta_y(:,nn:nn+1,k)-davg_grid_err_y;
        nn=nn+2;
    end
    if nn==col
        border_num = 0;
        total_empty_x=0;
        total_empty_y=0;
        dtotal_empty_x=0;
        dtotal_empty_y=0;
        for j=nn
            for i=1:row
                if delta_y(i,j,k,2) ==0
                    total_empty_x=total_empty_x+delta_x(i,j,k,1);
                    total_empty_y=total_empty_y+delta_y(i,j,k,1);
                    dtotal_empty_x=dtotal_empty_x+direct_delta_x(i,j,k);
                    dtotal_empty_y=dtotal_empty_y+direct_delta_y(i,j,k);
                    border_num = border_num+1;
                end
            end
        end

        avg_grid_err_x=total_empty_x/border_num;
```

```
        avg_grid_err_y=total_empty_y/border_num;
        davg_grid_err_x=dtotal_empty_x/border_num;
        davg_grid_err_y=dtotal_empty_y/border_num;

        delta_x2(:,nn,k,1)=delta_x(:,nn,k,1)-avg_grid_err_x;
        delta_y2(:,nn,k,1)=delta_y(:,nn,k,1)-avg_grid_err_y;
        direct_delta_x2(:,nn,k) = direct_delta_x(:,nn,k)-davg_grid_err_x;
        direct_delta_y2(:,nn,k) = direct_delta_y(:,nn,k)-davg_grid_err_y;
    end
end
%% Data Smoothing
k=1:nFrames;
for i=1:row
    for j=1:col
        temp_x = reshape(direct_delta_x2(i,j,:,1),[],1);
        temp_y = reshape(direct_delta_y2(i,j,:,1),[],1);
        [scsx px] = csaps(k,temp_x);
        [scsy py] = csaps(k,temp_y);
        scsx2 = csaps(k,temp_x,px*0.5);
        scsy2 = csaps(k,temp_y,py*0.5);
        direct_delta_x3(i,j,:) = fnval(scsx2,k);
        direct_delta_y3(i,j,:) = fnval(scsy2,k);
    end
end
%% No Smoothing - Skip
k=1:nFrames;
for i=1:row
    for j=1:col
        direct_delta_x3(i,j,:) = direct_delta_x2(i,j,:);
        direct_delta_y3(i,j,:) = direct_delta_y2(i,j,:);
    end
end
%% Calculate conversion factor for pixels to microns and convert grids
%pin_spacing=6um
pin_spacing = 6;
convert=pin_spacing/y_spacing;

delta_x_micron=delta_x2*convert;
delta_y_micron=delta_y2*convert;
ddelta_x_micron=direct_delta_x3*convert;
ddelta_y_micron=direct_delta_y3*convert;

% convert deflections to forces
force_convert=38; %nN/um - why? (SH) need to be recalculated.
force_x=delta_x_micron*force_convert;
force_y=delta_y_micron*force_convert;
dforce_x=ddelta_x_micron*force_convert;
dforce_y=ddelta_y_micron*force_convert;
%% result video with force vectors
figure;
% Write a video file
vidObj3 = VideoWriter(regexprep(FileName,'.avi',' forces.avi'));
open(vidObj3);
set(gcf,'nextplot','replacechildren');
set(gcf,'Position',[0, 100, 900, 400])
mag_factor = 10;
t_interval = 10; %in seconds
for k = 1: nFrames
    X = vidFramesD(:,:,1,k);
%     Xr=imrotate(X,rot_angle,'bilinear','crop');
    Xc=imcrop(X,[p1 offset]);
    Xadj=imadjust(Xc);
    imshow(Xadj);
    hold on

% direct_delta3
    quiver(actual_y_bot(:,:,k),actual_x_bot(:,:,k),...
        mag_factor*direct_delta_y3(:,:,k,1).*delta_y(:,:,k,2),...
```

```
        mag_factor*direct_delta_x3(:,:,k,1).*delta_x(:,:,k,2),0,'w','Linewidth',2);
    quiver(actual_y_bot(:,:,k),actual_x_bot(:,:,k),...
        mag_factor*direct_delta_y3(:,:,k,1).*(1-delta_y(:,:,k,2)),...
        mag_factor*direct_delta_x3(:,:,k,1).*(1-delta_x(:,:,k,2)),0,'k','Linewidth',2);

   quiver(10,10,...
        mag_factor*10.0/38/convert,0,'y','Linewidth',2);
    text(10,130,['t=      '      num2str(floor(t_interval/60*(k-1)))      '      min      '
num2str(mod(t_interval*(k-1),60))                                                    '
sec'],'FontName','Arial','FontSize',18,'Color','w','FontWeight','bold','BackgroundColor','k
')
    drawnow
    hold off
    currFrame = getframe(gcf);
    writeVideo(vidObj3,currFrame);
end
close(vidObj3);

%% force magnitude plot for all posts
figure;
t_interval = 5/60; %in minute
tk=(1-1:nFrames-1)*t_interval; %2 means two minute period
p=0;
for i = 2
    for j=1:14%[6 11 20]%1:size(delta_x,2)
        p = p+1;
        y_force = reshape(dforce_y(i,j,:),[],1);
        plot(tk,y_force)
        hold all
    end
end
ylabel('Traction Force in x-direction (nN)');
legend('post  1','post  2','post  3','post  4','post  5','post  6','post  7','post  8','post
9','post 10','post 11','post 12','post 13','post 14','post 15','post 16','post 17','post
18','post 19','post 20','post 21','post 22','post 23','post 24','post 25','post 26','post
27','post 28',-1);
xlabel('Time (min)');
% hold off

%% Total strain energy
figure;
tk=(1-1:nFrames-1)*t_interval;
%                                          SE                                                =
0.5*sum(sum((ddelta_x_micron(:,:,:).*delta_x(:,:,:,2)).^2+(ddelta_y_micron(:,:,:).*delta_y(
:,:,:,2)).^2))*38;
SE                                                                                           =
0.5*(sum((ddelta_x_micron(2,:,:).*delta_x(2,:,:,2)).^2+(ddelta_y_micron(2,:,:).*delta_y(2,:
,:,2)).^2))*38;
% SE = 0.5*sum(sum(((ddelta_y_micron(:,:,:).*delta_y(:,:,:,2)).^2)))*38;
plot(tk,reshape(SE,[],1),'k','LineWidth',2), title('Strain Energy');
xlabel('Time (min)');
ylabel('Strain Energy (fJ)');
hold on
SE2                          =                          0.5*sum(sum((ddelta_x_micron(:,:,:).*(1-
delta_x(:,:,:,2))).^2+(ddelta_y_micron(:,:,:).*(1-delta_y(:,:,:,2))).^2))*38;
% SE2 = 0.5*sum(sum(((ddelta_y_micron(:,:,:).*(1-delta_y(:,:,:,2))).^2)))*38;
plot(tk,reshape(SE2,[],1),'Color',[0.6 0.6 0.6])
%% Total Force
figure;
tk=(1-1:nFrames-1)*t_interval;
TotF                                                                                         =
sum(sum(abs(ddelta_x_micron(:,:,:).*delta_x(:,:,:,2))+abs(ddelta_y_micron(:,:,:).*delta_y(:
,:,:,2))))*38;
plot(tk,reshape(TotF,[],1),'k','LineWidth',2)
xlabel('Time (min)');
ylabel('Total Force (nN)');
hold on
```

```
TotF2                          =                          sum(sum(abs(ddelta_x_micron(:,:,:).*(1-
delta_x(:,:,:,2)))+abs(ddelta_y_micron(:,:,:).*(1-delta_y(:,:,:,2)))))*38;
plot(tk,reshape(TotF2,[],1),'Color',[0.6 0.6 0.6])
%% Save
MatFileName = regexprep(FileName,'.avi','.mat');
save(MatFileName, '-v7.3')
```

VITA

Sangyoon Han was born in London and raised in Seoul, Korea. He earned a Bachelor of Arts and a Master of Arts in Mechanical Engineering at Seoul National University. In 2012 he earned a Doctor of Philosophy at the University of Washington in Mechanical Engineering.